Mechanical properties of glial cells

by

Amy M. Dagro

A dissertation submitted to The Johns Hopkins University in conformity with the requirements for the degree of Doctor of Philosophy.

Baltimore, Maryland

January, 2019

Abstract

In recent years, traumatic brain injury (TBI) has received an increase in attention as an "invisible wound"–where mild injuries are difficult to detect non-invasively and remain undiagnosed until postmortem analysis. As most of our knowledge comes from neuropathological evaluation of cellular damage, there is a need for relating the injurious loading to damage at the level of cellular networks. For example, recent analysis of postmortem samples from former football athletes, as well as military personnel, show peculiar damage surrounding arterioles–the small vessels of the arterial vasculature that feed into the capillary bed of the brain. The locations and extent of damage are largely dependent on heterogeneity of brain tissue, which at the length scale of interest (1-100 μm), is poorly defined.

Glial cells–which encompass astrocytes, oligodendrocytes, and microglia–are conventionally believed to comprise the softer "isotropic matrix" which surround axons in previous multiscale models. However, heterogeneity at smaller length scales implies that this might no longer be the case, as the brain appears more as a fibrous network. To simplify the extremely dense and complex structure of brain tissue at

ABSTRACT

the mesoscale, we aim to answer the question, *Is there a length scale at which brain tissue constituents have homogeneous mechanical properties?*

To obtain local mechanical properties of glial cell processes, conventional techniques for obtaining cellular mechanical properties are mostly limited to probing cells grown on 2D substrates, which are shown to provide an unrealistic morphology for glial cells. In order to obtain mechanical properties of glial cell processes with a realistic morphologies, we devised a new experimental platform to probe cellular processes grown in a 3D polymeric scaffold via indentation by optically trapped silica beads. Due to the soft nature of glial cell processes, small forces can generate significantly large deformations–often exceeding the linear elastic regime described by classical Hertzian contact. In light of this observation, we developed a force-displacement relationship for the elliptical contact loading on a hyperelastic cylindrical body. Through our experiments, we demonstrate the glial cells have some mechanical properties that are predominantly homogeneous at small length scales, although their behavior is largely affected by strain-rate. Our findings provide a contribution to our understanding of mesoscale material properties of brain tissue. In the future, we hope this will aid in the development of accurate relationships between the mechanics and neuropathological observations following TBI.

Thesis advisor and Primary Reader: K.T. Ramesh

Secondary Readers: Arun Venkatesan and Christian Franck

Acknowledgments

"Within about seven years every atom in your body will be replaced by other atoms. Physically, you are constantly a new you. Fortunately, there maybe be one constant that links all those different versions of your self together: memory."

-David Eagleman, The Brain: The Story of You

I am very thankful to the professors, mentors, friends, and family that were essential in helping me reach this point in my life. First, I would like to thank my Ph.D. advisor, Prof. K.T. Ramesh, (a.k.a. "DJ K.T." by the undergraduate students) who spent many hours teaching me how to approach problems and communicate effectively. KT's talents in mechanics, vision formulation, and mesmerizing audiences, are qualities that I will strive for in many years to come. I would also like to thank my thesis committee members, Prof. Christian Franck and Prof. Arun Venkatesan for imparting your knowledge to me during my graduate school years and for taking the time to read this thesis.

I am immensely grateful to Dr. Chris Hoppel, my supervisor at the U.S. Army

ACKNOWLEDGMENTS

Research Laboratory (ARL) who was very supportive of me returning to school. Chris and the folks at ARL allowed me to pursue school full-time by pointing me in the direction of the DoD SMART scholarship program–something that helped me get the most out of the graduate school experience. I am very fortunate to have had the opportunity to start my career with Prof. Reuben Kraft, who was my first mentor at ARL. Reuben invested hundreds of hours in teaching me practical research skills, as well as teaching me how to have fun while working. Part of my own enthusiasm for research comes from the time I spent working with Reuben. At ARL, I have been fortunate to have great coworkers. A special thanks to Kimberly Thompson and Justin McKee who have always been helpful and willing to teach me new things.

Much of the experimental work in this paper is interdisciplinary, and would not have been possible without the help and generosity of others. I would especially like to thank Labchan Rajbhandari for the hours spent helping me through cell culturing, staining, and imaging for my experiments. To Prof. Santiago Orrego and Prof. Sung Hoon Kang, it was a pleasure to work with you and thank you both for your generosity and words of encouragement. Also a special thanks to Dr. Nitin Daphalapurkar for his helpful advice and enjoyable conversations throughout the years. Thank you to Dr. Vassilis Koliatsos and his group (Dr. Nikolaos Ziogas and Dr. Jiwon Ryu), for our interesting meetings, and introducing me to their very interesting pathology work in perivascular damage following brain injury in veterans.

Thank you to my friends and colleagues, who have made my years during graduate

school an enjoyable experience. Thank you to all of the staff at the Hopkins Extreme Materials Institute, especially Matt Shaeffer and Katie Vaught, who not only put up with endless requests, but are great friends to have. I would be remiss not to thank my fellow Ramesh Lab group members. I am thankful for the advice and support I received over the years from the senior lab members: Adam Fournier, thank you for showing me the ropes early on and introducing me to Dr. Venkatesan's group, both of which were critical for my success. Justin Wilkerson, I always admired how you could simultaneously play poker on your cell phone, watch television, and type some new equation into Matlab in between poker rounds. You give us all hope that brilliant scientists can still be functional and socially competent people. I appreciate you and Natasha for being great friends and providing words of encouragement. Neha Dixit, thank you for being a great friend, as well as introducing me to Zumba (which I continued to attend religiously, along with Barbara Murienne). I was fortunate to also have guidance and support from several excellent postdocs, including: Jamie Hogan, Lukasz Farbaniec, Shailesh Ganpule, Andrew Leong, and Minju Kang. A special thanks to Jamie for teaching me some Canadian lingo (#cesars) which proved to be very useful during my vacation in P.E.I.

Thank you to the junior Ramesh lab colleagues: Jason Parker, Alex Sun, Sakshi Baroo, Gary Simpson, and Adyota Gupta. You guys have been great friends, and I am confident that you all will be successful in anything that you do. Thank you to my "younger older brother" Vignesh Kannan, who is incredibly knowledgeable and

kind. We are all very fortunate to have had such a helpful lab mate, and I am glad that you were always willing to accompany me on random hiking trips. Thank you to the other "Latrobe expert", Meng Zhao, for also being helpful and always having a positive attitude. You were also a great classmate and extremely helpful colleague when we were TAing together. To Kimmie Leonard, thank you for all of your support and encouragement, and I will miss our lunches together. Fatma Madouh, you were incredibly helpful throughout the years. Thank you for keeping me aware of meetings I needed to go to, letting me study from your beautiful notes, and surprising us all with candy on a frequent basis. A special thank you to Debjoy's "redneck brother", Andrew Robinson, for being a reliable friend and introducing us to the turtle hunter call. You are basically our family member, and I will always be there ready to call 911 or give you a Band Aid.

A memorable part of the graduate school experience encompasses the grueling hours of working on homework assignments and studying for tests with your peers. Thank you to my classmates: Charles El-Mir, George Weber, Deniz Öztürk, Meng Zhao, and David Eastman. I am very fortunate to have had such a fun group of colleagues to help survive the first 2 years of suffering through graduate school.

Some of the most enjoyable parts of graduate school involved spending time with friends through intramural sports ("Team Obi wan Latrobie") and the occasional weekend activity (hot pot, karoake, Glacier National Park, Old Rag, and Iceland, to name a few). Thank you to Gianna Valentino, Tracy Ling, Harsh (last name

TBD), Jason Parker, Matt Vaughn, Anu Kaushik, and Elina Spyrou for joining in last-minute plans to movies/dinner on a regular basis. A special thank you to the "Hampden Connection" (George Weber, Mattia Almansi, Max Pinz, Mo Mohammed) for being reliable attendees of "75% off night" at Five and Dime.

To my Baltimore-based JHU undergrad family (Sonia Sarkar, Vikram Rajpurohit, and Neil Neumann), I am so happy that you stuck around Baltimore throughout the years. You guys have always been very important to Debjoy and myself, and I look forward to seeing your continuing successes in the future. The last group should also include Jessica McCue, who has been one of my closest friends since middle school, and is basically a Hopkins alumna, for all intents and purposes.

After being in Baltimore for the last 14 years, I am fortunate to have had the support of friends that I have met before starting graduate school. Thank you to Jennifer Matsumoto, Monisha Cherayil, and Tegan Feehery for the occasional "Galentine's Day" and basically being my older (although not much older) sisters. Also, a special thank you to Debjoy's surrogate older brother, Sid Chaudhury, for always being there for us. I sleep better at night knowing that in case of any emergency or natural disaster, I can probably call up you or Matt Shaeffer, and at least one of you can provide some useful guidance.

To my parents, Mark and Maria Dagro, thank you for inspiring me to work hard and for shaping me into the person I am today. A special thanks to my brother, James Dagro, for always being there for support and for being my most trusted ally.

ACKNOWLEDGMENTS

Thank you to the "Mallick Family Mafia" for being supportive of Debjoy and myself during the pursuance of our PhDs. A special thanks to my father-in-law, Debasish Mallick for his endless love for family and hard work planning our summer vacations. And finally, a big thank you to my husband/co-worker/best friend, Debjoy Mallick, for help with everything from cooking dinner to studying for exams.

Dedication

This thesis is dedicated to my husband Debjoy (if you clean the garage).

Contents

List of Tables

List of Figures

Chapter 1

Introduction and motivation

1.1 Motivation

A recent study estimates that 69 million individuals worldwide sustain a traumatic brain injury (TBI) each year, with the majority of cases being considered mild TBI [21]. Since mild TBI detection methods are still in their infancy, postmortem analysis of human brain tissue is needed to definitively diagnose neurodegenerative disease following injury [22]. As public awareness of TBI rises, postmortem brain donations to "brain bank" repositories also continue to rise [23, 24], allowing researchers to have access to thousands of injured human brain tissue specimens. With these specimens, neuropathologists can observe cellular-level damage and disease, often invisible with non-invasive imaging on living patients.

Understanding the relationship between the physics of the initial injury event and

the subsequent neuropathological observations is a critical step for future strategies in protection, diagnosis, and treatment for TBI patients. However, relating the mechanics of brain injury to neuropathology is a non-trivial task. The challenges include:

- The range of time scales involved (e.g., the duration of loading versus the time scales of biological processes)
- The lack of a comprehensive understanding of injury thresholds
- The variations in mechanical properties of brain tissue with location and at different length scales
- A scarcity of smaller length scale physics-based computational models of brain tissue to quantify cellular damage following an injurious event

Although the initial injury event is over within milliseconds, the biological events that lead to a neurodegenerative state can occur over hours, days, and weeks (well beyond the time scales examined with conventional computational mechanics modeling) [25]. Furthermore, there is limited knowledge regarding the correlations between tissue-level deformations and functional injury. In recent years, progress has been made using strain-based thresholds for brain injury [26–29]. However these thresholds are often for specific cell types, and are based on empirical observations alone. The relationship between mechanical loading at the cell-level and the ensuing cytoskeletal events that could lead to neurodegeneration is an area of ongoing research [30,30–32].

Computational models provide a promising avenue for understanding how macroscale strains can result in damage to cell membranes, cytoskeletal structures, and intercellular adhesion complexes. However, we are far from the realization of accurate models of injury in part because our knowledge of the mechanical properties at this length scale is incomplete. Furthermore, it is necessary to know when and how to simplify models at each length scale due to the complexity of brain tissue microstructure and heterogeneity (discussed in the following sections).

1.1.1 Background: hierarchical structure of brain tissues

A schematic overview of the various structures of the central nervous system (CNS) at different lengthscales is shown in Figure 1.1. Although we have omitted a few structures from the schematic (ventricular structures, deep gray matter, etc.), the majority of the cerebrum and cerebellum can generally be divided into the outer gray matter and inner white matter regions. Throughout the thesis, the macroscale refers to tissue level structures (0.5 mm and larger), while the mesoscale is defined here as the scale at which various cytoarchitectures (i.e., arrangements of cells) are observed (1 μm - 500 μm). Both gray and white matter contain neurons, glial cells, and the endothelial and smooth muscle cells that comprise the vascular network.

In the white matter, myelinated axons align into fiber bundles. Although the

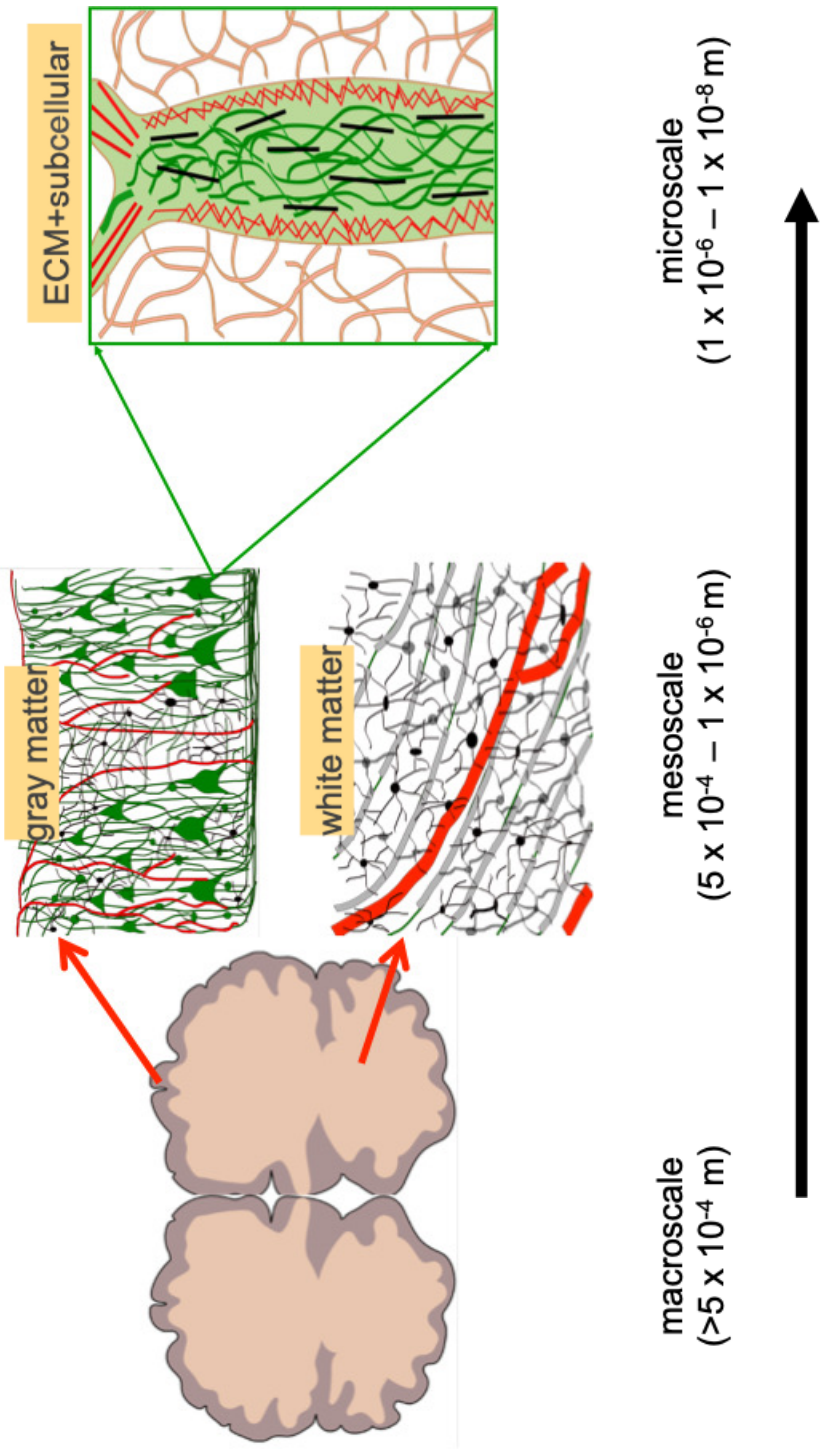

Figure 1.1: Examples of brain tissue structures at various length scales. Brain tissue at the macroscale (coronal view shown above) can generally be divided into gray matter and white matter regions–each containing their own microarchitecture. White matter contains myelinated axons, surrounded by glial cells and capillaries. The gray matter is more heavily vascularized and contains large neuronal cell bodies, also surrounded by glial cells. The mesoscale may refer to the unique cytoarchitecture of individual brain regions. At the nanoscale, subcellular structures and extracellular matrix give cells their mechanical properties.

number of axons can vary across white matter tracts and within a white matter tract, the range is roughly between 1,000 to 13,000 axons in a 2 mm x 2 mm x 2 mm voxel [33]. Glial cells–which encompass astrocytes, oligodendrocytes, microglia, and sometimes ependymal cells– surround the axons in the white matter, and typically align themselves along the axonal directions as well [33]. In contrast, the neocortex (comprising the outer gray matter layers) contains cell bodies, unmyelinated axons, and axon terminals which radiate in a more isotropic manner. The various cytoarchitectures within the neocortex correspond to unique functional areas. The vasculature system persists throughout most regions of the brain, with arterioles and capillaries contributing to the meso-/microscale architectures.

Finally, at the microscale (10 nm - 1 μm), the subcellular components (nuclei, cytoskeletal components, etc.) and the extracellular matrix (proteoglycans, lecticans, etc.) help provide cells with structural rigidity as well as assist in a wide range of biological functions. The cytoskeleton in all eukaryotic cells can be classified into three categories: actin (7-9 nm in diameter), microtubules (24 nm in diameter), and intermediate filaments (10 nm in diameter), as depicted in Fig. 1.2. While actin and microtubules are present in all brain cells, the specific types of intermediate filaments present will depend on the cell type. F-actin is a filamentous protein that is formed by the polymerization of monomeric G-actin subunits. Microtubules (MTs) are hollow cylindrical structures assembled from dimers of α-tubulin and β-tubulin. Intermediate filaments (IFs) come in a diverse group of cell-specific molecules. For ex-

ample, keratins are expressed in epithelial cells, glial fibrillary acidic protein (GFAP) is expressed in astrocytes, and neurofilaments (NF) are expressed in neurons [34].

Unlike most organs of the body, brain tissue contains virtually no "stromal space" [35]. The fluid-filled regions outside of the plasma membrane of brain cells are collectively referred to as the extracellular space (ECS). Although the ECS makes up roughly 20% of brain tissue [36], the average spacing between cells is roughly 20-60 nanometers [37]. In other words, narrow but convoluted paths allow a continuous interconnection of the ECS. This allows the fluid within the ECS to maintain an ionic balance for Ca^2+, Na^+, K^+ and Cl^- across the cell membranes [38]. Unlike most organs of the body, the extracellular matrix (ECM) of brain tissue contains relatively small amounts of fibrous proteins like collagen and fibronectin. Instead, it contains high amounts of glycosaminoglycans (GAGs), which are highly polymerized unbranched polysaccharide chains composed of repeating disaccharide units. These GAGs are either bound to proteins (forming proteoglycans) or unbound in the form of hyaluronic acid [35, 39, 40].

The compactness of brain tissue is demonstrated in Fig. 1.3A-B, where fragments of at least 1600 cells are shown to exist in a volume of 1500 microns cubed [41] within the neocortex. Within the "3-cylinder" volume, there are 193 dendrites and 1,407 unmyelinated axons. Neurites (e.g., axons and dendrites) occupy 92% of the cellular volume, whereas glial processes occupy the remaining 8%. Note that since this study examined a piece of the neocortex (an area that is part of the gray matter), there is a

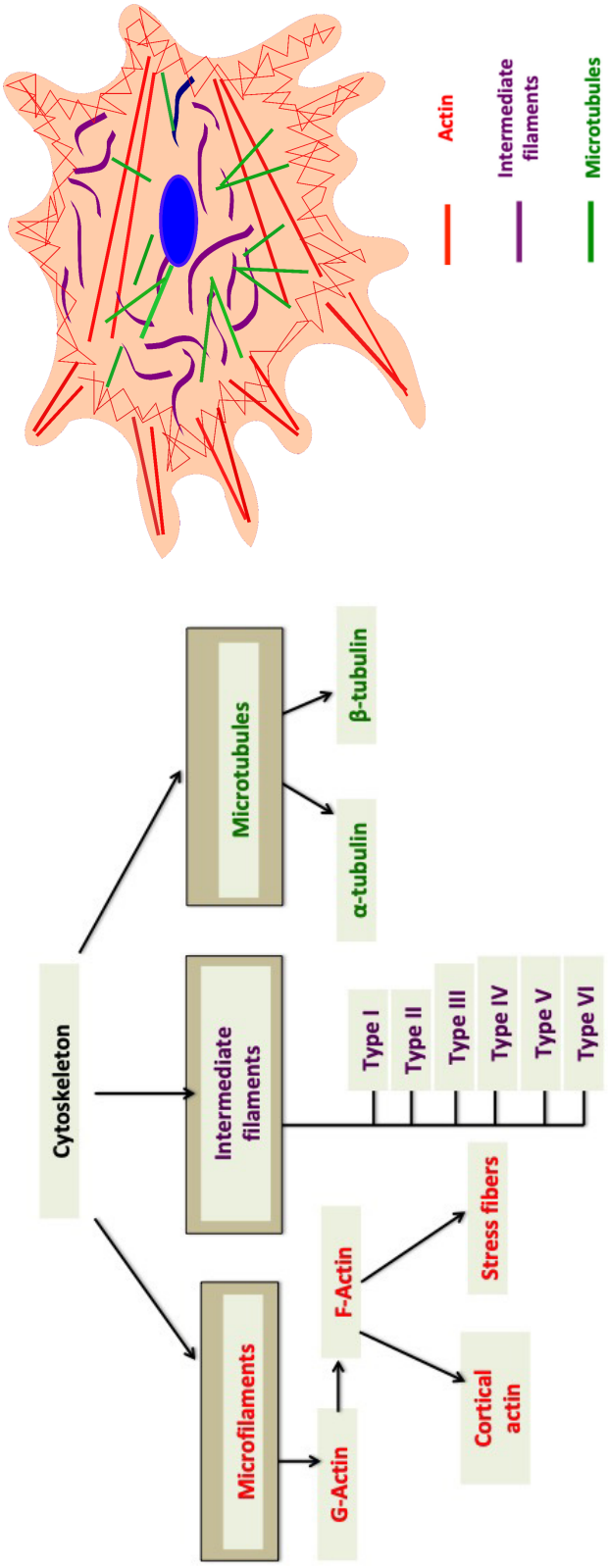

Figure 1.2: Overview of cytoskeletal structures and their subunits.

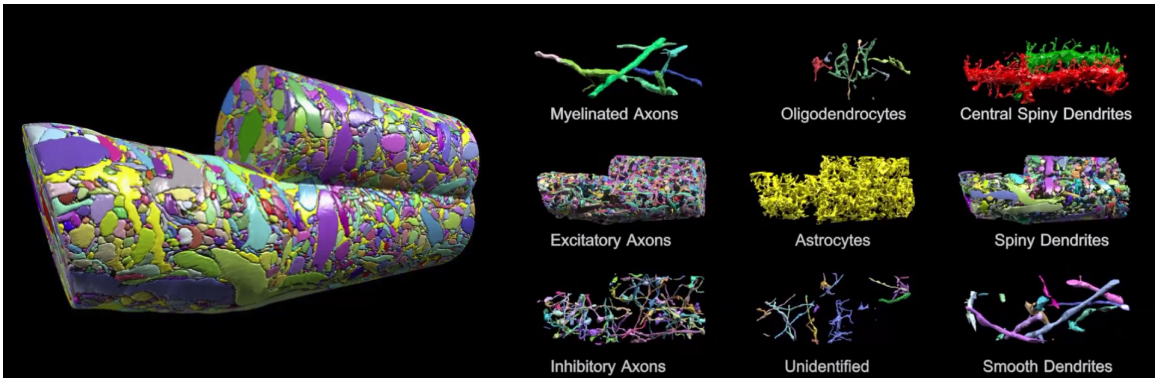

Figure 1.3: Volume reconstruction from high-throughput electron microscopy around two central dendritic spines in the neocortex. (A)Three 600 μm^3 cylinders, two of which are centered on a "red" neuron's dendrite and one on the "green" dendrite, provided a total reconstructed volume of 1500 μm^3. Diameter of each cylinder is roughly 5-10 μm. (B) Segmentation into axons (left), glia (middle), and dendrites (right). (Adapted from Kasthuri et al. 2015).

higher ratio of number of neurons to non-neuronal cells than in comparison to white matter [42]. Overall however, the nonneuronal/neuronal ratio in the whole human brain is close to 1 [42, 43].

1.1.2 Mechanical properties of CNS cells

A summary of previously reported mechanical properties of CNS cells (for both neurons and glial cells) is shown in Fig. 1.4. There is an enormous disparity in the reported values of Young's modulus, ranging from < 100 Pa to > 100kPa. However, the majority of studies seem to report a relatively low Young's modulus (< 1 kPa). Note that at the macroscale, the measured shear modulus for various regions of brain tissue is 0.4-1.4 kPa [20], which corresponds to an elastic modulus of roughly 3 kPa

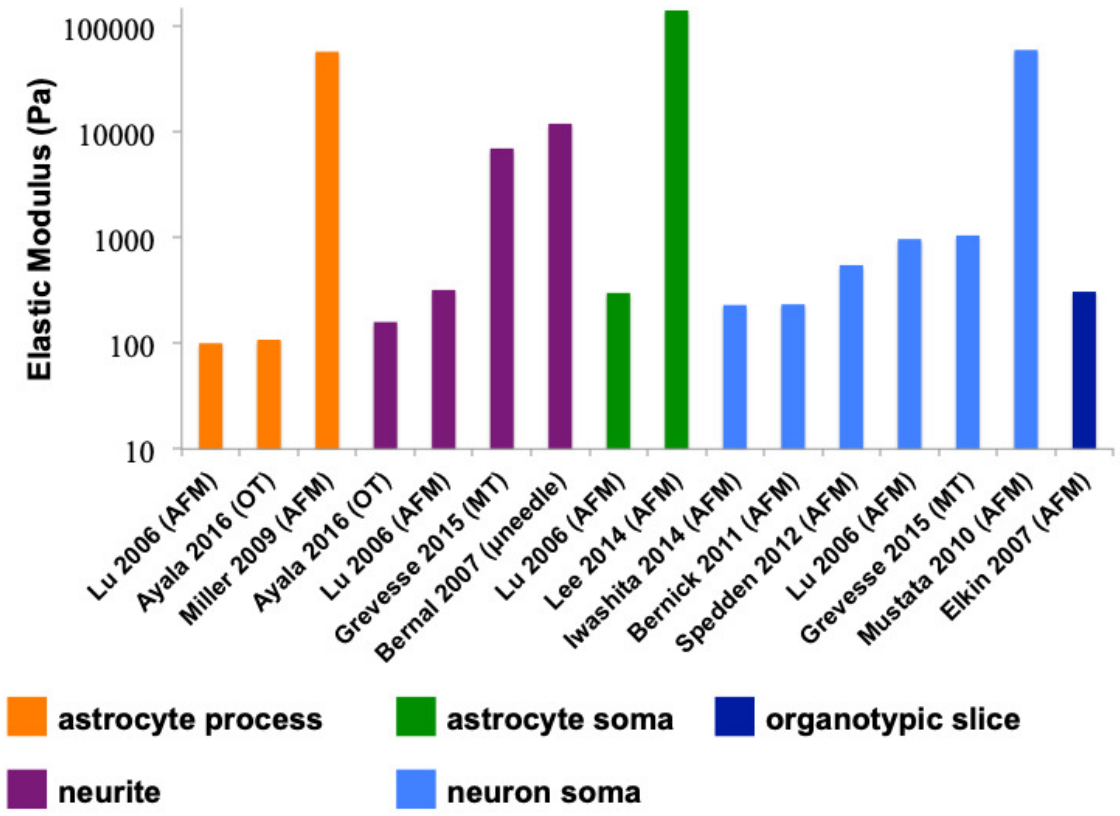

Figure 1.4: Summary of measured brain cell elastic modulus in previous reports [1–10]. When a complex Young's modulus is provided, only the value for the elastic storage modulus is shown. The corresponding technique used is shown in parentheses: atomic force microscopy (AFM), optical tweezers (OT), magnetic tweezers (MT), and microneedle bending (μneedle). Colors correspond to the specimen type probed.

in the small strain regime.

The large deviation in cellular mechanical properties is not only attributed to the heterogeneity between cellular compartments, but also the experimental method and analysis used [44]. The studies with the highest reported stiffness in Fig. 1.4, where $E >> 10$ kPa, are all taken with indentation testing using a sharp pyramidal tip– an approach which has been shown to consistently overestimate stiffness values by incorporating measurable contributions from the underlying hard substrate [45] and

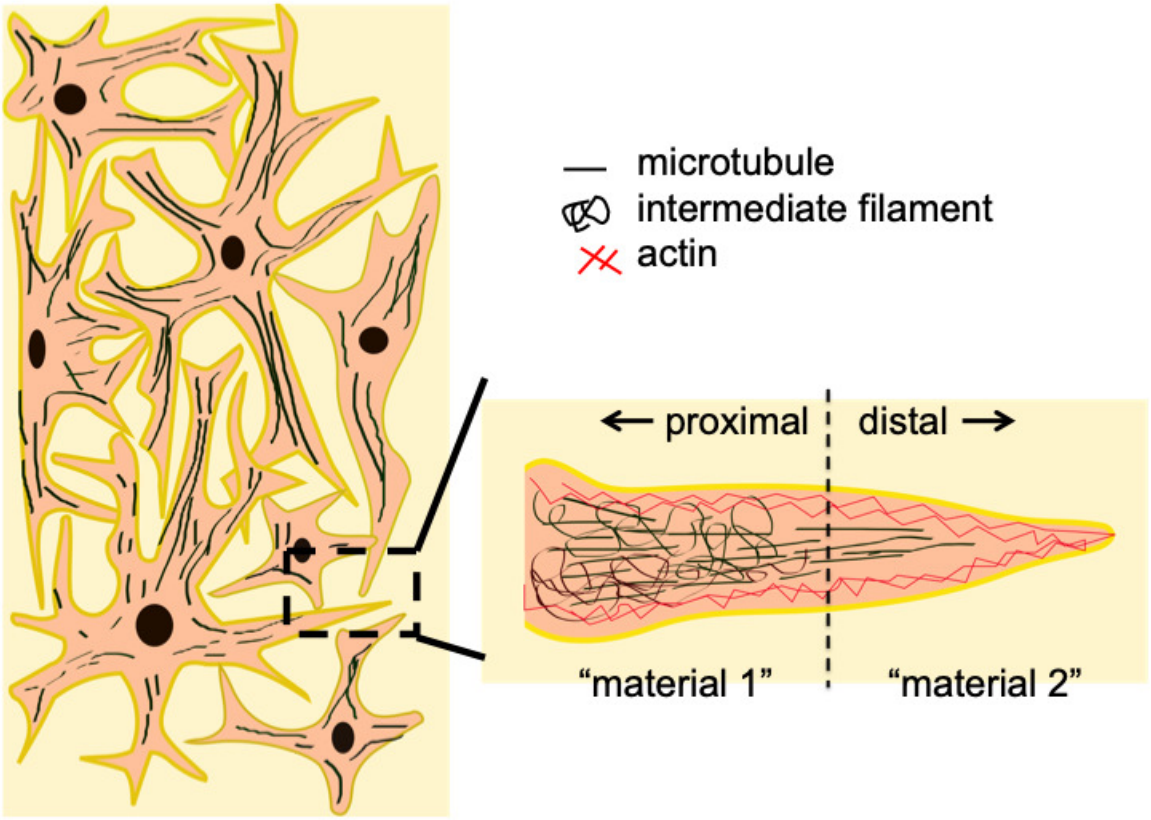

Figure 1.5: The mechanical properties of brain cells are a function of the underlying cytoskeleton. Proximal processes, which are larger and closer to the cell body, contain a mix of actin, intermediate filaments, and microtubules. For smaller, distal glial cell processes, there exists less variety in cytoskeletal components. The average effective mechanical response of the proximal components ("material 1") would presumably behave different than the average response of the distal components ("material 2").

also probing a smaller localized area [46]. Additionally, some of these experiments apply small strain theories to experiments where there is large deformation. In most cases, this would overestimate the Young's modulus.

When reporting on the mechanical properties of cells, it is important to do so with respect to both cell type as well as specific cell compartments [47], as demonstrated in the studies summarized in Fig. 1.4. For glial cells and neurons, the mechanical prop-

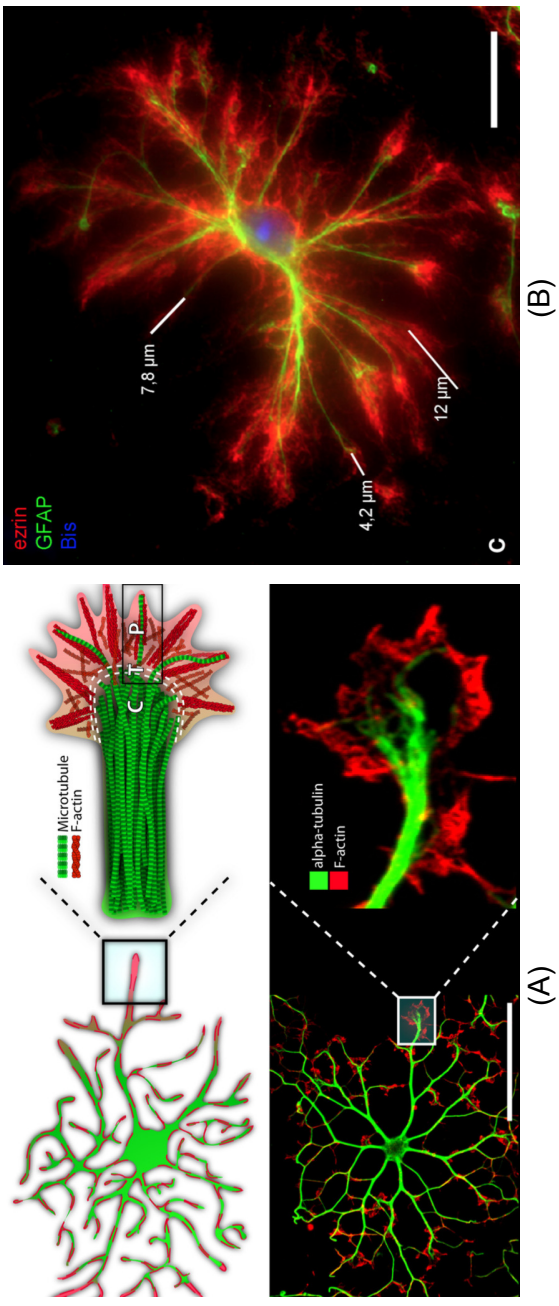

Figure 1.6: (A) Microtubules (depicted in green) run along parallel to oligodendrocyte processes. Although F-actin (red) is found throughout the cell, it is most heavily concentrated at the growing ends. For peripheral processes, we see the transition of three domains: a microtubule rich central (C) domain, an F-actin rich peripheral (P) domain, and a transition (T) domain where microtubules and F-actin overlap. Oligodendrocytes contain very few microtubules in smaller, peripheral processes (scale bar=50 μm). Adapted from [11]. (B) Ezrin (red), a protein that links the plasma membrane to F-actin, covers the entire astrocytic surface. Astrocytes lack GFAP (green) in peripheral processes. The mean length of the astrocytic processes are also depicted (scale bar=15μm). Adapted from [12].

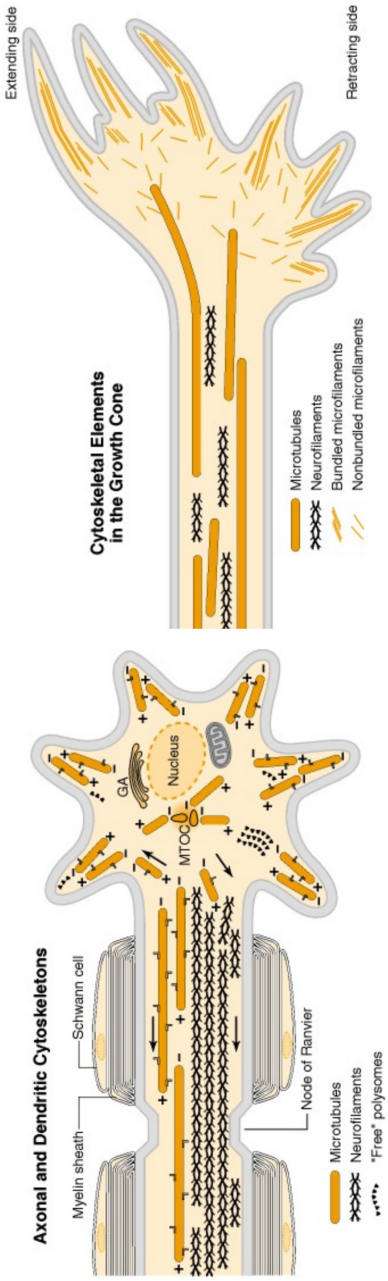

Figure 1.7: Cytoskeletons of the neuron are compartment-specific. (A)Comparison of cytoskeletal components within the axon and dendrite. (B) Cytoskeletal components of a neuronal growth cone are lacking in microtubules. Adapted from [13].

erties in various cell compartments (cell bodies versus cell processes) differ [1, 48]. Within the individual studies presented in Fig. 1.4, it appears that some studies demonstrate neuronal and astrocytic processes are slightly less stiff than their soma counterparts (e.g. Lu et al.), while other studies indicate the opposite (Grevesse et al.). Several studies have shown that regions closer to (or including) the cell nucleus show higher stiffness values [49–51]. However, other studies have shown that subcellular heterogeneities can contribute to higher overall elastic moduli in regions farther away from the cell soma [52]. In summary, there is agreement in the community that cells exhibit heterogeneous mechanical properties between their compartments, but the relative stiffness between these compartments is still an ongoing area of research.

Figure 1.5 shows a schematic of how the heterogeneity of mechanical properties in brain cells is a function of location (or compartment) within a cell since the composition of cytoskeleton constituents at the microscale will influence mechanical properties at the mesoscale. For both glial cells and neurons, the proximal cell processes (closer to the cell body) are larger and contain a mix of microtubules, intermediate filaments, and actin. For smaller and more distal processes/neurites, there are less microtubules and intermediate filaments. Therefore, compartmental properties are also likely to be heterogeneous across length scales due to variations in the underlying cytoskeleton.

Examples of heterogeneity in the cytoskeletal components of brain cells are shown in Figures 1.6 and 1.7. Fig. 1.6 shows the variation of cytoskeletal components in smaller processes of oligodendrocytes (Fig. 1.6A) and astrocytes (Fig. 1.6B). In

both oligodendrocytes and astrocytes, for example, microtubules are less prevalent in smaller and more peripheral processes and mainly localize to the soma and main processes. Fig. 1.6A demonstrates the lack of microtubules in the finer, distal process of an oligodendrocyte. Additionally, certain intermediate filaments are co-localized with microtubules near the cell bodies and larger processes, as shown by the lack of GFAP expression in distal astrocytic processes in Fig. 1.6B.

In neurons, the axonal, dendritic, and cell body cytoskeletons also differ in composition from one another. Although both types of neurites (axons and dendrites) have microtubules, neurofilaments are largely excluded from the dendritic compartments (Fig. 1.7A). Neuronal growth cones, which are very small extensions of neurites seeking new synapses, are essentially filopodia and lamellipodia comprised of mostly actin [13] (Fig. 1.7B).

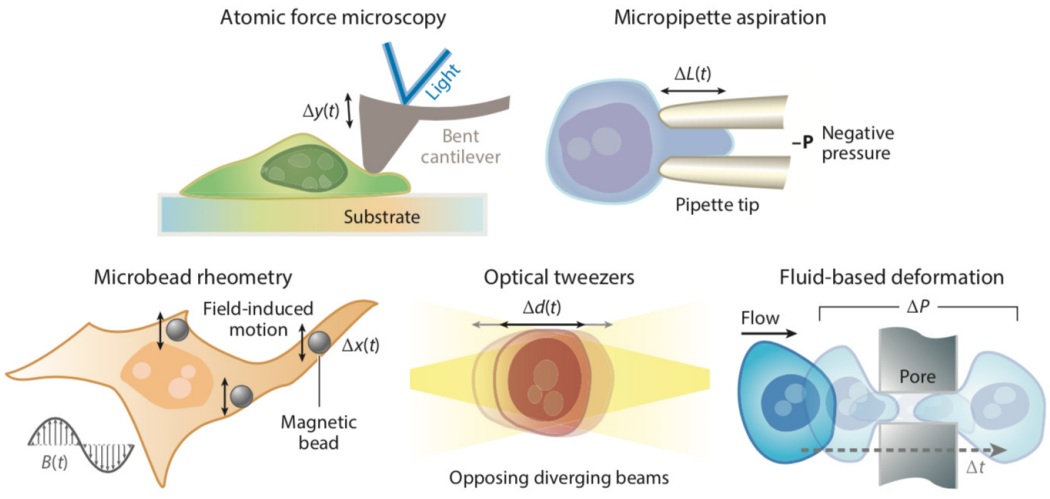

Figure 1.8: Various experimental techniques used to obtain mechanical properties of cells [14].

1.1.3 Conventional experimental techniques

An overview of previously used techniques for measuring mechanical properties of cells is shown in Fig. 1.8. Cell poking, cytoindentation, and atomic force microscopy (AFM) are indentation techniques where a known applied force is measured simultaneously with the deformation (indentation depth) response of a cell [53,54]. Based on the indenter geometry [55], specimen geometry [56], and potential interface interactions [57,58], an appropriate theoretical model is fit to the measured force-indentation data in order to obtain the material properties.

In a similar manner, magnetic tweezers and optical tweezers can also be utilized in an indentation approach by applying a known force with a trapped bead (i.e., indenter) to a cellular body [59]. In many cases, magnetic tweezers are applied to magnetic twisting cytometry, which rotates a bead that is biochemically adhered to the cell surface [60,61]. Magnetic microbead rheometry has an advantage over other techniques since it can provide mechanical properties of multiple locations simultaneously [59].

Optical tweezers, which will be discussed in more detail in Chapter 3, utilize a highly focused laser beam to trap particles in three-dimensional space with a known amount of force. They can also be modified by combining two laser traps, as shown in Fig. 1.8. This arrangement, also called an optical stretcher, works by placing cells between two nonfocused laser beams and stretching them with a known force [62,63]. In the case of using a trapped silica bead as an indenter [64], the optical trap must contain one highly focused laser beam (instead of two nonfocused laser beams).

Although the optical stretcher can achieve higher overall loading forces (100's of pN) than an optical trap (30 pN), the optical stretcher is applied to non-adherent cells in suspension [62, 63].

Another alternative to indentation-type mechanical measurements is micropipette aspiration (MA). This technique involves applying a suction pressure to a cell while monitoring the deformation of the cell into the micropipette [65, 66]. MA can be used to obtain mechanical properties of cells, both in local regions and as a whole-cell measurement, although it is usually limited to measuring viscoelastic creep-like responses of cells over long time scales [67].

Finally, fluid-based deformation cytometry utilizes a pressure gradient to pass cells through microchannels, while monitoring the deformation behavior [14]. Although this technique has potential for high-throughput applications, it requires more work in validation and verification to improve its accuracy [13].

1.1.4 Thesis aim and organization

In the following chapter (Chapter 2), we describe a specific example in which a computational model of the mechanical response of brain tissue can be used to help explain the neuropathological observations of perivascular damage patterns surrounding arterioles in postmortem TBI patients exposed to football and military head injuries. Chapter 2 demonstrates that it is important to incorporate the heterogeneity and anisotropy of brain tissue at the mesoscale in order to improve quantitative

accuracy.

Given the complexity of cellular networks and the heterogeneity within cells, we aim to further our understanding of the mechanical response of cellular constituents in order to simplify mechanical models of the brain at the mesoscale ($1 - 10^2$ microns). In order to simplify the complexity of brain tissue mechanical properties, we seek to answer the question:

Is there a maximum length scale at which cellular compartments in brain tissue have homogeneous mechanical properties?

To address this question, we developed a system which performs indentation via optical trapping to probe the mechanical properties of glial cells grown in a 3D scaffold environment at various strain rates (1-300 s^{-1}). Chapter 3 provides an in-depth description of the novel experimental platform we created. As glial cells take on extremely different morphologies when grown on 2D substrates versus a 3D environment (shown in Fig. 1.9), we grow the cells in a porous polymer scaffold, and perform indentation with an optically trapped bead to obtain nonlinear mechanical properties within a more native environment. Although optical trapping has been used in the past to obtain mechanical properties of non-adherent cells in a 3D environment (see work on red blood cells by Dao et al. [62]), this is the first time that an experiment has been designed to obtain mechanical properties of adherent cells in a 3D environment.

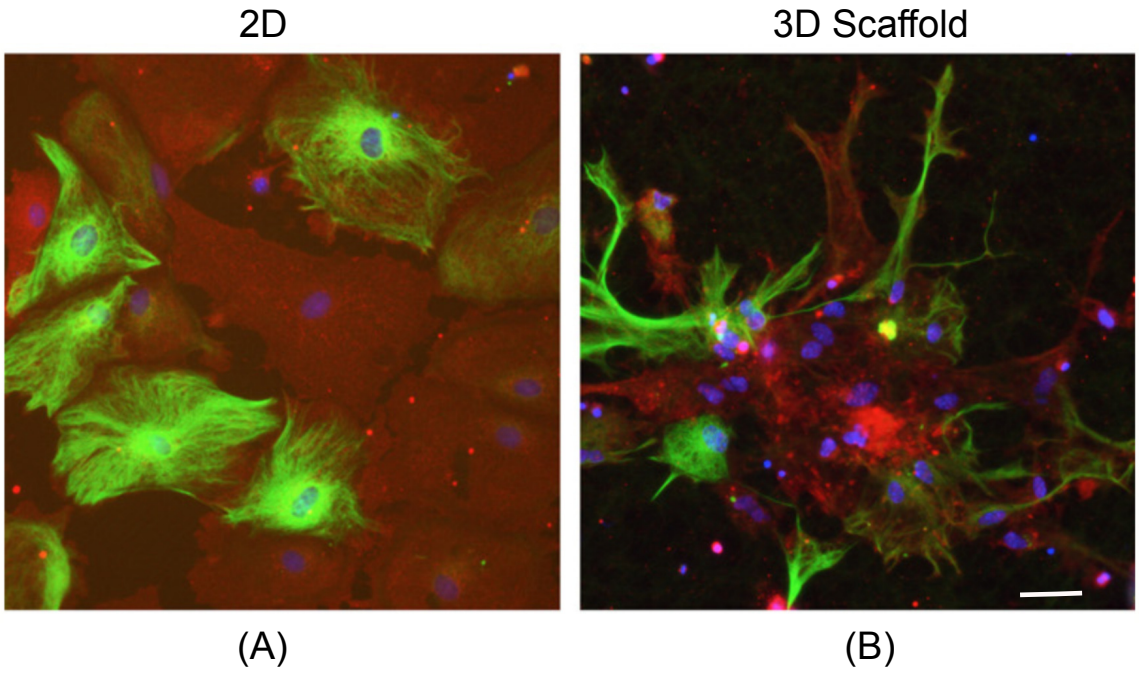

Figure 1.9: Comparison between astrocytes grown on a 2D substrate versus 3D scaffold. Astrocytes show a more polygonal morphology with smaller processes when grown on 2D substrates. Green= intermediate filament GFAP, red = glutamate synthetase, blue = DAPI. Scale bar=30 μm. Adapted from [15].

Chapter 4 provides the theoretical framework to evaluate the optical trap experiments by developing a modified force-displacement relationship that is useful for the indentation of hyperelastic cylindrical bodies. As discussed in the preceding section, the vast majority of experimental data on CNS cells (and all biological cells, for that matter) only report values for an elastic modulus or viscoelastic parameters, which are parameters that are only useful for small deformations. Since cells are soft materials which are often subjected to large deformations, a measure of the hyperelastic properties of the cell is more appropriate for future mesoscale models. Although sphere-cylinder linear elastic contact models exist, and hyperelastic indentation for-

mulations exist for indentation of flat specimens, there were no previously developed theories for the contact between a spherical indenter and a hyperelastic cylindrical specimen. The nonlinear contact theory developed in Chapter 4 is then applied to the indentation experiments described in Chapter 5.

The hyperelastic properties obtained from our experiments are discussed in Chapter 5. Glial cells are conventionally characterized as the the softer cells [1] which surround and support neurons (as an "isotropic matrix"). We seek to better understand their relative contribution to the mechanical response at the mesoscale by obtaining the hyperelastic material properties found for glial cell processes at different indentation depths and strain rates.

Finally, Chapter 6 provides a summary of the key findings and discusses limitations and potential future work. The hyperelastic material properties from our experiments provide a possible length scale, although perhaps not the maximum length scale, at which mesoscale models of brain tissue can be homogenized for future computational models.

Chapter 2

Cerebral arteriole inflation: the importance of mesoscale material properties

An increase in arterial pressure within the cerebral vasculature appears to coincide with ischemia and dysfunction of the neurovascular unit in some cases of traumatic brain injury. In this study, we examine a new mechanism of brain tissue damage that results from excessive cerebral arteriole pressurization. We begin by considering the morphological and material properties of normotensive and hypertensive arterioles, and present a computational model that captures the interaction of neighboring pressurized arterioles and the surrounding brain tissue. Assuming an axonal strain-induced injury criterion, we find that the injury depends on vessel spacing,

proximity to an unconfined free surface, and the relative difference in stiffness between the arterioles and the surrounding tissue. We find that a steeper heterogeneity (stiffer vessels surrounded by softer brain tissue) causes larger axial strains to develop at some distance from the arteriole wall, within the brain parenchyma. For a more gradual heterogeneity (softer vessels), we observe more larger strain fields close to the arteriole walls. Both deformation patterns are comparable to damage seen in previous pathology studies on post mortem TBI patients. Finally, we use an analytical model to approximate the interplay between internal pressure, arteriole thickness, and the variation in mechanical properties of arterioles.

2.1 Introduction

The high energy demands of the human brain require a complex and extensive vascular architecture to deliver the nutrients necessary to maintain normal neuronal and glial function. The cerebral arterioles—which carry oxygenated blood from the larger arteries to the capillary bed—can create a pressurized bottleneck following injury or disease states [68], [69], partially attributed to the fact that penetrating and parenchymal arterioles are largely unbranched vessels with a high resistance to flow [70]. Although capillaries individually demonstrate high flow resistance due to their small diameters, the number of capillaries greatly exceeds the number of arterioles, causing the pressure drop across the arterioles to be larger the pressure

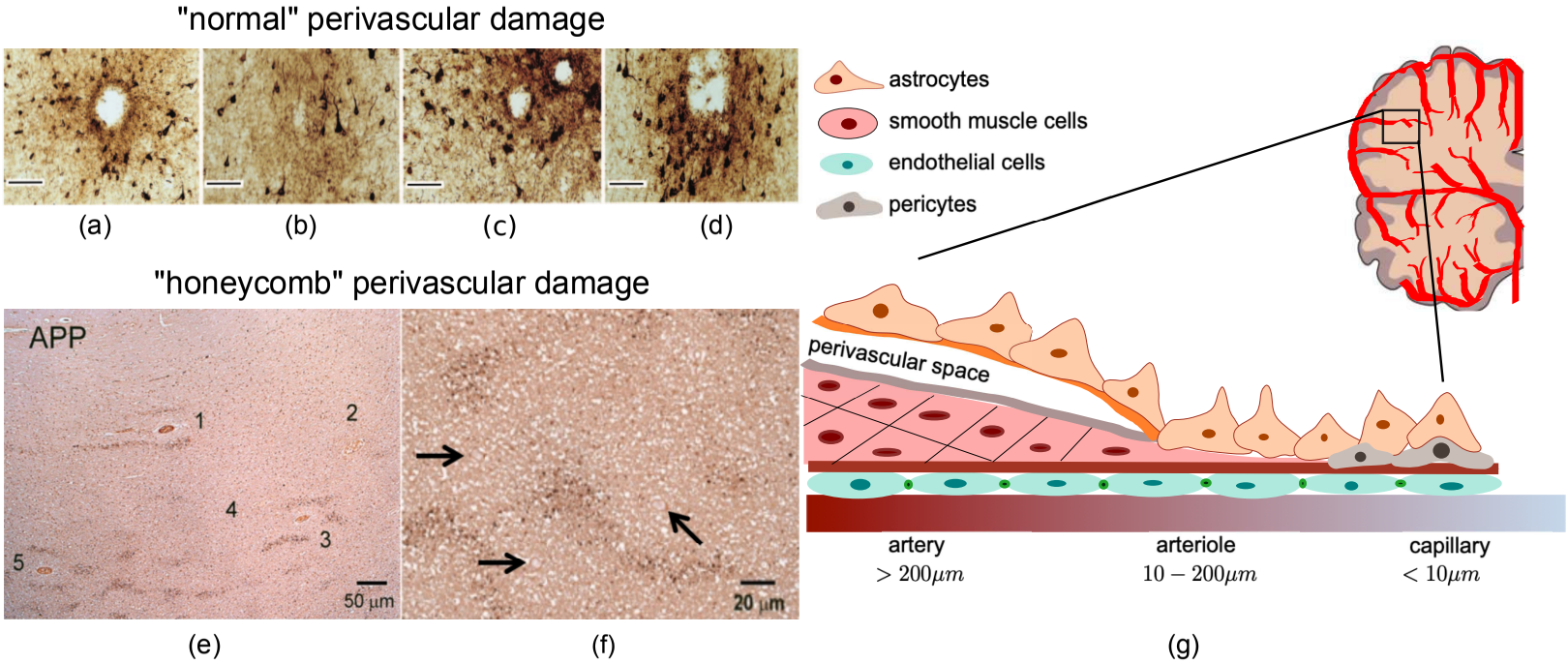

Figure 2.1: Neuropathology of post-mortem TBI patients often reveals damage surrounding small cerebral vessels, at the length scale of arterioles/venules. **(a-d)** Phosphorylated tau (CP-13) is highly expressed in perivascular regions of military patients and athletes (taken from Goldstein et al. 2012 [16]). Scale bar is 100 μm. **(a)** Phosphorylated tau with neurofibrillary degeneration in the frontal cortex of a military veteran with exposure to a single blast event. **(b)** Phosphorylated tau in the frontal cortex of a military veteran with exposure to two blast events. **(c)** Frontal cortex of an amateur American football player with repetitive subconcussive injury. **(d)** Frontal cortex of another amateur American football player with repetitive subconcussive injury **(e-f)** Example of amyloid precursor protein (APP) staining of neuronal damage surrounding arterioles in military veterans subjected to blast exposure (taken from Ryu et al. (2014) [17]). Neuronal damage appears around arterioles (labeled 1 and 3) but not venules (labeled 2 and 4) in **(e)**. Damage appears to create a "honeycomb" pattern that localizes near the midway point between arterioles (black arrows) in **(f)**. **(g)** Schematic of cerebral arterial system. We are interested in over pressurization of arteriole vessels (length scale on order of $10 - 200\mu m$).

drop across the capillaries due to a larger total cross sectional area [71]. While larger arteries can possess anywhere from 2-20 layers of circumferentially oriented smooth muscle cells (SMCs) [70], most arterioles have only one layer that surround the endothelial layer. Pericytes replace smooth muscle cells as the cerebral arterioles gradually branch into capillaries, although the transition is not well-defined [72]. Hereafter, we will refer to arterioles as the arterial vessels having diameters in the 10-200 μm range.

A transient rise in arterial blood pressure following brain injury is known to be responsible for functional, morphological, and metabolic abnormalities in cerebral arterioles and arteries [73]. In some cases of TBI, the blood-brain barrier function is compromised [74, 75] and the process of autoregulation is disturbed such that normal arteriolar constriction does not occur [76]. This may be due to loss of a pressure-induced myogenic response, since in cases when the rise in blood pressure is eliminated, these abnormalities are no longer seen [77]. Although it is intuitive that increased arteriole pressurization will generate mechanical loads on the the arteriole wall itself, the extent and consequences of this loading are relatively uninvestigated. Post-mortem studies of traumatic brain injury patients demonstrate that in addition to changes in arteriole vessel morphology [73, 78, 79], damage to perivascular regions surrounding small vessels can also occur [16, 17, 80–83] as shown in Fig. 2.1. Due to the clinical relevance of cerebral arteriole pressurization, we aim to address the following questions: Could a state of pressurized arteriole inflation lead to the dam-

age patterns shown in the pathological findings of Figure 2.1? What determines if neuronal damage occurs close to the vessel wall (Figure 2.1a-d) versus farther from the wall (Figure 2.1e,f)?

We address these questions using well-accepted concepts on strain-based damage thresholds for brain tissue [26, 84–86]. Stretching of tissue could result in cellular dysfunction by 1) creating a biochemical imbalance due to non-specific cell membrane openings and 2) directly damaging the cytoskeletal structure within the cells. Our interest is in understanding the likelihood of such deformation-induced injury as a result of arteriole overpressurization. If we idealize the arteriole pressurization problem as the inflation of a cylindrical void in a homogeneous medium, we expect the largest strains at the interface closest to the cylindrical void. However, due to the mechanical differences between the arteriole wall and surrounding brain tissue, as well as interacting deformation fields, it is possible that larger strains may also develop at some distance offset from the cylindrical void.

We begin by presenting a 3D finite element model (FEM) to observe the three-dimensional nature of the mechanical interactions between neighboring arterioles. We consider two cases of arteriole inflation (a healthy arteriole versus an arteriole with a high sclerotic index) to see how the variation of stiffness and thickness of the arteriole wall affect the deformation of surrounding tissue. Next, we discuss how greater het-

erogeneity generates higher strains away from the arteriole wall, potentially leading to neuronal dysfunction. Finally, we extend our analysis to an analytical model to quantitatively explore the complex interplay between material parameters and vessel spacing.

2.2 Computational model

2.2.1 FEM approach

We performed 3D simulations that incorporate the interactions of arterioles using the commercially available software, Abaqus (Dassault Systemes Simulia Corp.). For simplicity, we only consider the scenario of similar arterioles interacting (i.e. arteriole-arteriole pairs, rather than arteriole-venule interactions) as shown in Fig.2.2d. To capture the interaction between arterioles, the FE model includes a single repeating unit containing a central arteriole surrounded by four other arterioles, equally separated by a distance λ, as shown in Fig. 2.2b.

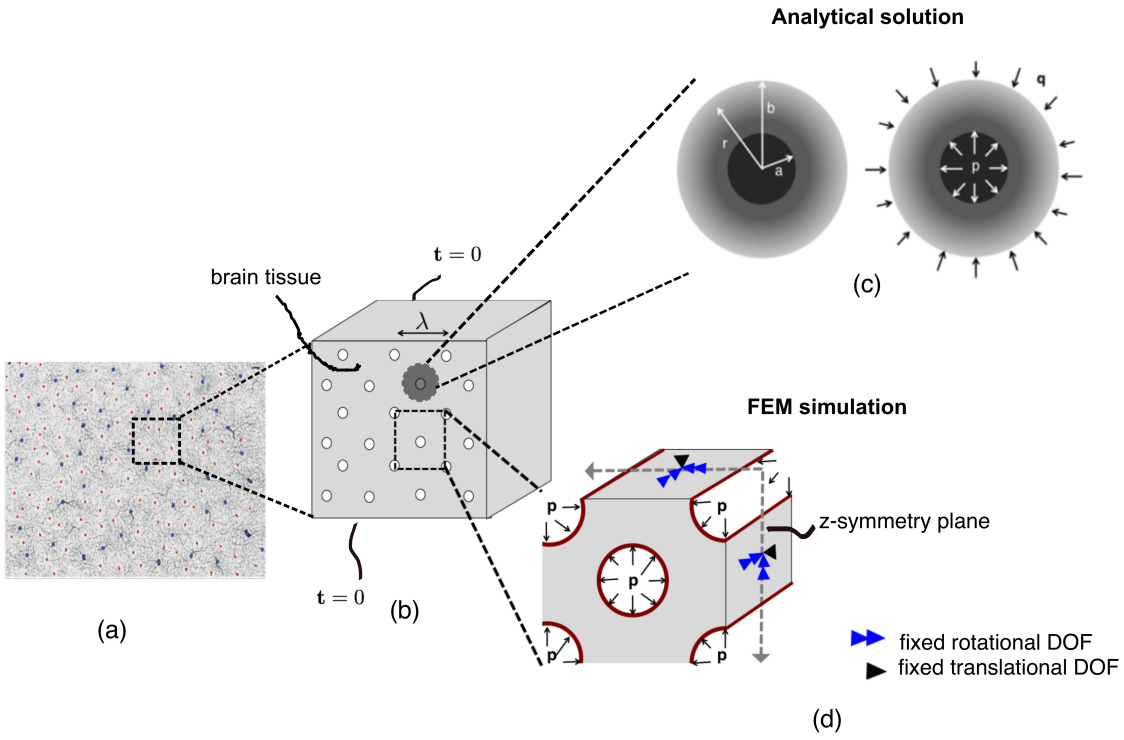

Figure 2.2: Schematic of model geometry and boundary conditions for the two solution procedures (analytical and FEM) presented. **(a)** Histology of vasculature from the macaque primary visual cortex and identification of arterioles (red) versus venules (blue) from Adams et al. (2015) [18]. **(b)** Idealized array of parallel arterioles embedded in brain tissue with spacing λ and traction-free surfaces normal to the axial direction($\mathbf{t} = 0$, front and back). Each arteriole is subjected to an internal pressure p applied at the inner arteriole wall. **(c)** Schematic of the physical constants and boundary conditions of the 2D analytical arteriole inflation model. **(d)** The repeating unit used in the FE model with depiction of symmetry boundary conditions. Blue arrows indicate the direction of fixed rotations, while black arrows indicate the directions of fixed translation. All FE models in this study used an identical arteriole inner diameter, while the spacing λ was varied.

2.2.2 Morphological and material property considerations

For all simulations, we chose an inner arteriole diameter of 35 μm based on pathology studies of cerebral arteriole diameters found in humans. Arteriole diameters in the white matter range from approximately 10 - 100 microns, with the most frequent diameters in the 30 - 40 micron range [87]. Following injury or disease, the arteriole walls can thicken and lose stiffness. Studies show that hypertension can increase the elastic components (smooth muscle and elastin) whereas collagen and basement membrane either decrease or remain unchanged [19,88,89]. To obtain realistic values of wall thickness, we utilized previously reported values for the sclerotic index (SI) of arterioles, which is defined as SI=1-(internal diameter/outer diameter). In healthy subjects, SI values are in the range of 0.2 to 0.3 in cerebral arterioles [90], while moderate small vessel disease shows an SI in the range of 0.3 to 0.5. For our finite element model of the healthy arteriole, we used a wall thickness of $t = 6$ μm, or SI of 0.25. For the case of a thickened (unhealthy) wall, we used a wall thickness of 10 μm, or SI of 0.36 (see Fig. 2.3a).

2.2.3 Arteriole spacing

Since the interaction between arterioles is a function of the spacing λ, three different spacings were investigated. High-throughput histology has shown that the

probability density function for the distance between pairs of nearest penetrating arterioles is centered between 80 - 120 microns in the cortex of mice (Blinder et al. 2013). Three different "proximity ratios," defined as the ratio of the arteriole inner diameter ($2a$) to the distance (λ) between arteriole centers, were used: 0.2, 0.3, and 0.4 (corresponding to λ =175, 116, and 88 μm for an inner arteriole diameter of 35 μm).

Experimental data describing the mechanical response of arterioles from human brain tissue is limited. The most extensive experimental data on human cerebral vasculature (Monson et al. 2005 [91]) describes larger vessels (arteries with diameters greater than 0.6 mm), which are expected to have much stiffer material properties. Arteries contain several layers of smooth muscle cells (SMCs) with ECM, while arterioles contain only 1-2 layers of SMCs. Since arterioles are expected to have extremely different mechanical properties than arteries due to their lack of SMC and extracellular matrix layers, and cerebral arterioles from rats have a similar ultrastructure to human cerebral arterioles, rat cerebral arterioles are a better choice in terms of available data than large human cerebral arteries. The mechanical properties of the arterioles were determined from the experimental data of Baumbach et al. (1988c) [19] , where in vivo inflation tests were performed on rat pial arterioles of normotensive and previously hypertensive rats (all subjected to SMC deactivation). Normotensive rat cerebral arterioles show greater strain stiffening than cerebral arterioles previously subjected to hypertension. Stress-strain curves from the Baumbach et al. data were

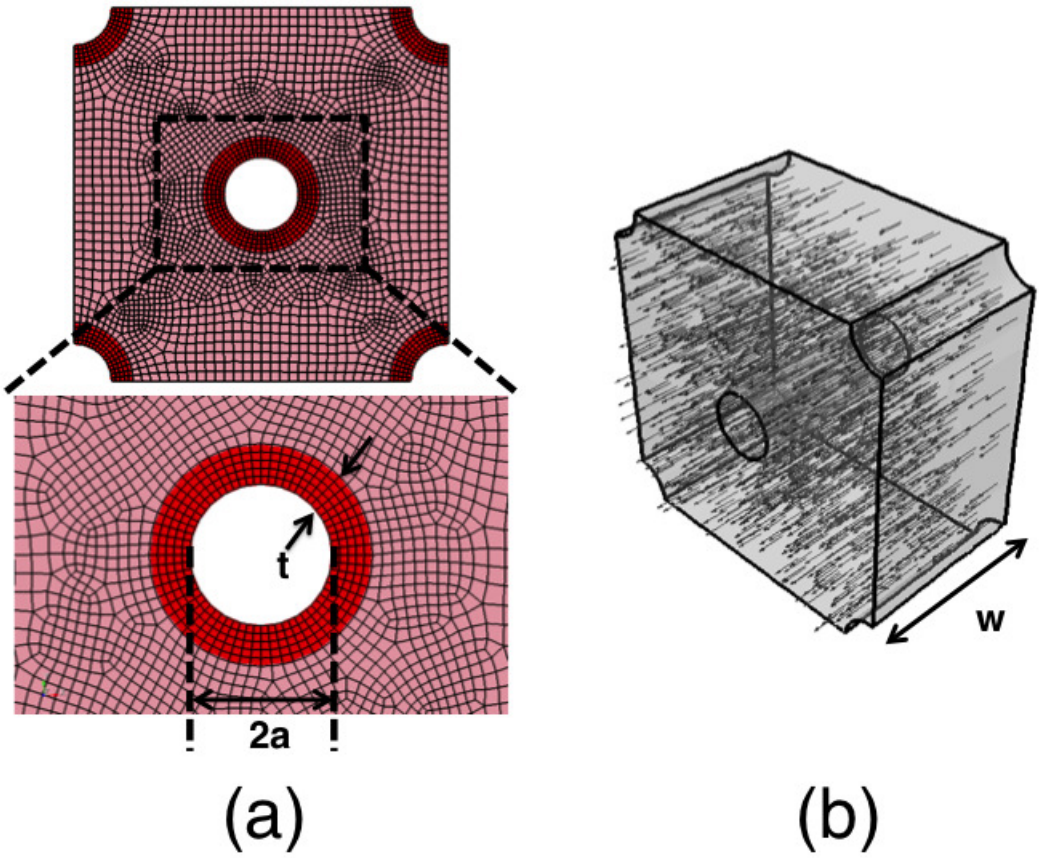

Figure 2.3: **(a)** FE model of a normal arteriole with thickness t (red elements) of 6 microns (SI=0.25) for healthy arterioles, and thickness $t = 10$ microns (SI=.36) for hypertensive arterioles. The inner diameter ($2a = 35$ microns) remained the same across models. For modeling healthy arterioles, elements within the wall thickness ($t = 6$ microns) were assigned material properties for normal healthy arterioles as shown in Table 1. For hypertensive arterioles, elements within $t = 10$ microns were assigned materials properties for hypertensive arterioles shown in Table 1. **(b)** Depiction of perfectly aligned "fiber directions" (black lines) implemented into the FE model for axons oriented parallel to arterioles.

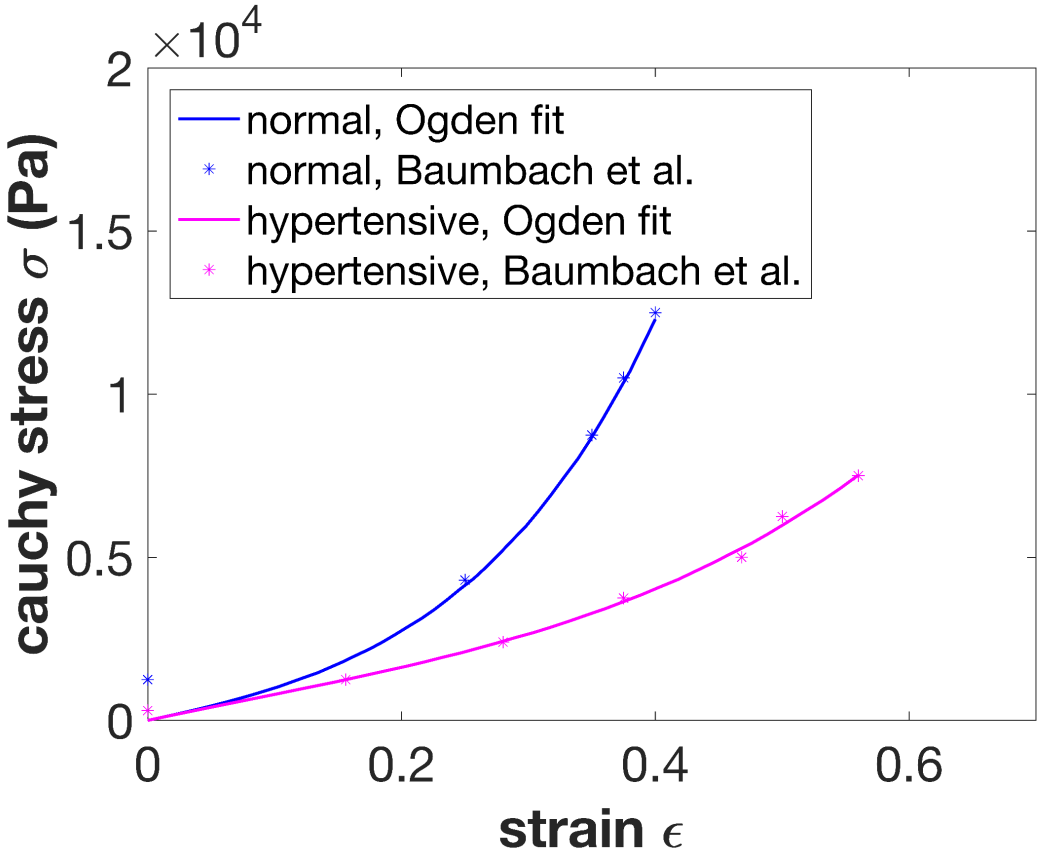

Figure 2.4: Parameter fitting for cerebral arterioles based on experimental inflation tests of rat pial arterioles from [19]). A hyperelastic Ogden model (solid lines) is fit to the experimental data ('*' line) in both normotensive and hypertensive specimens using Abaqus.

fit to an Ogden model using Abaqus (shown in Fig. 2.4). Details of the Ogden model are found elsewhere [92], but in brief, this hyperelastic model for large deformations has a strain energy W of the form:

$$W(\lambda_1, \lambda_2, \lambda_3) = \sum_{i=1}^{N} \frac{\mu_i}{\alpha_i}(\lambda_1^{\alpha_i} + \lambda_2^{\alpha_i} + \lambda_3^{\alpha_i} - 3) \tag{2.1}$$

The mechanical properties of brain tissue vary as a function of anatomical location [20, 93, 94] as well as loading direction [95]. When modeling the brain as an

isotropic material, a one-term Ogden model can represent the hyperelastic behavior of brain tissue under tension, shear, and compression loading [20]. Previous works in computational modeling of brain tissue mechanics also employ anisotropic models, typically in order to capture the additional stiffness generated when loading in the direction of axons [96–100]. In this study, we will use instantaneous shear moduli found from the corona radiata [94], and will add stiffness parameters that can incorporate the anisotropic response of cellular orientations (herein referred to as "fibers") within the tissue (see Fig. 2.3b). We chose a hyperelastic Holzapfel-Gasser-Ogden (HGO) strain energy [101, 102] for the brain tissue that takes the form:

$$W = \frac{\mu}{2}(\overline{I}_1 - 3) + \frac{k_1}{2k_2}\sum_{\alpha=1}^{N}(e^{k2<\overline{E}_\alpha>^2} - 1) + \frac{K}{2}(\frac{J^2-1}{2} - \ln J) \quad (2.2)$$

with

$$\overline{E}_\alpha = \kappa(\overline{I}_1 - 3) + (1 - 3\kappa)(\overline{I}_{4\alpha} - 1) \quad (2.3)$$

Here, μ is the shear modulus of the isotropic material around the fibers, K is the bulk modulus, k_1 is a fiber reinforcement parameter, k_2 controls the nonlinearity of the fiber reinforcement, $\overline{I}_1$ is the modified first invariant of $\overline{\mathbf{C}}$ (the distortional part of the right Cauchy-Green tensor), J is the elastic volume ratio, and $\overline{I}_{4\alpha}$ is a pseudoinvariant that is a function of $\overline{\mathbf{C}}$ and the fiber directions. The fiber reinforcement parameter is derived from experimental tensile data on brain tissue [95] by recalcu-

Part	Material model	Properties	Ref.
normal arteriole	Ogden	$\mu_1 = 2.7$ kPa, $\alpha_1 = 10.38$	Baumbach et al. 1988c*
hypertensive arteriole	Ogden	$\mu_1 = 2.4$ kPa, $\alpha_1 = 6$	Baumbach et al. 1988c*
corpus callosum (CC)	Ogden	$\mu_1 = .43$ kPa, $\alpha_1 = -22.8$	Budday et al. 2017*
corona radiata (CR)	Ogden	$\mu_1 = .85$ kPa, $\alpha_1 = -20.5$	Budday et al. 2017*
cortex (CX)	Ogden	$\mu_1 = 1.61$ kPa, $\alpha_1 = -16.6$	Budday et al. 2017*
anisotropic model for CR	Holzapfel-Gasser-Ogden	$\mu = .85$ kPa	Lee et al. 2014*, Miller and Chinzei 2002*
		$k_1 = 356$ Pa,	Velardi et al. 2006*
		$k_2 = 1 \times 10^{-9}$ MPa	
		$\kappa = 1/3$ (isotropic)	
		or	
		$\kappa = 0$ (perfectly aligned)	
		$\nu = .5$	

Table 2.1: Table of material properties used in the finite element model. *Experimental values obtained with quasi-static loading rates.

lating the fiber reinforcement parameter with the same k_1/G_0 ratio, as done in our previous computational studies of white matter [103–105]. As an example, we chose to orient the fibers perfectly aligned and parallel to the arterioles (see Fig. 2.3b).

2.2.4 Boundary conditions

The pressurized three-dimensional arterioles are arranged in an array as shown in Fig. 2.2d. The interface between the arteriole wall and surrounding tissue elements is tied with shared nodes, such that no slip or separation can occur between the arteriole and brain tissue. The model was given symmetric boundary conditions along surfaces

normal to the X- and Y- directions and the negative Z-direction, while it remained traction free ($\mathbf{t} = 0$) in the positive Z direction. These boundary conditions are similar to the conditions of arterioles which run parallel to one another and perpendicular to the surface of the brain. Symmetric boundary conditions for a face normal to direction i were: $u_i = 0$, $u_{r,i\neq j} = 0$, where u_i is the displacement in the i^{th} direction and $u_{r,i\neq j}$ are the rotational displacements in the remaining two directions (see Fig. 2.2d). A mesh convergence study was performed to ensure an adequate distribution of elements surrounding each arteriole. The mesh size was varied from 2 to 7 μm, corresponding to 15 to 50 circumferential hexahedral elements surrounding the cylindrical cavity, respectively. It was found that a mesh size of 2.75 μm (40 circumferential elements) could achieve less than 1% error of the maximum principal strain (for the finest mesh resolution) at the tissue-arteriole interface.

Although the pressure magnitudes in individual arterioles may vary, we assume that arterioles of equal radii, in close proximity to each other, will have equal internal pressures. In the simulations presented, a pressure of $p = 1$ to 5 kPa was applied to each arteriole wall surface. We do not consider the case of a single arteriole under pressurization ($q = 0$) in our simulations, since this case is well described by an analytical model (see Appendix A.2). All finite element models in the study, regardless of arteriole spacing, have a thickness along the z-direction of 100 microns from the traction-free surface. The z-depth of 100 microns was found to be sufficient with respect to our simulations, but larger depths should be considered for simulations with

larger applied loading ($p >> 1$ kPa) due to potential interactions of displacements with the z-symmetry boundary. If we define the z-depth as a parameter w, as shown in Fig. 2.3b, the ratio of $w/a = 5.71$ remained constant across all simulations.

2.2.5 FE model results

2.2.6 Effect of material parameters on damage pattern

For each proximity ratio, simulations were performed using brain tissue properties of either the corpus callosum (CC), or the corona radiata (CR), or the cortex (CX). Figures 2.5a and 2.5b demonstrate the importance of the relative stiffness between the arteriole wall and brain tissue. In both simulations the proximity ratio, internal pressurization, and material properties of the surrounding brain tissue were equal ($2a/\lambda = 0.3$, p=2.5 kPa, and CX tissue properties). In Figure 2.5a, the thickness and stiffness of the arteriole wall are normal, while the arteriole wall of Figure 2.5b has the thickness and properties of a hypertensive arteriole. If we consider a strain injury threshold of 10% [86], the stiffer arteriole results in a "honeycomb" damage pathology similar to that seen in post mortem TBI patients of Fig. 2.1e,f, while the softer arteriole results in a "normal" perivascular damage similar to Figures 2.1c,d. The "honeycomb pattern" describes neuronal damage at a remote distance surrounding

cerebral arterioles, but not around venules or capillaries [17].

Fig. 2.5c shows a plot of axial strain as a function of the distance from the arteriole center for the simulations of 2.5a and 2.5b. In comparison to the normal arteriole, the hypertensive arteriole generates relatively larger strains across all values of r. Let ρ_{th} equal the distance from the arteriole center at which strains exceed an injurious threshold. Using an injury threshold of 10% strain, the brain tissue surrounding a normal arteriole reaches injurious strains at $\rho_{th} = 97$ μm, while strains $> 10\%$ occur much closer to the hypertensive arteriole ($\rho_{th} = 55$ μm).

A summary of the maximum axial strains for each brain region and proximity ratio are shown in figure 2.5d. As expected, the highest strains (18%) can be seen for the largest proximity ratio, with the softest brain tissue (CC) and the softest (hypertensive) arteriole walls. Comparing the stiffest material properties (CX, normal arteriole) with the same proximity ratio, we see that the strains reduce from 0.18 to 0.13. For a given type of brain tissue (CC, CR, or CX), hypertensive arterioles will result in larger brain tissue strains (in comparison to normal arterioles), regardless of the proximity ratio.

2.2.7 Comparison to pathology images

Although we demonstrated that injurious strains can arise in a "honeycomb pattern," it remains to be determined if this type of injury can occur with the large spacing of arterioles shown in the histology image of the frontal cortex (Fig. 2.1f,

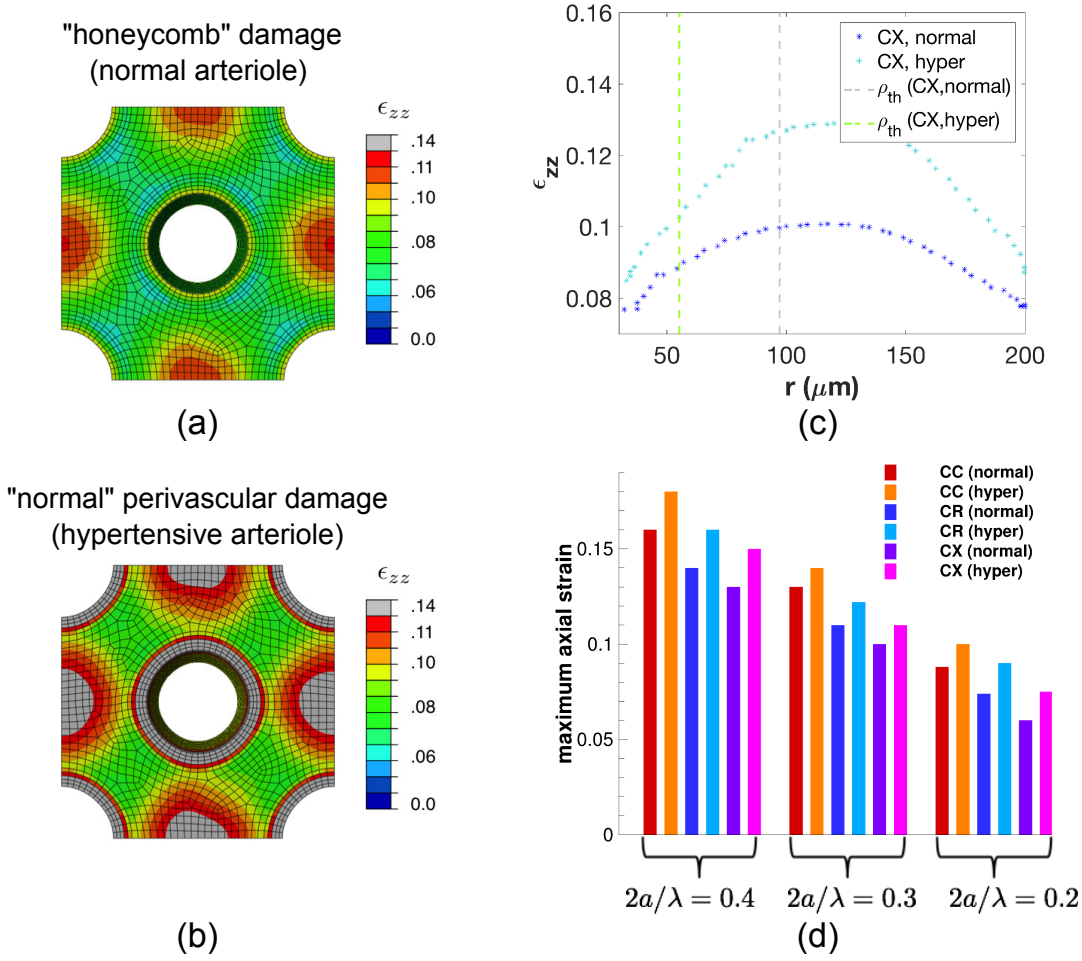

Figure 2.5: **(a)** A proximity ratio of 0.3, material properties of the cerebral cortex, and an internal pressurization of 2.5 kPa applied to a normal arteriole (steeper heterogeneity), create a damage pattern similar to the "honeycomb" pattern in some pathology studies. **(b)** Using the same conditions, except applied to a hypertensive arteriole (gradual heterogeneity), created a damage pattern similar to the "normal" perivascular pattern in previous pathology studies. **(c)** Axial strain as a function of distance from the arteriole center for the simulations shown in **(a)** and **(b)**. The dashed lines for ρ_{th} demonstrate the radially position at which strains exceed the injury threshold ($\epsilon_{th} = .10$). Both simulations are looking at a slice located at 5 μm from the free surface. **(d)** Comparison of results from 3D FEM simulations of the corpus callosum (CC), corona radiata (CR), and cortex (CX) subjected to an arteriole pressurization of 2.5 kPa. Each simulation compares normal and hypertensive arterioles. Material properties used from [20].

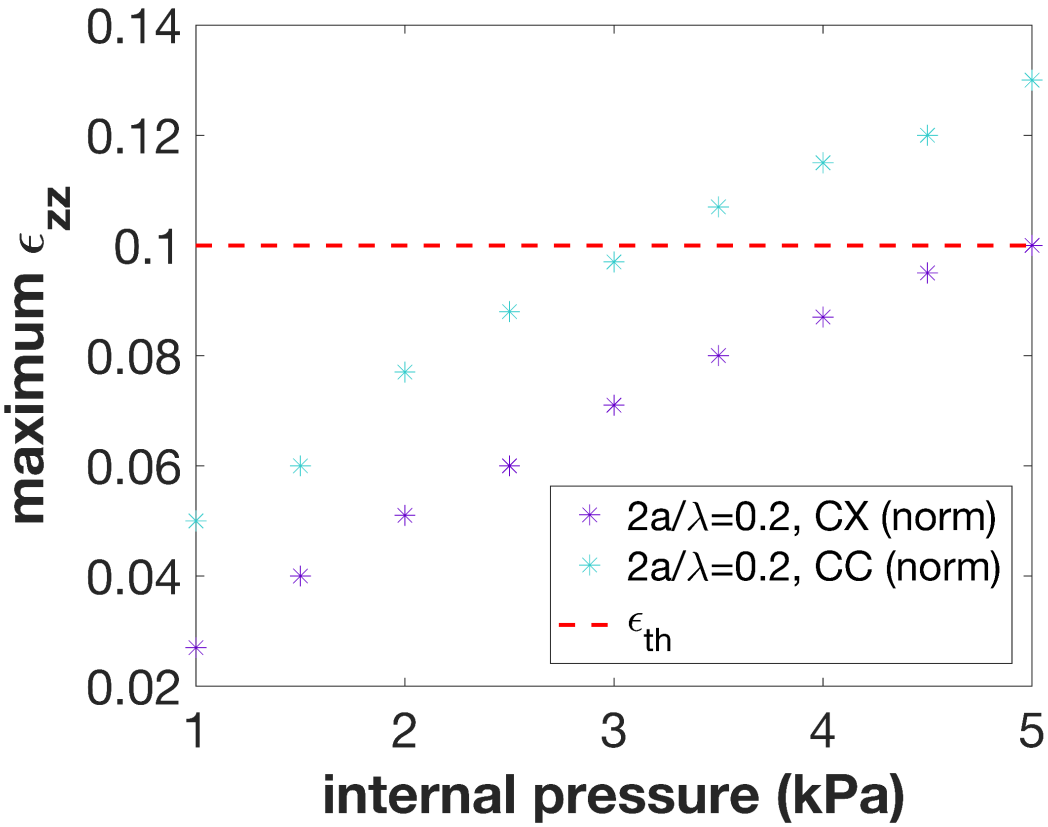

Figure 2.6: Maximum axial strain found in FEM simulations as a function of pressure for the cortex (CX) and corpus callosum (CC) for a proximity ratio similar to the pathology images of Fig. 2.1f ($2a/\lambda = 0.2$). For both the softest and stiffest types of brain tissue, a reasonable amount of internal pressure can still generate the "honeycomb" perivascular damage for largely separated arterioles.

$2a/\lambda \approx 0.2$) given a reasonable amount of pressurization. Simulations of comparable geometry and material properties to Fig. 2.1f ($2a/\lambda = 0.2$, CX tissue, normal arterioles) were subjected to increasing amounts of internal pressure, as summarized in Fig. 2.6. Again, assuming a strain threshold of 10%, an internal pressure of 3 kPa is required for the CC tissue, while an internal pressure of 5 kPa is required in the CX tissue. The magnitude of arteriole pressurization in the physiological state following injury remains unknown, however, the simulated boundary conditions (1-5 kPa) in this study are within the limit of deleterious mean arterial pressure (MAP=14 kPa) [106]. The MAP only provides an average pressure across the arterial compartments, but it is not unreasonable to assume that pressure in the arterioles would possess a similar magnitude, since a normotensive blood pressure of 15 kPa in the brachial artery corresponds to 8 kPa in the smaller parietal arterioles [107]. Thus, using a strain injury criteria of 10%, it is possible to achieve the damage pattern of Fig. 2.1f with a reasonable amount of pressurization (about 30-60% increase from the baseline pressure).

2.2.8 Effects of brain tissue anisotropy

To investigate the effects of brain tissue anisotropy, we begin by considering normal arterioles embedded in brain tissue with isotropic parameters ($\kappa = 1/3$) and a shear modulus equivalent to the corona radiata as shown in Fig. 2.7a-c. Three different arteriole spacings were simulated with an internal pressurization of 1 kPa.

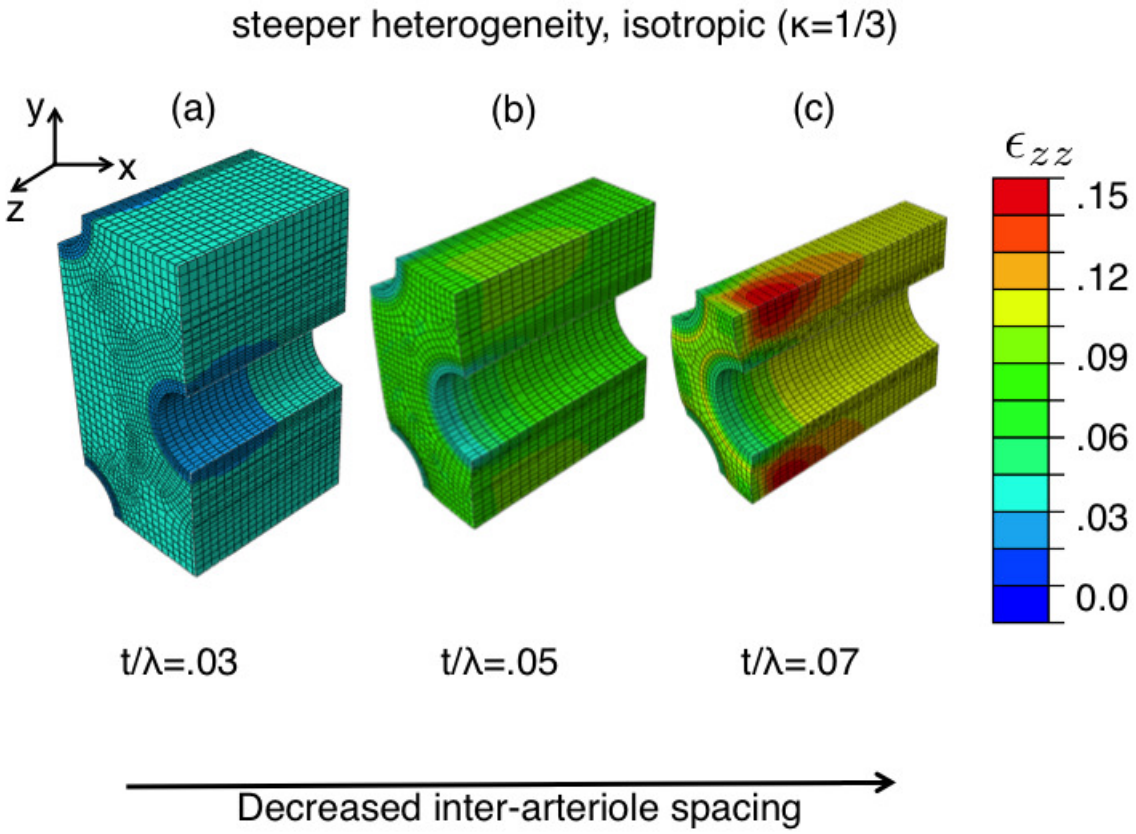

Figure 2.7: Simulations of arteriole inflation for different spacing in case of greater ($t = 6\mu$m) heterogeneity with isotropic brain tissue ($\kappa = \mathbf{1/3}$). Proximity ratios (defined as inner diameter/spacing) are 0.2 (**a**), 0.3 (**b**), and 0.4 (**c**). Z-depth (w) of the model is 100 microns for all cases. The internal pressure applied to the inner surface of the arteriole walls is 1 kPa.

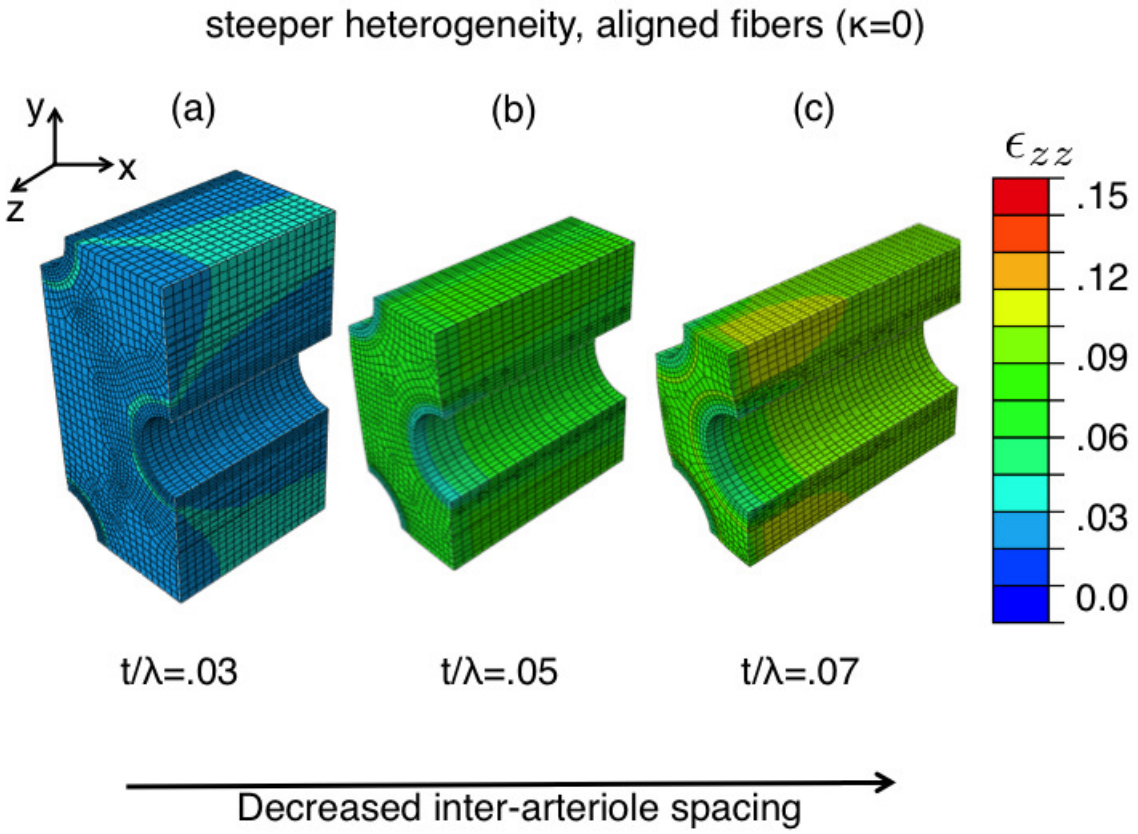

Figure 2.8: Simulations of arteriole inflation for different spacing in case of greater ($t = 6\mu$m) heterogeneity with isotropic brain tissue ($\kappa = \mathbf{1/3}$). Proximity ratios (defined as inner diameter/spacing) are 0.2 (**a**), 0.3 (**b**), and 0.4 (**c**). Z-depth (w) of the model is 100 microns for all cases. The internal pressure applied to the inner surface of the arteriole walls is 1 kPa.

For the largest arteriole spacing ($\lambda = 175\mu$m, Fig. 2.7a), the strains are relatively homogeneous and $\epsilon_{zz} < .03$ throughout the brain tissue. For the intermediate arteriole spacing ($\lambda = 116\mu$m, Fig. 2.7b), the axial strains are larger ($\epsilon_{zz} = .08$), but relatively constant throughout the tissue. In the case of the smallest arteriole spacing ($\lambda = 88\mu$m, Fig. 2.7c), axial strains reach up to $\epsilon_{zz} = .15$. Axial strains vary along the z-depth, since the tissue can expand more easily near a free surface. Immediately at the front surface, however, the axial deformation is restricted due to the tied nodes between the tissue and stiffer arterioles, which will expand less in the axial direction. This is non-physical, and would likely not occur at the surface of the brain since the arteriole would transition into a larger artery within the subarachnoid space of the brain. Thus, we are more interested in the solutions that exist at a z-depth below these constrained elements at the immediate surface.

Results for a steep heterogeneity ("normal" arterioles) and perfectly aligned transverse isotropic fibers ($\kappa = 0$) are shown in Fig. 2.8a-c. For the largest arteriole spacing ($\lambda = 175\mu$m, Fig. 2.8a), axial strains are close to zero. In the intermediate arteriole spacing ($\lambda = 116\mu$m, Fig. 2.8b), $\epsilon_{zz} = .06$, although strains are approximately homogeneous throughout the tissue. For the smallest arteriole spacing ($\lambda = 88\mu$m, Fig. 2.8c), axial strains reach 0.10. In comparison to the isotropic tissue simulations of Fig. 2.7a-c, the peak axial strains were reduced by 30% in all cases ($\lambda = 175\mu$m, $\lambda = 116\mu$m, $\lambda = 88\mu$m). This is because in the isotropic limit where $\kappa = 1/3$, there is a smaller stiffness contribution in the direction of axial strain.

In the case of normal arterioles in close proximity (Fig. 2.7c), the axial strains between the arterioles reach higher strains closer to the arteriole walls. In other words, a steep heterogeneity does not necessarily produce a "honeycomb" distribution of damage when the arterioles are in close proximity to each other. The extent of strain concentration is more complex than simply being a function of heterogeneity between the arteriole and brain tissue. In order to quantify the relative effects of internal pressure, arteriole thickness, mechanical properties, and arteriole spacing, we use a simplified analytical model (presented in the next section).

2.3 Analytical solution for arteriole pressurization

2.3.1 Analytical approach

As mentioned in the last section, the strain concentration between arterioles is a function of both material properties and arteriole spacing. An analytical solution can be used to to provide a simplified mathematical expression that quantifies the complex interplay between heterogeneity and arteriole spacing. The analytical solution presented in the following section can describe the various possible deformation fields of brain tissue surrounding either a normal arteriole (thin with high stiffness) or hypertensive arteriole (thick with low stiffness) based on the choice of model pa-

rameters.

The arteriole inflation can be idealized as an axisymmetric problem of a hollow circular disk or cylinder with a spatially varying stiffness function subjected to uniform pressure on the inner ($r = a$) and outer ($r = b$) surfaces (Fig. 2.2c). The value of $r = a$ is determined by the inner radius of the arteriole, while $r = b$ represents a distance r from the arteriole wall at which the nearby vessels create an additional pressure field q ($\leq p$) that restricts radial expansion of the arteriole (Fig. 2.2c). Referring to Fig. 2.2c, we designate the inner radius of the cylinder wall (representing the inner edge of the arteriole wall) as $r = a$ and the outer edge of the cylinder wall as $r = b$. The space occupying the region between $r = a$ and $r = b$ is a combination of both the arteriole wall and the surrounding tissue, with the arteriole wall existing closer to $r = a$.

For a thick hollow cylinder under inflation, we expect from basic mechanics principles that the radial stresses are always compressive ($\sigma_{rr} < 0$) and the tangential stresses are always tensile ($\sigma_{\theta\theta} > 0$). For the homogeneous hollow cylinder case, we also expect that the maximum value of $\sigma_{\theta\theta}$ occurs at the inner boundary $r = a$, and decreases as $\frac{1}{r^2}$ [108]. For the case of a heterogeneous cylinder, σ_{rr} and $\sigma_{\theta\theta}$ are dependent on the material properties, and the highest strains may not necessarily be restricted to the region immediately adjacent to the boundaries with applied pressure.

2.3.2 Stresses and strains with radial dependence

A spatially varying Young's modulus ($E(r)$) is used to represent a continuous medium that transitions smoothly from the stiffer arteriole wall and then decays to a final value of lower stiffness, representing the properties of the surrounding brain tissue (neurons, glia, and capillaries). With a slight adaptation of the work of Horgan and Chan (1999) [109], we can suppose that the Young's modulus varies spatially as a function of r and takes the form:

$$E(r) = E_0(\frac{r}{r_0})^n \tag{2.4}$$

where n is an arbitrary constant ≤ 0 and E_0 has units similar to E. We have modified Horgan and Chan's solution to include a lower bound E_0 for the modulus at a distance $r = r_0$ (see Fig. 2.9a). As the value selected for n becomes more negative, the function $E(r)$ begins at a higher value and drops off more quickly with respect to r. Thus, when using n values close to zero, one can approximate a "hypertensive" arteriole–a thicker arteriole wall with material properties that more closely match the softer surrounding brain tissue [19]. The derivation and final form for the radial and tangential stresses can be found in the Appendix (Section A.1). Letting $E_a = E(r = a)$ and $E_b = E(r = b)$, the resulting strain fields are given by:

$$\epsilon_{rr} = \frac{C_1}{r}(C_2 r^{m_1} + C_3 r^{m_2}) - \nu\frac{C_1}{r}(C_4 C_2 r^{m_1} + C_5 C_3 r^{m_2}) \tag{2.5}$$

$$\epsilon_{\theta\theta} = \frac{C_1}{r}(C_4 C_2 r^{m_1} + C_5 C_3 r^{m_2}) - \nu\frac{C_1}{r}(C_2 r^{m_1} + C_3 r^{m_2}) \tag{2.6}$$

$$\epsilon_{zz} = -\frac{\nu C_1}{r}(C_2(1 + C_4) r^{m_1} + C_3(1 + C_5) r^{m_2}) \tag{2.7}$$

where $m_1 = (-n-k)/2$ and $m_2 = (-n+k)/2$ for $k = \sqrt{n^2+4-4n\nu}$. The constants C_1, C_2, C_3, C_4,C_5, which are dependent on E_a,E_b, ν, m_1, and m_2, are given in the Appendix (Section A.1). For most cases, we can use the simplified expression of the analytical solution (derivation in Text S3) to determine when the axial strains begin to exceed a particular strain threshold:

$$\epsilon_{zz} \approx -\frac{\nu C_1^*}{r}(C_3(1+C_5)r^{m_2}) \tag{2.8}$$

where C_1^* simplifies to:

$$C_1^* \approx \frac{1}{E_a E_b(\frac{b^{m_2}}{a} - \frac{a^{m_2}}{b})} \tag{2.9}$$

Whether or not these strain fields will induce damage depends on the cellular architecture surrounding the arterioles. Realistically, axonal directions can be oriented either parallel, perpendicular, or off-axis to the direction of cerebral arterioles, depending on the location in the brain. For example, the arterioles of the corpus callosum are perpendicular to axons, while the arterioles of the centrum semiovale run parallel to axons [110].

From Eqn. 2.8 one can see that the axial strains will depend on: 1)the distance between $r = a$ and $r = b$, 2) the pressures p and q applied at the locations $r = a$ and $r = b$, and 3) how the stiffness of the cylinder decreases from the arteriole wall (i.e., the parameters that define $E(r)$). Since C_1* and C_3 are the only constants which depend on the arteriole spacing in Eqn. 2.8, we see that ϵ_{zz} is linearly proportional

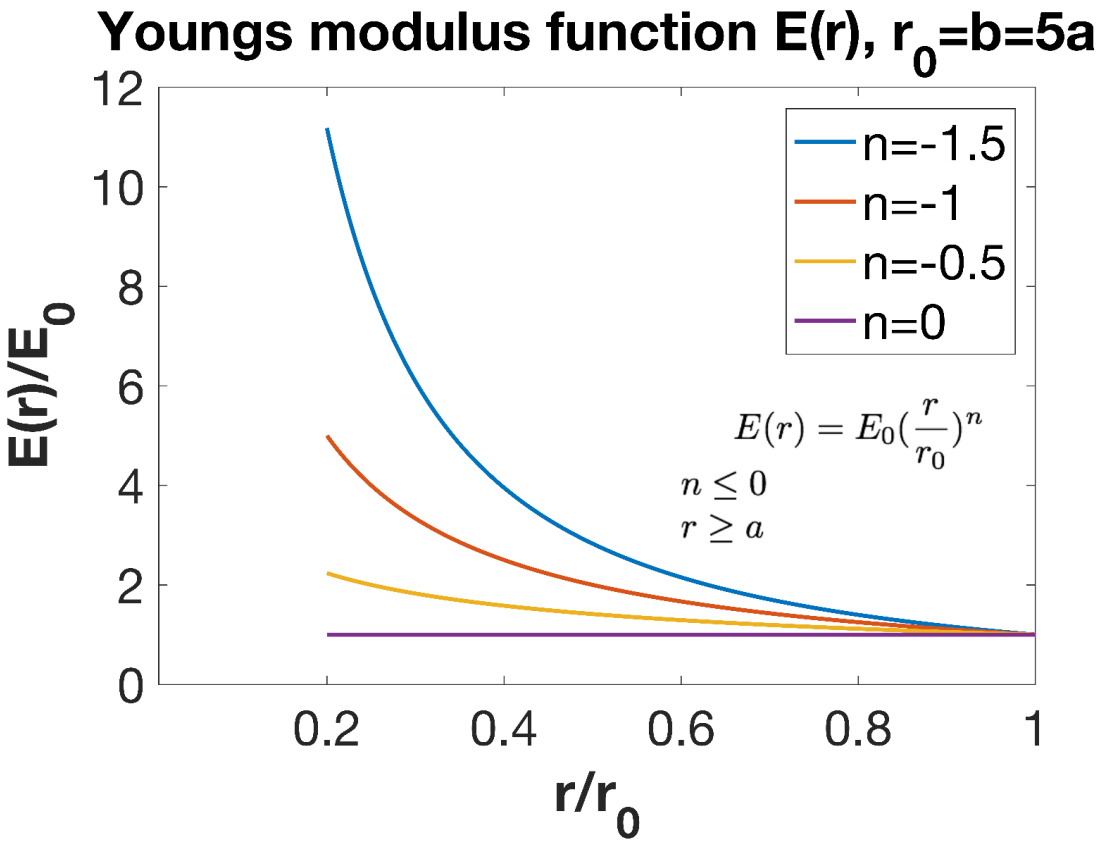

Figure 2.9: **(a)** Function describing a spatially varying Young's Modulus. In this example, the Young's modulus reaches a plateau of E_0 at a distance of $r_0 = b$, where $b = 5a$. The constant $n = -0.5$ corresponds to a more "gradual" heterogeneity (hypertensive, thick arteriole with a lower stiffness wall), while $n = -1.5$ corresponds to a more "steep" heterogeneity (healthy, thin arteriole with a stiffer wall).

to the spacing, for a given value of n. The dependence of strain on the heterogeneity is much more complicated, since m_2, C_1^*, and C_5 are all functions of n. Equation 2.8 can also be used to approximate the range at which strains become large and require the nonlinear computational model.

2.3.3 Analytical solution

To approximate the surrounding pressure field (q) from neighboring arterioles acting on the brain tissue, we will assume that the arterioles are surrounded by an "effective" field of pressurized cylindrical inclusions that occupy a volume fraction ϕ^A, where $\phi^A = \frac{\text{vol. of cylinders}}{\text{total vol.}}$. For the case of 35 micron diameter arterioles separated by $b = 3a = 116$ microns between the arteriole centers, this corresponds to $\phi^A = 0.15$. The effective pressure (q_{eff}) acting at $r = b$ will be approximately $\phi^A p$ where p is the internal pressure acting in each arteriole. Although this approximation does not take into account the stress concentrations arising around each void, Figure 2.11 shows that the expression for q_{eff} is a good approximation, given the similar magnitudes of pressure at the locations of strain concentration in the corresponding Abaqus simulation.

For the homogeneous case shown in Fig. 2.10a, the tensile and tangential stresses are independent of E_0/p. For the case of $E_0/p = 2$ and $E_0/p = 0.5$ (Fig. 2.10b), the axial strains are positive and independent of r. For smaller external pressures ($p >> q_{eff}$), the axial strains can be negative as one approaches the $q = 0$ case (not

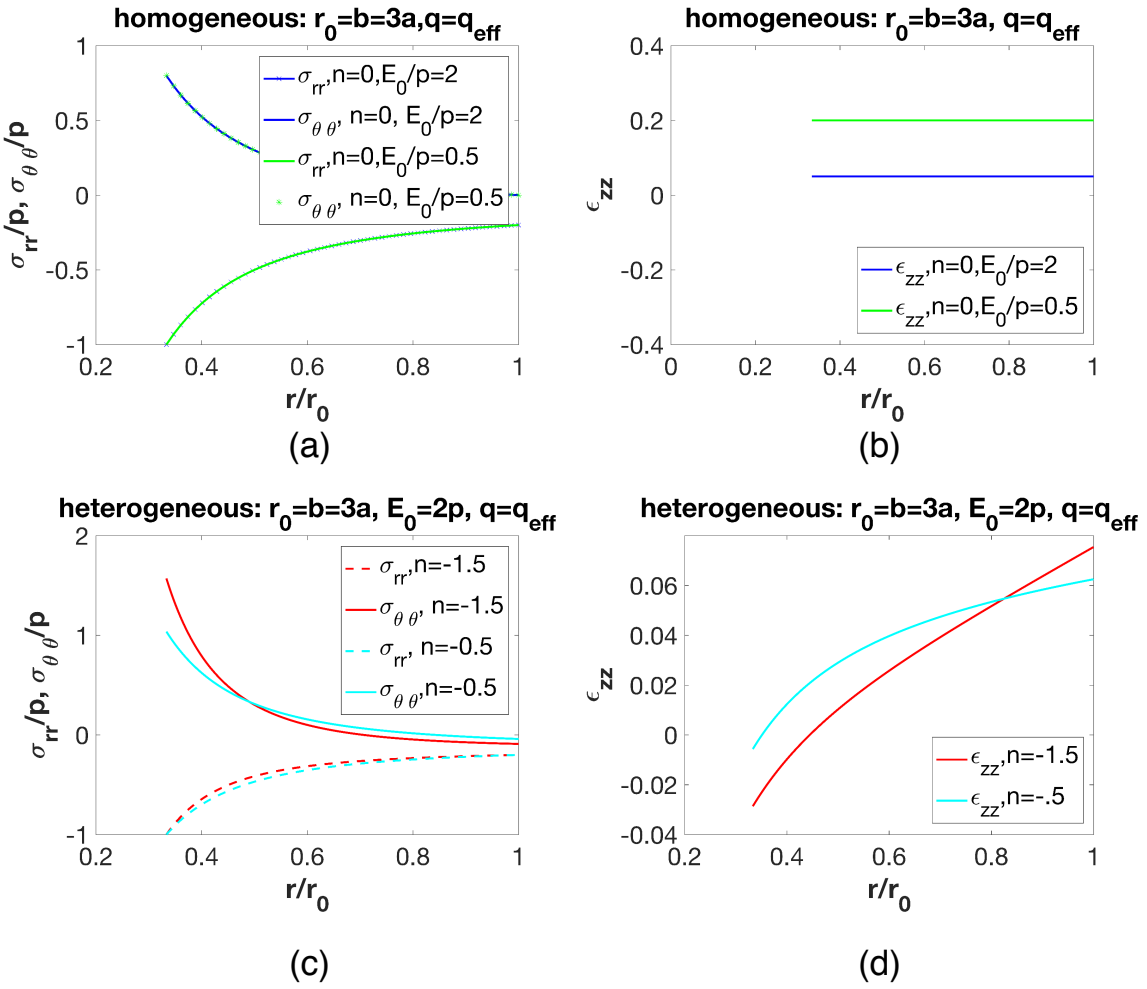

Figure 2.10: Results for a single cylinder with internal pressurization p and external pressurization q ($q = q_{eff} = \phi^A p$) for the case of $\phi^A = 0.2$. The top row (a-b) shows stresses and strains in the homogeneous case ($n = 0$) for two different ratios of E_0/p, while the bottom row (c-d) shows heterogeneous cases. For all cases, a=17.5 microns, b=5a, and Poisson's ratio $\nu = 0.5$. The parameter n was changed to simulate the variation in arteriole wall thickness and stiffness. For a steep heterogeneity, $n = -1.5$, while for a gradual heterogeneity $n = -0.5$.

shown).

Fig.2.10d shows that for a greater heterogeneity ($n = -1.5$, i.e., stiffer arterioles) the positive axial strains develop at a distance farther away from the arteriole wall and are larger in magnitude than the compressive strains near the arteriole wall ($r = a$, or $r/r_0 = .2$ in this case). For the more gradual heterogeneity, larger axial strains occur close to the arteriole wall.

2.3.4 Comparison of analytical and computational approach

The analytical and computational models both demonstrate that a steeper heterogeneity results in injurious strains developing farther from the arteriole wall. Furthermore, the analytical model shows that heterogeneity is required for generating positive axial strains. The material properties and proximity ratios of the analytical solution presented in Fig. 2.10d for $n = -.5$, correspond to similar properties (utilizing the relationship $E = 2\mu(1 + \nu)$) of the simulation shown in Fig. 2.5d ($2a/\lambda = 0.3$). The analytical solution underpredicts the axial strains (0.06 versus .10 maximum strain), although the results qualitatively agree. The discrepancy between the simulation and analytical solution could be attributed to several differences: 1.) the simulation exceeds small strain elasticity, 2.) the finite element model has a discretized boundary between the arteriole wall and surrounding tissue instead of being described by a spa-

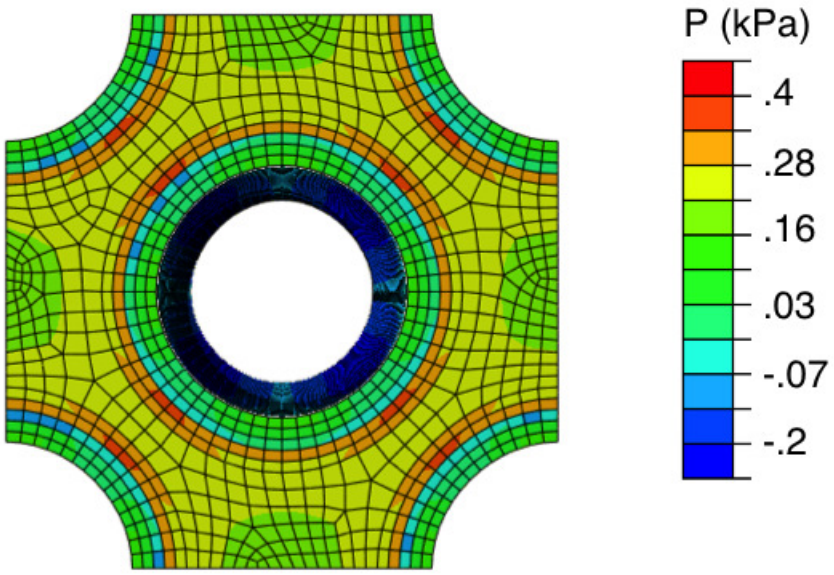

Figure 2.11: FEM simulation (greater heterogeneity, isotropic brain tissue, and proximity ratio of $2a/\lambda = 0.4$) comparing simulated pressure with the effective pressure (q_{eff}) used in the analytical solution. The arteriole spacing in the simulation corresponds to a volume fraction of $\phi^A = 0.2$, and therefore, $q_{eff} = \phi^A p = 0.2$ kPa

tially varying Young's modulus, 3.) the analytical solution approximates the solution for plane stress, and 4.) the analytical solution approximates a uniform q_{eff}.

2.4 Discussion

2.4.1 Implications for injury

The analytical model reiterates an important result seen in the FEM simulations: heterogeneity between the vessels and brain tissue determines the location of damage in surrounding tissue. A gradual heterogeneity will generate larger strains close the arteriole wall, while a steeper heterogeneity causes strains to happen farther from the arteriole wall. Both the analytical and finite element models demonstrate that the largest strains occur halfway between internally pressurized arterioles due to a Poisson effect.

For very close arterioles (i.e, large proximity ratio) undergoing significant deformation, large strains will appear near the arteriole walls regardless of the heterogeneity. This could potentially explain cases when cellular damage is more uniformly distributed between small vessels, as shown in Fig. 2.1c. The work of Goldstein et al. (2012)(Fig. 2.1a-d) and Shively et al. (2017) show damage, in the form of phosphorylated tau, near the walls of small blood vessels from post-mortem chronic traumatic encephalopathy patients.

Regardless of the arteriole wall thickness, all of the simulations showed that a large proximity ratio ($2a/\lambda > 0.3$) resulted in axial strains greater than 10% when subjected to an internal pressure of 2.5 kPa. Although DiPietro et al. (2013) [86] showed that a Lagrangian strain of 10% and strain rate of 20 s^{-1} of rat organotypic slice cul-

tures produced a hypometabolic state and an abnormal pattern of gene modulation, other studies have defined a 14-18% axonal strain (parallel to the axon orientation) to produce an injurious or dysfunctional state [26]. However, it should be noted that thresholds for cellular injury might be smaller at this length scale due to the lesser extent of dissipative mechanisms such as fiber straightening or sliding. Our simulations for the soft isotropic brain tissue (CC) with close spacing ($2a/\lambda = 0.4$) and hypertensive arterioles showed axial strains of 18%, which is well above the threshold set by DiPietro et al. (2013) [86] and equal to the commonly cited average threshold identified by Bain and Meaney (2000) [26]. Strain levels below theses thresholds may still be important since vessel dilation and contraction create increase or decrease synaptic density, respectively, near the vessel walls [111].

Due to the long time scales involved in secondary injury mechanisms, the accumulation of phosphorylated tau over time is affected by several biological mechanisms in addition to the strain fields imparted on the surrounding tissue. The tau protein stabilizes microtubules (MTs) in healthy axons, but undergoes abnormal phosphorylation following injury, eventually leading to accumulation of p-tau which contributes to neurodegeneration [112, 113]. It is believed that during axonal elongation in TBI, MTs (normally aligned in bundles along the axon) will detach from the bundle by breaking the connecting tau proteins [31,32,114]. The sequence of events leading from disassembly of the MT-tau complexes to the accumulation of phosphorylated tau in axons and surrounding glial cells, remains an ongoing research effort [113]. In the

future, more research should be done in modeling tau association/dissociation under damage from macroscale stretching, and obtaining a "p-tau accumulation threshold" for neurodegeneration.

2.4.2 Limitations and future work

Although rat cerebral vasculature posses a similar ultrastructure to human cerebral vasculature [115], their mechanical response may be different. However, since human cerebral arteriole data is not available, and would presumably be much less stiff than the available data on cerebral arteries, we decided to adopt the properties of rat cerebral arterioles. Although we briefly considered the anisotropic behavior of brain tissue in two extreme limits (perfectly aligned versus isotropic), it would be useful to implement realistic fiber orientations between neighboring arterioles in future studies. Previous tissue-level models of brain tissue mechanics define the direction of axons to be the fiber alignment direction, and consider the glial cellular networks to be isotropic; however that may not be true at the smaller length scales examined in this model.

The model does not include the active response of SMCs on the arteriole wall, although this is consistent with recent work which showed that the myogenic response seems dysfunctional following TBI [77]. The lack of SMC contractility might exist following TBI [77], however the consideration of active myogenic responses might be necessary when modeling arteriole inflation in other scenarios. In normal function-

ing arterioles, increased pressurization can depolarize smooth muscle cells to elicit constriction [116], which would presumably reduce the generation of strains in surrounding brain tissue.

For the sake of simplicity, the analytical and computational models presented here ignored several time-dependent factors. Previous studies have shown that the loss of myogenic response begins 24 hours after the initial TBI event [77], although the exact duration of this pathology might vary based on the severity. We have ignored the long term behavior of brain tissue such as bulk interstitial fluid flow, viscoelasticity, and stress-softening following cyclic loading.

2.5 Summary and key findings

We propose a new mechanism for injury to brain tissue during cerebral arteriole inflation and showed that the resulting deformation fields are sufficient to cause injury ($> 10\%$ strains). Although cerebral arteriole heterogeneity might also contribute to nonuniform strain fields during primary traumatic brain injury events (at the time of impact or head acceleration), this study focuses on localized strain in brain tissue following small vessel inflation, a known pathology during secondary brain injury mechanisms. We demonstrate that the relatively high stiffness of arteriole walls, combined with external loading from pressurized neighboring arterioles, creates the possibility of large axial strains occurring halfway between pressurized arterioles, as

shown in the pathology of some TBI cases. In summary, our analysis demonstrates:

1) A "honeycomb pattern" of damage is more likely to occur around normal arterioles (i.e., steep heterogeneity) while a "normal" pattern of perivascular damage is more likely to occur with hypertensive arterioles (i.e, gradual heterogeneity) when surrounded by similar brain tissue.

2) For pressurization in excess of 2.5 kPa, a large proximity ratio ($2a/\lambda > 0.3$) resulted in axial strains greater than 10% across all FEM simulations with isotropic tissue.

3) Regardless of differences in arteriole spacing or brain region, hypertensive arterioles caused larger maximum strain values than normal arterioles.

4) The strain fields presented in this study are consistent with the perivascular cellular damage seen in post-mortem neuropathology of both military personnel and football players with TBI.

Chapter 3

Experimental techniques

In the last chapter, we discussed how understanding the mechanics of arteriole inflation can shed light on cellular damage observed with neuropathological findings from TBI patients. Arteriole spacing, heterogeneity between the arteriole and brain tissue, and anisotropy within the tissue all contribute to strain concentrations in brain tissue. In order to create more realistic models, we need to better understand the mechanical response and heterogeneity of brain tissue at small length scales (i.e., the mesoscale). For example, what is the extent of variation in mechanical properties across the various compartments in glial cells, and can we use this information to approximate the glial cellular network as a mechanically homogeneous material? In this section, we outline a novel experimental platform for probing the mechanical properties of glial cells in a 3D scaffold.

3.1 Introduction

Current techniques to probe the regional mechanical properties of adherent cells (cells–such as glial cells–that grow attached to a surface rather than in suspension) are limited to indentation using Atomic Force Microscopy (AFM), magnetic tweezers, or optical tweezers, on flat two-dimensional (2D) substrates [117, 118]. Biomicrorheology techniques can been used to probe the mechanical properties of cells in 3D substrates [119, 120], however, this technique can only probe internal properties at the local nano-/microenvironment. Since 2D substrates are not representative of the cellular microenvironment found in tissues [121, 122], adherent cells often express unrealistic morphologies and phenotypes when grown on flat substrates [15]. Given the same stiffness substrate, different cell morphology can result in different cell stiffnesses [123]. We demonstrate, for the first time, an experimental setup that allows probing the bulk mechanical properties of local compartments of adherent cells (in this case, glial cells) grown in a three-dimensional scaffold. Using optical trapping, we can perform indentation testing on cells at precise locations, and then use the nonlinear contact mechanics formulations developed in Chapter 4, to obtain the local hyperelastic mechanical properties while the cells exist in a more favorable three-dimensional microenvironment.

With 3D culture systems, cell surface receptors can become spatially organized in a more biologically relevant configuration, allowing cells to undergo the mechanical cues and cell-cell communication which can be lost with cultures grown on flat plastic

and glass substrates [124], [125]. Differences in cell morphology and phenotype in 3D cultures have been shown across various cell types such as chondrocytes [126], hepatocyes [127], [128], epithelial cells [129], and astrocytes [130, 131].

Conventional techniques in the mechanical testing of cells, such as atomic force microscopy (AFM) or scanning force microscopy (SFM), require cells grown on a flat substrate so that the cell surface can be vertically indented with an AFM probe tip of a selected geometry. The applied vertical force is measured from the bending of the AFM cantilever, which has a pre-determined stiffness. For a given indenter tip shape, the measured forces and indentation data can provide measurements of the specimen material properties. The length scale at which the specimen is probed depends on the indenter tip shape and overall dimensions.

Previous efforts to probe the mechanical properties of cells in a more native environment have used computational modeling to estimate the elastic properties of heterogeneous samples containing cells embedded in a three-dimensional extracellular matrix (ECM) [132, 133] by measuring an overall "apparent stiffness." Since the Young's modulus of the ECM gel is known, a computational model is used to decouple the Young's modulus of the cell from the overall apparent stiffness, with the assumption that the ECM is an isotropic and homogeneous matrix surrounding a perfectly spherical cell. Although this technique enables the measurement of cell properties in a 3D culture, it cannot be applied to local cell compartments or non-spherical cells grown in porous scaffolds.

Another technique in which the mechanical properties of cells can be probed in a 3D scaffold environment is through intracellular particle-tracking microrheology–a technique in which spherical particles are internalized by the cell and the movement of the particles is tracked over time [134]. The "active" motion (through externally applied forces on the particle) or "passive" motion (from thermal effects) of the particle is monitored and related to the nonbulk viscoelastic properties by comparison with the known theoretical Brownian motion of a submicron particle entangled in a filamentous protein network [119, 135]. Previous studies have utilized microrheology to obtain mechanical properties of cells grown in a 3D scaffold [120, 136], however, these measurements do not incorporate effects of plasma membrane tension, as an indentation test does [119].

Since the measured mechanical response of cells depends on the underlying cytoskeleton, it is desirable to obtain mechanical properties with respect to specific cell compartments [47]. In neurons and glial cells, previous work demonstrates that soma, neurites, and processes, each exhibit different mechanical properties [48], [1] (Fig. 1.4). In addition to AFM, bead-based techniques such as optical tweezers (OTs), magnetic twisting cytometry (MTC), and particle-tracking microrheology (PTM), have the capability of obtaining mechanical property measurements of local cellular compartments. Here we present a new technique using an optically trapped silica bead to perform indentation testing on cells grown in an electrospun scaffold. Optical trapping allows the three-dimensional measurement of small forces (on the order

of tens of piconewtons), and precise positioning of a bead, to obtain the mechanical response of specific cellular compartments within a scaffold. Although it is common to use an optically trapped silica bead as a "handle" to apply tensile forces to cells and surface-tethered molecules, it is also possible to use the bead as a spherical indenter tip [137–139].

3.2 Fundamentals of optical trapping

Optical traps, also referred to as optical tweezers, were invented by Arthur Ashkin in 1986 [140]. With this instrument, a highly focused laser beam is used to precisely position microscopic dielectric objects and measure small forces (on the order of 1-100 pN). Objects ranging in size from 20 nm to several microns [59] can be physically levitated (or "trapped") in three-dimensions, as long as the object is able to transmit light.

A ray optics schematic illustrating the principles of optical trapping through conservation of the photon momentum is shown in Fig. 3.1A. When an object (such as the sphere in Fig. 3.1A) is outside of the trap focus, the net momentum change from photons can draw the object towards the center of the trap gradient. The change of momentum from individual rays of light (e.g., the vectorial difference between A_i and A_t) when striking the object results in an equal, opposite momentum change on the particle. This is known as the gradient force (F_g) since it relies on an intensity

gradient (usually in the form of a Gaussian beam profile). The gradient force must be strong enough to counteract the scattering force (F_s) produced by the photons striking the object along their propagation direction.

The mechanism of optical trapping can only be explained using the ray optics approach when the particle size is larger than the wavelength of the incident light, also known as the Mie Regime. When the particle size is substantially smaller than the wavelength, also referred to as the Rayleigh regime, a different theoretical approach using electromagnetic field vectors must be used. For a more detailed explanation of optical trapping in the Rayleigh regime, the reader is referred to Harada and Asakura (1996) [141]. For particle sizes that are comparable with the wavelength of the trapping laser, the physics of neither the Mie or Rayleigh regime are completely accurate [142].

For a dielectric object trapped by the gradient force, any displacement of the object from center of the trap focus will result in a restoring force towards the trap focus. A depiction of the optical trap restoring force is shown in Fig. 3.2. In order to use an OT to measure forces precisely, one must measure the "stiffness" of the optical trap. In other words, one must calibrate how much force is required to move a given object by a given distance from the center of the intensity gradient. The force from the OT in the i-th direction (denoted as F_i) acts as a "restoring force" and can be deduced by:

$$F_i = k_i \Delta d_i \tag{3.1}$$

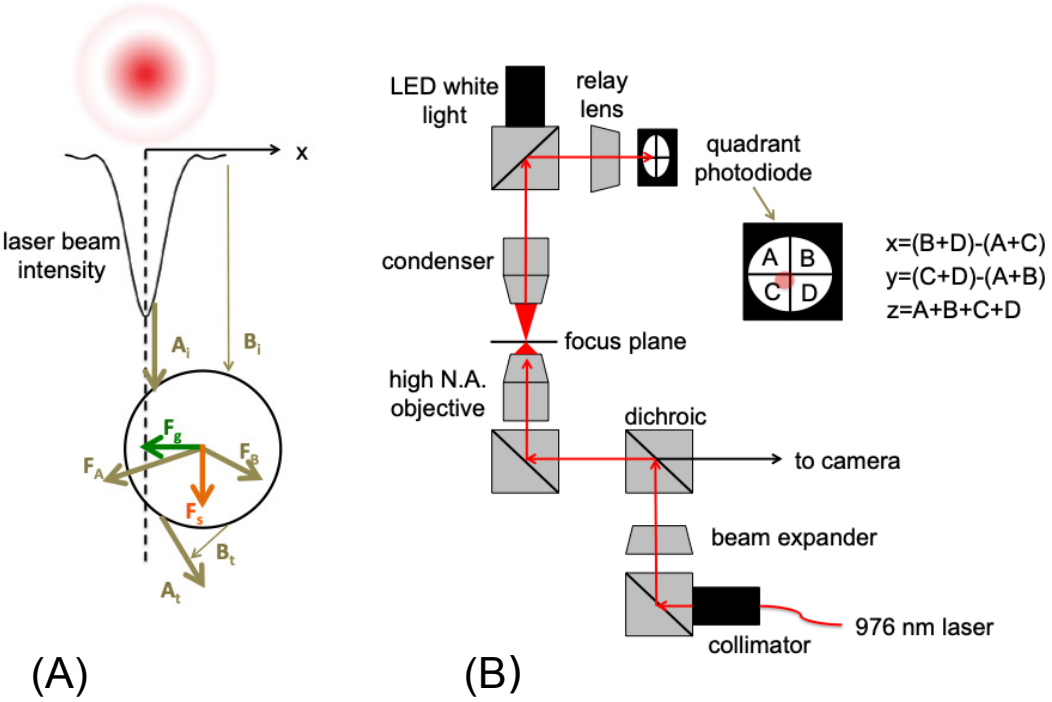

Figure 3.1: (A) Schematic behind the principles of optical trapping on a spherical particle in the case of a particle size that is much greater than the wavelength of incident light. A_i and B_i are incident light rays, while A_t and B_t are the transmitted rays. The particle will experience a momentum that is equal to the momentum change but in the opposite direction, resulting in F_A and F_B on the particle. In order to maintain a stable trap, the net gradient force acting on the trap (F_g) must balance the net forces from scattering (F_s) in the the (forward) direction of light propagation. (B)Schematic of optical trap instrumentation. A laser beam is collimated and expanded in order to flood the back aperature of an objective with a high numerical aperture. After being focused into a small waist beam above the objective, the beam is transmitted to a quadrant photodiode (QPD) sensor which measures any deflections of the beam by looking at changes in voltages between the quadrants. Although other bead detection methods exist, the QPD sensor allows for high temporal and spatial resolution of bead deflection.

where k_i is the trap stiffness in the i^{th} direction, and Δd_i is the bead deflection in the i^{th} direction (shown as Δd_x, Δd_y, and Δd_z in Fig. 3.2). The stiffness of the OT will be slightly different in each direction, with the axial direction (z-direction) typically having the lowest stiffness since this is the primary direction of scattering forces. Additionally, different sized particles and different laser power will create different values of k_i since these parameters alter the gradient and scattering forces, respectively. Therefore, it is important to calibrate the stiffness of the trap using the same bead size and power that will be used in the experiment.

3.3 Experimental setup

3.3.1 Overview

A schematic of the optical trap setup used in our experiment is shown in Fig. 3.1B. When building a successful optical trap (OT), a laser beam is aligned into the back of a microscope objective and is focused to a diffraction-limited beam waist (shown in the focus plane of Fig. 3.1B). An objective with a high numerical aperture is required to allow for a maximum amount of light going into the objective, thereby creating the largest possible intensity gradient. As water is a major component in biological tissue, and has low absorption in the infrared range of light (λ=700 nm-1μm), utilizing a laser source within the infrared region helps minimize damage to cells [59]. However, even at infrared wavelengths, laser adsorption by the specimen

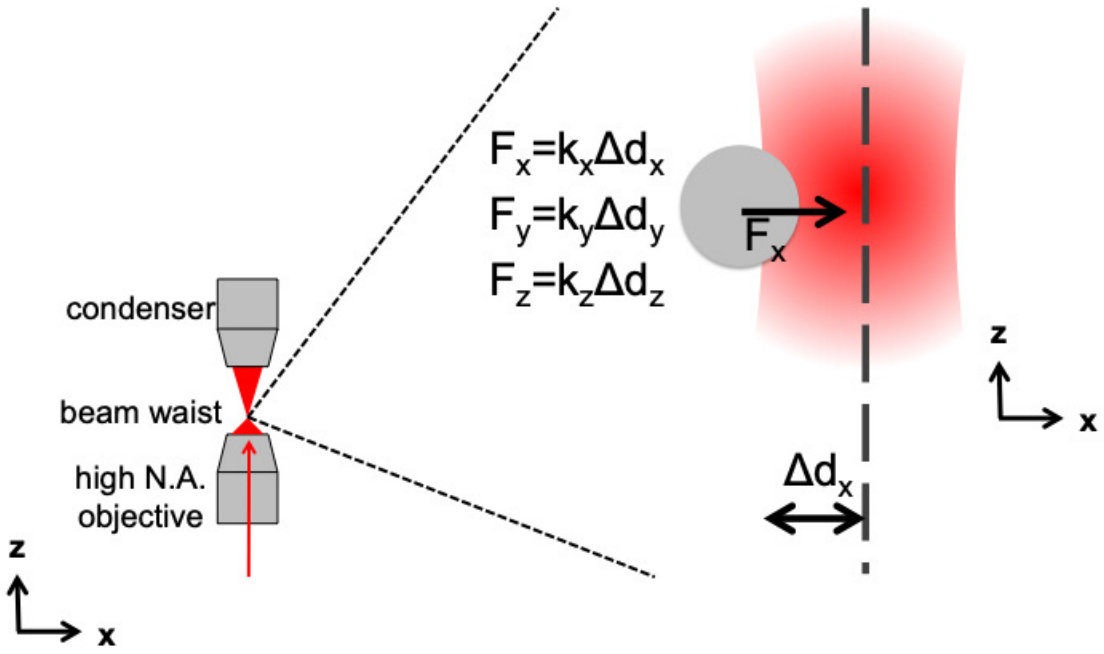

Figure 3.2: Schematic of the OT restoring force. Imagine that a "spring" with stiffness k_i attaches the a spherical bead to the center of the optical trap, and that the force needed to pull the bead from the trap increases with the distance d_x. Although this example shows the bead being translated from the OT center in the x-direction only, any arbitrary displacement vector will have forces in the X-, Y-, and Z-directions to move the bead back to its stable position in the center of the trap

can still result in some photodamage from thermal effects [143, 144].

3.3.2 OT details

A 975 nm laser operating at 200 mW at the back aperture of a Nikon 100X oil immersion objective (NA=1.25) was used to optically trap 5-micron diameter streptavidin-coated silica beads (Bangs Laboratories, Fishers, IN). Back focal plane detection of the transmitted laser light was obtained with a quadrant position detector (Thorlabs, # PDQ80A) in order to provide three-dimensional displacement information on the bead, as depicted in Fig. 3.1B.

Silica beads (which act as the indenter tip) were optically trapped in the vicinity of a cell of interest and gently pressed against the cell surface for 3-5 minutes to ensure a sufficient bond between the streptavidin-coated bead and the biotinylated cell surface. The determination of the initial contact point is non-trivial for indentation into soft materials, and if identified incorrectly, can create an inaccurate force-displacement relationship during indentation testing [145]. To ensure that our initial contact point is known, we utilized streptavidin-coated silica beads to adhere to the biotinylated cell membrane surfaces. The biotin itself is incorporated into the glycocalyx layer (or "cellular brush") surrounding the cell membrane. In reality, the first 10-50 nm of the indentation is probing the cellular brush, which can be accounted for using a "brush model" during indentation analysis [57, 146]. For the cells in this study, the thickness of the cellular brush is negligible, and is within the the error in tracking the

positional data of the bead (which was found to be approximately 20 nm and 30 nm in the x- and y- directions, respectively).

The z-depth (along the laser propagation, above and below the bead) was visually examined by focusing the objective throughout the scaffold thickness to ensure that the optical path was unobstructed for the transmitted laser light.

3.3.3 Trap calibration

An overview of possible OT stiffness calibration techniques is provided in the Appendix B.2.2. Out of the available techniques, we used the power spectral density (PSD) roll-off technique, which is the most commonly used technique since it does not require prior position calibration of the QPD sensor [147]. The PSD method relates the observed frequencies of particle motion in the trap to the theoretical frequencies of a damped massless oscillator in a fluid of known viscosity. The trap stiffnesses in the x-, y-, and z-directions were found to be $k_x = 34.9$ pN/μm, $k_y = 34.2$ pN/μm, and $k_z = 24.1$pN/μm. Additionally, the PSD method is useful for detecting sources of noise in the system. Note that this method does not readily provide information on the maximum holding force of the trap (the maximum force that the trap can provide before the bead can be pulled out of the trap). In order to calculate the maximum allowable deflection (and thus maximum holding force), the Stokes flow technique can be used (see Appendix B.3.1). With the Stokes flow technique, the fluid velocity surrounding the bead is increased until the measured drag force is large

enough to remove the bead from the trap. For the 5 μm diameter silica beads used in the experiments, the maximum holding force magnitude of the trap was 22.1 pN, and the maximum allowable deflection was found to be .61 μm.

3.3.4 Preparation of experimental samples

3D cellular scaffolds were produced by electrospinning polyvinylidene fluoride (PVDF) directly onto glass coverslips (22 mm x 22 mm). Glial cells from mouse pups were grown for 7-10 days on electrospun polyvinylidene fluoride (PVDF) scaffolds (for more details see Sec. 3.6). Before indentation testing, cells were stained with calcein to verify cell viability.

Glial cells grew processes along the PVDF fibers. Fig. 3.3 demonstrates that glial cells exhibited a more stellate-like appearance when grown on electrospun polymer scaffolds in comparison to the polygonal morphologies seen on glass substrates.

Prior to mechanical testing, scaffolds were carefully removed with tweezers from the 6-well culture plates. A small 15 μl drop of diluted streptavidin-coated silica beads was placed on a fresh coverslip (22 mm x 40 mm), and the cell-laden scaffolds were placed upside down onto the drop of silica beads (Fig. 3.4A). This was performed because the coverslips exposed to cell culture media could contaminate the surface of the objective and cause misalignment in the optical trap beam. The assembled coverslips were then backed by a 1 mm thick microscope slide to prevent bending due to contact with the 100X oil-immersion objective. Within 5-10 minutes, the majority

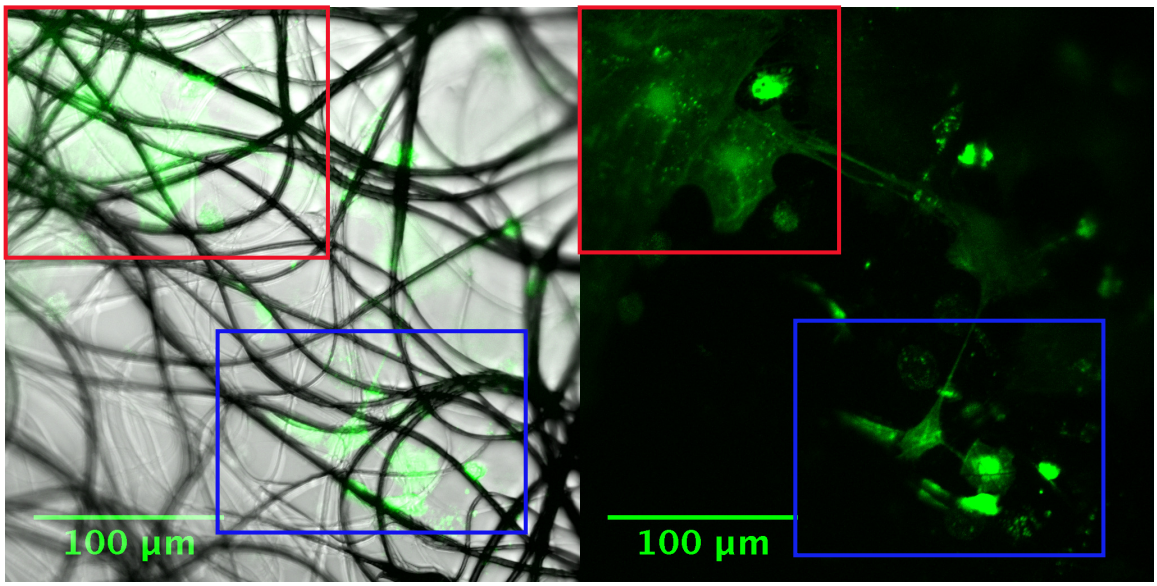

Figure 3.3: Comparison of cells growing on the cover slip glass underneath of the scaffold fibers (red box) and cells grown within the polymer scaffold (blue box). Left panel shows light confocal microscopy image overlaid with fluorescence stain of calcein (green) while the right image shows only the fluorescence image for clarity. Note that the cells which migrated to the glass substrate developed a large polygonal morphology, while cells in the scaffold contained processes which grew along the fibers.

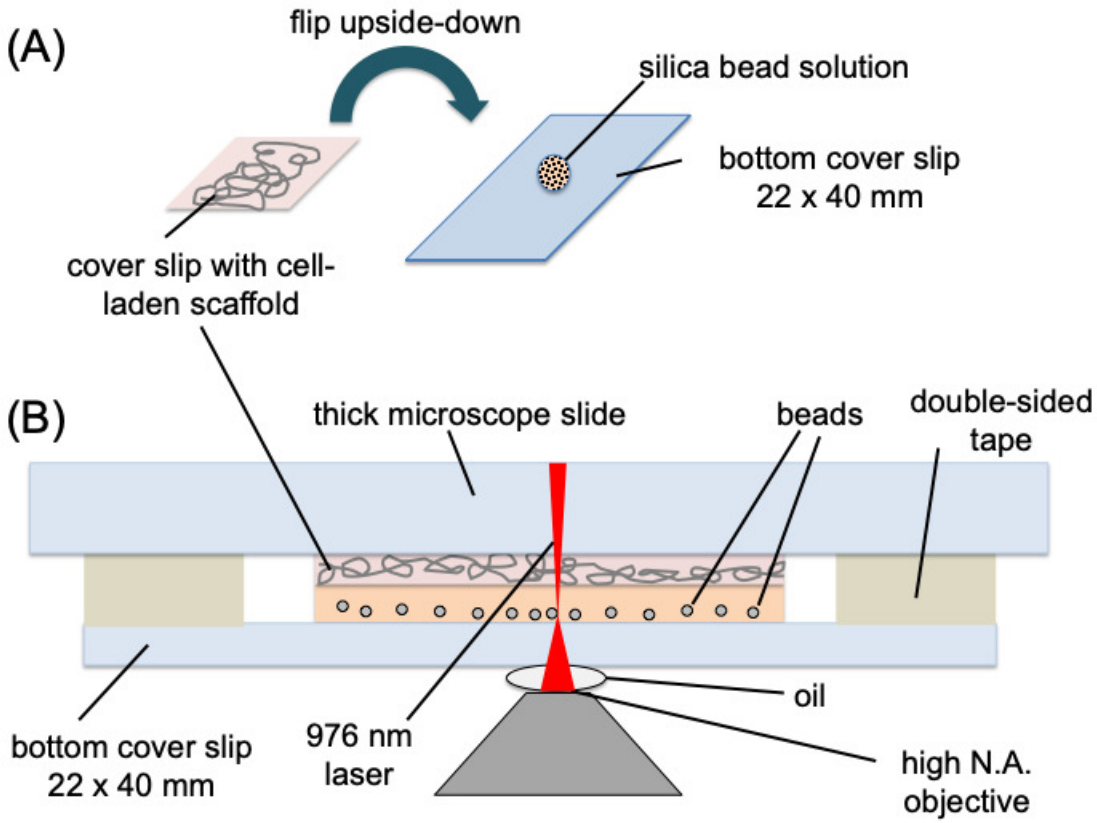

Figure 3.4: Schematic of specimen and loading configuration for OT experiments. (A) A cover slip with the PVDF scaffold containing cells is flipped upside-down into direct contact with a droplet of diluted silica beads on a clean cover slip. (B) Schematic showing scaffold sandwiched between two cover slips. A thick microscope slide is used as a rigid support as the objective is brought into contact with the bottom cover slip. A specimen holder presses the microscope slide and cover slips together (not shown) and applies a reaction force to the objective which moves upward into the bottom cover slip. The specimen holder couples the specimen with the translation stage.

of silica beads fall to the bottom surface of the coverslip, where they can be trapped and subsequently brought into contact with a nearby cell for indentation testing, as shown in Fig. 3.4B. An additional schematic outlining the entire experimental process along with the assigned coordinate system is shown in Fig. 3.5.

3.3.5 Force-indentation acquisition

A 3-axis high precision piezo actuator specimen stage (Nanomax stage, Thorlabs #MAX311D) in closed-loop mode with internal strain gauges for positional feedback (Thorlabs, #KSG101) was translated in the direction perpendicular to the long axis of the cell process (and its supporting PVDF fiber). Thus, the relatively rigid scaffold with the embedded cells is displaced by a known distance towards the direction of the trapped bead in the x- and y-directions (Fig. 3.5B-C). The distance of stage translation, which is provided by the stage controller (through feedback from an internal strain gauge), is denoted as $\Delta\psi$, where $\Delta\psi_i = \Delta\psi_x$ or $\Delta\psi_y$, since the stage is translated in either the x- or y-directions, depending on the cell process orientation.

Upon the applied collision of the cell into the bead, the resulting deflections of the bead measured by the QPD (denoted as Δd_i) enable the determination of the applied force (Fig. 3.5E). In other words, the restoring force associated with the bead deflection is a consequence of the bead getting pushed by the prescribed specimen displacement. The indentation depth (or displacement, δ) from the cell surface is then simply:

$$\delta_i = \Delta\psi_i - \Delta d_i \tag{3.2}$$

Here, the usage of Δd_i refers to a displacement from the optical trap center in the i^{th} direction (the direction of stage translation). Therefore, Δd_i is equivalent to Δd_x, Δd_y, and Δd_z in Fig. 3.2. The force applied to the cell is therefore determined from the bead deflection by: $F_i = k_i \Delta d_i$, where k_i is the known calibrated stiffness of the optical trap calibrated in the i^{th} direction. Due to the high stiffness of the scaffold fibers, we can assume that the fiber remains rigid during the indentation testing (shown explicitly in Section 3.4.3).

Position data of the trapped bead, as well as the stage translation data in the x- and y- directions, were recorded as voltage histories with a National Instruments Data Acquisition system (#USB-6212 BNC) and a custom-built Labview program. A sampling rate of 36 kHz with the data acquisition system was sufficient to capture bead deflection during the movement of the specimen stage over roughly 50 ms. Examples of the stage controller and QPD voltage output histories are shown in Fig. 3.6A,B, respectively. Fig. 3.6A shows the stage controller voltage output, which corresponds to an applied "jump" in stage displacement to about 500 nm. The resulting bead deflection at the cell surface is shown in voltage history of Fig. 3.6B. For all tests, the stage displacement should be slightly less than the maximum allowable trap deflection with a 5 μm bead, which was calibrated to be 610 nm to ensure that the bead is not removed out of the trap during the experiment. The

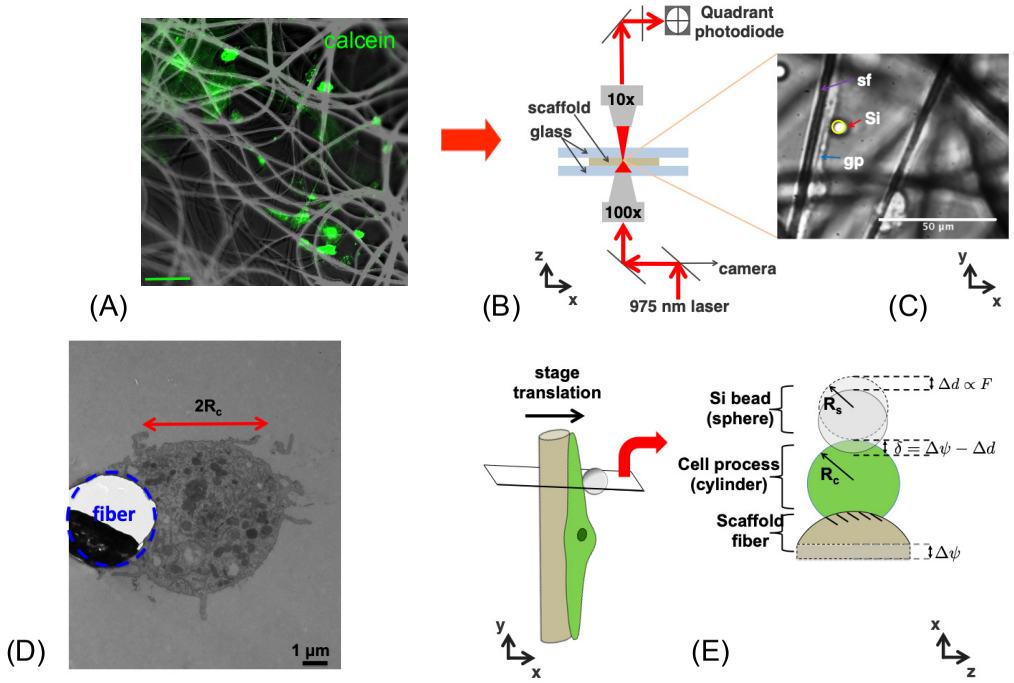

Figure 3.5: Schematic for optical trap indentation setup. (A) Cells are grown for 7-10 days in an electrospun PVDF scaffold in order to grow cellular processes. Cells are stained in calcein to verify viability during mechanical testing. Scale bar =50μm (B) Scaffolds with cells are inverted onto coverslips with 10 μL of Silica beads diluted in deionized water. Specimens are clamped into a translational piezoelectric stage at the focal point of the trapping laser. A quadrant photodiode at the back-focal plane is used to detect deflection of the 975 nm laser, thereby providing X,Y, and Z changes of bead displacement. (C) Example image of glial process (gp) grown along a scaffold fiber (sf). An optically trapped streptavidin-coated silica bead (Si) is brought into contact with the biotinylated surface of the cell. (D) Transmission electron microscopy shows the cross-sectional view of the scaffold fiber outline (blue circle) and glial cellular process (diameter of $2R_c$). (E) The specimen stage is translated in the direction perpendicular to the fiber (+X-direction in the example shown). The cross-sectional view depicts the scaffold translation (Δz), measured bead deflection (Δd), and cell indentation ($\delta = \Delta z - \Delta d$). The bead deflection ($\Delta d$) is related to force through prior calibration of the OT.

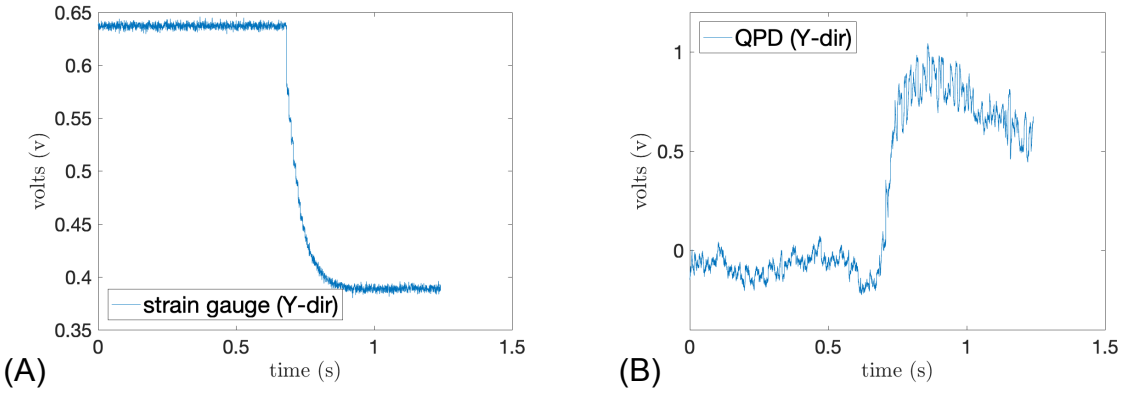

Figure 3.6: Examples of voltage histories from (A) the stage controller (obtained from internal strain gauge readings) and (B) the quadrant position detector (QPD). In this case, the specimen stage was moved in the y-direction. Voltage readings from the stage controller correspond to the measured $\Delta\psi_y$, while voltages from the QPD correspond to Δd_y (and therefore, the indentation force F_y).

maximum allowable trap deflection is determined by the laser power at the back aperture of the objective, as well as the size of the silica bead.

3.4 Assumptions and quantification of uncertainty

3.4.1 Uncertainty in bead position

From the example voltage history signal from the QPD output (Fig. 3.6B), the position data of the bead (Δd) shows a signal containing some fluctuations from the baseline position, even before the stage begins to move (shortly after 0.5 seconds). The additional noise in bead position measurement is partially attributable to:

- The inherent "damped oscillator" behavior
- Small nearby molecules getting drawn into the optical trap and colliding onto the bead surface
- Fluctuations at the surface of the membrane due to Brownian motion of biological processes

By calculating the average fluctuation in the QPD signal for the bead positioned on the cell surface before stage movement (when δ is presumably zero), an average uncertainty error in bead displacement for each experiment is determined. Although Fig. 3.6B shows the raw data, in later analysis of the force-displacement curves presented in Chapter 5, a moving average differentiation was performed for every 2.5 ms on the QPD signal. The standard deviation from the mean value of bead position during the 2.5 ms interval before stage translation provided an appropriate average value for the uncertainty in bead position. The uncertainty in bead position measurement due to noise in the example data from Fig. 3.6B corresponded to ± 0.018 μm in the x-direction, ± 0.032 μm in the y-direction, and ± 0.005 μm in the z-direction. Across all experiments, the average uncertainty in bead position due to noise along the direction of loading was approximately ± 0.038 μm. Since the error of the prescribed stage displacement was $5-10$ nm [1] due to the minimum voltage change output by the stage controller, we consider the noise in bead position measurement

[1] Theoretical resolution provided in specifications for Thorlabs NanoMax stage MAX311D: www.thorlabs.com/NewGroupPage9.cfm?ObjectGroup_ID=2386

to be the primary contributor of uncertainty in our force-displacement curves.

3.4.2 Quantifying compliance of the piezoelectric stage

The extent of cell deformation is calculated using the measured bead deflection and stage translation (Eqn. 3.2). Thus it was necessary to ensure that the measured applied stage translation was sufficiently equivalent to the actual scaffold movement. Image analysis was used to compare to stage controller voltage histories to the stage movement observed in microscopy images taken with a Nikon 100X oil immersion objective (NA=1.25) and CMOS camera (Thorlabsm Item #DCC1240C). Figures 3.7A-B show the microscope images of fibers before and after translation in the x-direction, while Figures 3.7E-F show the microscope images of fibers before and after translation in the y-direction. By reading the grayscale intensity values, the distance change in pixels between the peak intensity values can be used to determine the position change of the fiber along the x- or y-directions. Differences between the image analysis and stage displacement measurements were < 5 nm, well within the accuracy of the image analysis itself (25 nm between pixels along the intensity peaks). In other words, the accuracy to which we can verify the stage movement (25 nm) is comparable to the error in bead position uncertainty (18 to 32 nm).

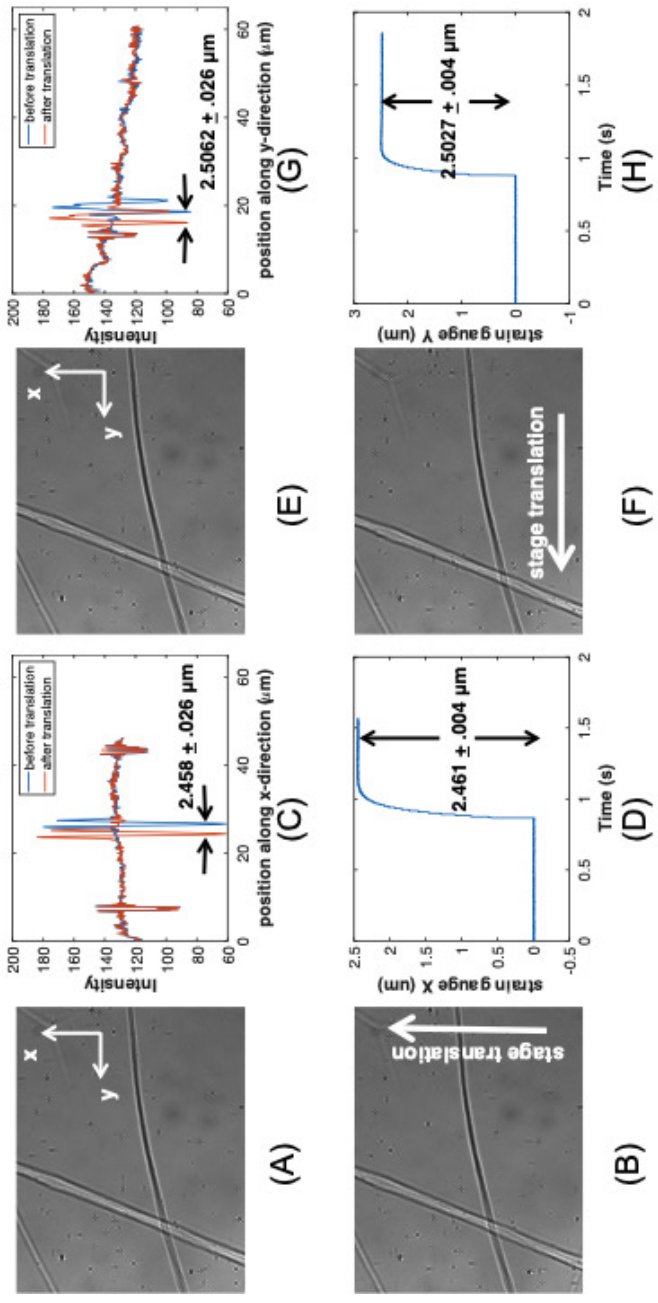

Figure 3.7: Microscopy images of scaffold fibers before (A) and after (B) stage translation in the x-direction. Grayscale images were read into Matlab and the intensity values were plotted for a line sweeping the x-direction (C). From the peak intensity values, we could obtain the translation distance of the fiber, and compare the distance to the measured stage displacement reading (D). Microscopy images were taken before (E) and after (F) stage translation in the y-direction. Intensity peaks from the grayscale images were used to calculate the fiber translation (G) and compared to the measured stage displacement reading in the y-direction (H). Results showed that the fibrous scaffold translation was equivalent to the measured stage displacement readings to within 26 nm (the minimum distance distinguishing between pixels in the intensity plots).

3.4.3 Assumption of fiber rigidity

Since our indentation formulation in Chapter 4 assumes that the fiber is a rigid substrate beneath the glial cell process, we performed a quick calculation to ensure that the selected polymer fibers were sufficiently stiff. To check if it is possible for the fiber to bend from the small indentation forces of a trapped silica bead, we can consider an Euler Bernoulli beam of length L, simply supported at both ends, and under a point load at $L/2$. It is assumed that the "ends" of a single fiber are simply supported by nearby fibers that cross perpendicularly. The central deflection (δ_{max}) would then be:

$$\delta_{max} = \frac{FL^3}{48EI} \tag{3.3}$$

Where F is the applied load at $L/2$, E is the Young's modulus of the polymer fiber, and I is the moment of inertia. In this case of a beam with a circular cross section, $I = \frac{\pi d^4}{64}$. The diameter of a single PVDF fiber is approximately 1 μm, and the stiffness can be approximated as $E = 2.2$ GPa [148]. The maximum applied force of $F = 22$ pN, is the maximum force allowable by the optical trap. Since it is undesirable to have scaffold fiber deflections greater than $\delta_{max} = 38$ nm (the mean experimental uncertainty in bead displacement due to noise), then it is possible to calculate the minimum required length of the fiber that can undergo central deflections larger than 38 nm using the aforementioned values of F,E, and I. The approximation for fiber length resulted in a spacing of $L >$200 μm, which far exceeds the spacing between fibers in our scaffold. In other words, the PVDF fiber is stiff enough, and closely

packed enough, such that the maximum force of the optically trapped bead will not cause significant deflections (> 38 nm) in the fiber.

3.5 Alignment effects

The cell is translated and aligned in the x-y plane since this is the imaging plane observable by the camera. Precise alignment of the bead in the z-direction (along the laser light propagation) was not possible by visual inspection in the OT setup presented here. In the following section, we present a computational model we use to quantify the extent to which misalignment of the bead in the z-direction would affect the force-displacement curves for different combinations of indenter and specimen sizes. Fig. 3.8 shows an overview of the effects of misalignment found with the computational model. To help mitigate misalignment errors, it is possible to measure the displacement components of the bead in the x-, y-, and z- directions, and relate this to the "misalignment offset" (referred to as β in Fig. 3.8A) in the z-direction. Measurements of the tangential force (designated as F_z in the coordinate system shown in Fig. Fig.3.8B) are proportional to an increase in offset, β.

3.5.1 Modeling misalignment effects

We use a computational model to estimate the errors due to increasing misalignment offset (β in Fig. 3.8A) in order to obtain error bounds for the experimental

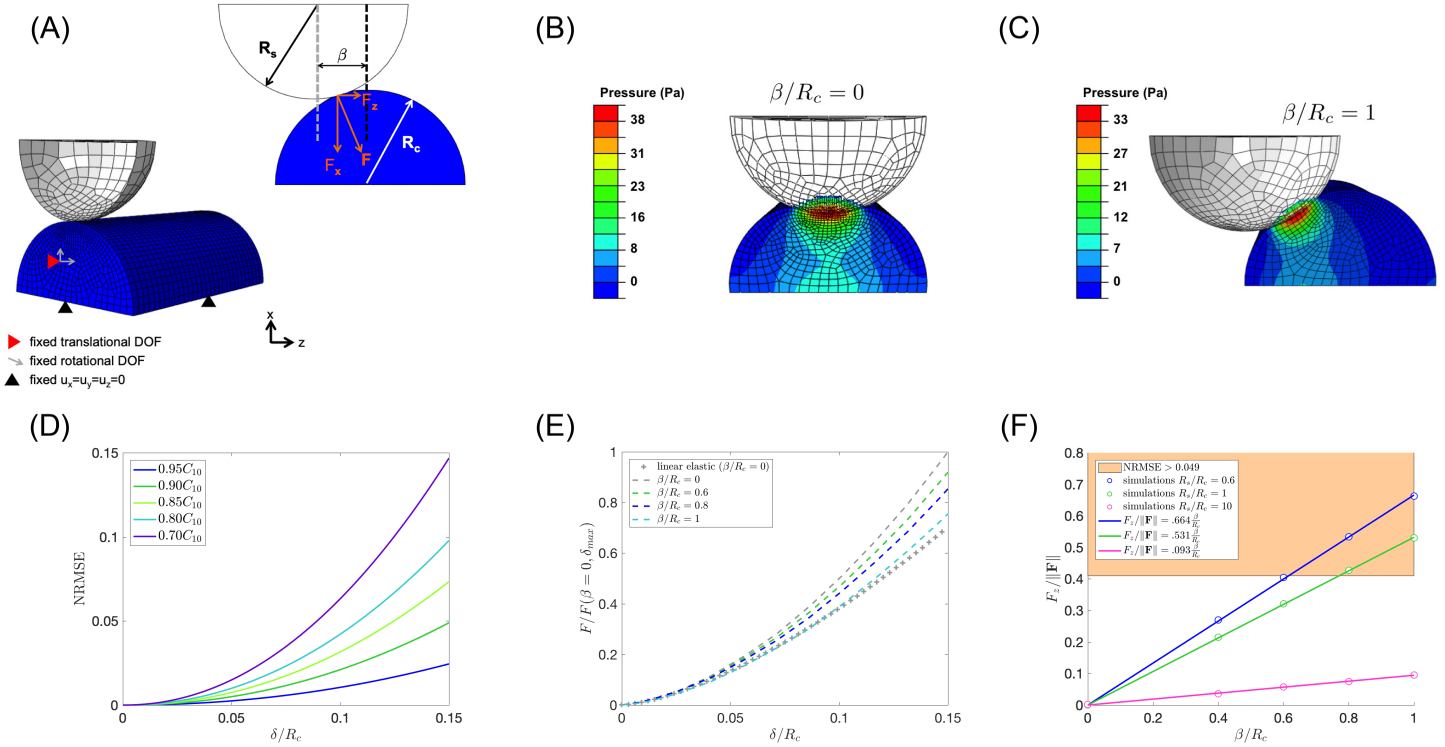

Figure 3.8: Effects of indentation misalignment. (A) Schematic of the finite element model dimensions and boundary conditions. (R_s is the radius of the spherical indenter, R_c is the radius of the cellular process, and β is the perpendicular distance which quantifies the offset of the indenter from the centerline of the specimen. (B) Finite element simulation of resulting pressure distribution when $\beta = 0$. (C) Pressure distribution when $\beta/R_c = 1$ shows a decrease in peak pressure at the point of contact. (D) Plot of normalized root-mean-square error (NRMSE) of the force obtained by varying the value of C_{10} in a simplified Mooney Rivlin material ($C_{01} = 0$) under indentation. X-axis is a non-dimensional measure of indent depth. An NRMSE value greater than .049 is associated with ¿10% error in the material stiffness. (E) Normalized force versus non-dimensional displacement for various amounts of offset in the case of $R_s/R_c = 1$. (F) Computational models provide a measure of tangential force (F_z) to force magnitude for various amounts of offset for different values of R_s/R_c. The shaded area of the plot encompasses the region where the $NRMSE > 0.049$. A threshold of $F_z/||\mathbf{F}|| = .41$ results in an experiment being deemed unreliable for obtaining material properties.

data. Transmission electron microscopy showed approximately circular cross-sections for the cells (example shown in Fig. 3.5D), which justified modeling the experiment as a rigid sphere in contact with a soft cylindrical cell. Let R_s refer to the radius of the spherical indenter, while R_c refers to the cylindrical radius of the cell. Since errors due to β would likely be dependent on the ratio of R_s/R_c, simulations were performed to encompass the values of R_s/R_c (in the range of 0.6 to 10) observed in the experiments.

Finite element simulations were performed with the commercial package Abaqus (Dassault Systemes) to obtain the force-displacement relationships for each combination of R_s/R_c and β. A rigid spherical indenter was prescribed a normal displacement of 0.75 μm into a hyperelastic cylindrical specimen using a frictionless contact. For each value of R_s/R_c, individual simulations were performed with varying amounts of β ($\beta/R_c = 0, 0.4, 0.6, 0.8, 1$).

A mesh convergence study was initially performed to obtain the minimum necessary element size at the contact interface. Several simulations were performed with the smallest element size at the center of contact varying between 2.5×10^{-5} mm and 5×10^{-4} mm. It was observed that all simulations (including the coarsest mesh) were able to accurately capture the theoretical force-displacement curves for a linear elastic material at small strains, although, a minimum element size of 1×10^{-4} mm was necessary for the convergence of the total internal energy.

In order to reduce computational costs, a symmetric plane was enforced transverse

to the cylinder length. Effects from the free boundary end were avoided by making the total length of the cylindrical specimen in the model at least twice the length of the major axis of the elliptical contact area. The bottom face of the model was given a fixed displacement boundary condition ($u_x = u_y = u_z = 0$). In reality, a smaller surface area would adhere to the PVDF fiber, as shown in the TEM image of Fig. 3.5D, allowing for more expansion in the out-of-plane directions. Here we are exclusively interested in the *relative* effect of misalignment, and therefore not largely concerned with replicating the wide range of possible cell adhesion boundary conditions.

Since biological materials often undergo large deformations ($\delta/R_c > 0.05$) and demonstrate a strain stiffening behavior [149, 150], it is desirable to obtain material parameters that can describe the cell as a hyperelastic material. A commonly used hyperelastic model for soft materials is the Mooney Rivlin model, described by the strain energy density function:

$$W = C_{10}(\bar{I}_1 - 3) + C_{01}(\bar{I}_2 - 3) + \frac{K}{2}(J_{el} - 1)^2 \tag{3.4}$$

Where $\bar{I}_1$ and $\bar{I}_2$ are the modified first and second invariants of $\bar{\mathbf{C}}$ (the distortional part of the right Cauchy-Green tensor), K is the bulk modulus, and J_{el} is the elastic volumetric strain. C_{10} and C_{01} are material constants. For the case of small deformation, C_{10} and C_{01} are related to the elastic modulus by $E = 4(1+\nu)(C_{10}+C_{01})$. Since we are only interested in using the model to quantify the effects of misalignment, $C01$ was set equal to zero, so that Equation 3.4 reduces to a simpler neo-Hookean strain

energy density function. However, the full Mooney Rivlin model will be used later in Chapters 4 and 5 when obtaining the mechanical properties from the experimental data.

As shown in the pressure distribution contour plots of Fig. 3.8B-C, as one increases the misalignment offset, the cell experiences smaller stresses than the perfectly aligned case ($\beta = 0$). This is due to the smaller area of contact associated with larger β values. In order to quantify differences between misaligned indentation force ($F(\beta)$) versus normal ($F(\beta = 0)$) indentation, we calculated the normalized root-mean-square error (NRMSE), which is defined as:

$$\text{NRMSE} = \frac{RMSE}{F(\beta = 0, \delta_{max})} \tag{3.5}$$

where

$$\text{RMSE} = \sqrt{\frac{\Sigma_{t=1}^{T}(F(\beta)_t - F(\beta = 0)_t)^2}{T}} \tag{3.6}$$

The summation in the second expression is performed at T values (sample points) of normalized indentation depth δ/R_C. Note that the root-mean-square error is normalized by the forces of a perfectly aligned sphere at the maximum indentation depth ($F(\beta = 0, \delta_{max})$.

Figure 3.8D shows that for $\beta = 0$, the NRMSE value greater than .049 is associated with $> 10\%$ error in the estimated material stiffness, C_{10}. This provides a threshold for an acceptable NRMSE value. Figure 3.8E shows a comparison of normalized force-displacement curves for various values of β alongside the theoretical curve for

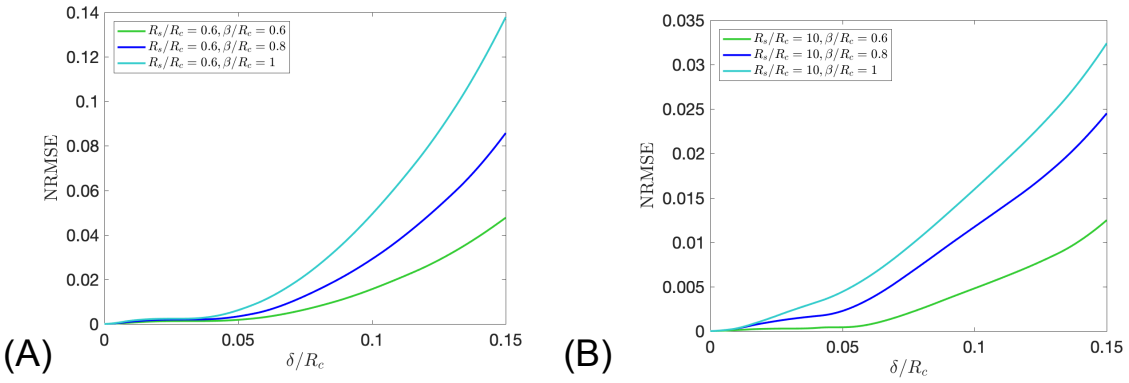

Figure 3.9: Normalized root-mean-square error (NRMSE) plotted over the normalized indentation depth for $R_s/R_c = 0.6$ (A) and $R_s/R_c = 10$ (B). NRMSE is plotted for 3 different offset values ($\beta/R_c = 0.6, .08$, and 1).

a linear elastic material when $R_s/R_c = 1$. With increasing indenter misalignment, greater depths of indentation were observed for a given magnitude of force.

Note that an offset value of $\beta/R_c = 1$ corresponds to forces that are of similar magnitude to a linear elastic approximation (with no offset) as shown in Fig. 3.8E. Since a 10% error in moduli resulted in an NMRSE of 0.049, we used the computational model to seek the range at which NRMSE > 0.049. The NRMSE threshold was found to be exceeded when the ratio of tangential force (F_z) to force magnitude ($||\mathbf{F}||$) was greater than 0.41 as seen by the shaded region in Fig. 3.8F. Any experiments with measured forces of $F_z/||\mathbf{F}|| > 0.41$ were discarded since they could generate significant errors in the determination of moduli.

The effect of the misalignment was quantified for different ratios of R_s/R_c (Fig. 3.9) by comparing the force-displacement curves to the perfectly aligned case ($\beta = 0$). Figures 3.9A-B show the NRMSE for $R_s/R_c = 0.6$ and $R_s/R_c = 10$, respectively.

From our simulations, smaller ratios of R_s/R_c showed larger normalized root-mean-square errors than larger ratios of R_s/R_c. Consequently, for a given indenter size, relatively small cells ($R_s/R_c = 10$), are less affected by misalignment, while larger cells ($R_s/R_c < 1$) are more sensitive to misalignment. Note that for $R_s/Rc = 10$, the NRMSE remained < 0.049 for the entire range of tested β values.

3.6 Materials and Methods

3.6.1 Fabrication of electrospun scaffolds

Electrospinning is a method which uses a sufficiently high voltage to draw charged threads of polymer solution towards a collector plate, resulting in a mat of nano-/microfibers (we call this the scaffold). The applied voltage, polymer viscosity, and flow rate of the drawn polymer threads, are parameters which can be altered to fine-tune the average fiber diameter and scaffold porosity. PVDF solution was prepared to a final PVDF concentration of 15% w/w by adding the polymer pellets to DMF and acetone (1:1). Random fibrous mats were collected on coverslips taped to a grounded metal collector plate located 12-13 cm from the electrospinning syringe tip. Electrospinning was performed at a voltage of 10-12 kV at 3-5 ml/hr flow rate from the syringe.

The resulting PVDF fiber diameters were 1-4 microns and the final overall scaffold thicknesses ranged between 50-100 microns. Scaffolds needed to be thin and porous

to allow sufficient spacing for unobstructed transmission of the trapping laser along the Z-axis. Scaffolds were carefully removed from the collector plates and adhered along the edges of the coverslips with "liquid bandaid" glue to ensure continued attachment during cell culturing. The coverslips were then placed in 6-well culture plates. Prior to introducing cell cultures, the wells containing the coverslips were UV-sterilized and immersed in 1X PBS at 37 °C in an incubator overnight [151]. Although PVDF is a piezoelectric polymer fiber, we were not concerned with the traction forces of cells creating significant charges since the piezoelectric coefficient for PVDF is approximately 20-30 pC/N [152] and peak cellular tractions are typically on the order of 100-300 pN/μm^2 [153, 154].

3.6.2 Cell culture

For primary mixed glia culture, cortices of mouse pups (Jackson Laboratory) P3-6 were isolated and plated on the PLL (Poly-L-Lysine)-coated T-75 culture flasks in DMEM/F12 50:50 media (Corning,15-090-CV) with 10% FBS and 1% antibiotics as per our previous protocol ([155]). The primary glia culture was maintained with a media change every three to four days. After 14 days of culture, glial cells were isolated by shaking the flask at 180 rpm at 37°C overnight. Cells were maintained for at least 3-4 days at 5% CO2 and 37°C incubation before seeding cells into the electrospun scaffold at a density of 1×10^6 cells per 100 μL of media. Once cells were added to the scaffolds at a high density, the scaffolds were incubated for 30

minutes for better attachment prior to adding more media. Once seeded on the cell scaffolds, cells were given 7-10 days to grow processes before performing indentation experiments. Although cell attachment and process growth was faster during the first few days for the PVDF scaffolds with a positive surface charge, after 7 days there was no significant difference in morphology between the cells grown in positively or negatively charged scaffolds. The glial cells grew processes along the length of the electrospun fibers, consistent with previous reports of glial cells grown in electrospun polymer scaffolds ([156], [131]).

Two hours prior to the indentation experiments, media from the scaffold culture plate was removed and washed once with 1X PBS. Cell surfaces were biotinylated with EZ-link Sulfo-NHS-Biotin at a final concentration of 2 mM (ThermoFisher: Cat # 21217). Cells were then washed three times with 100mM Glycine-PBS (VWR: Cat # VW1479-02) to remove excess biotin. Finally, cells were incubated in 500 nM of Calcein-AM (Life Technologies: Cat # C1430) in plain DMEM/F12 50/50 media in order to ensure cells were alive during mechanical testing, as well as to help distinguish cellular processes from the scaffold fibers.

3.6.3 Electron microscopy

Transmission electron microscopy (TEM) was used to obtain a cross sectional view showing the cellular morphology. In order to approximate the cellular specimen as a cylinder adhered to the scaffold fiber, we wanted to make sure that the cell

processes exhibited a circular profile (and not a flattened surface in contact with the indenter). TEM samples were fixed with 2.5% glutaraldehyde and 3mM magnesium chloride in 0.1M sodium cacodylate (SC) for 1 hour. Cells were washed in a 0.1M SC, 3mM magnesium chloride (CaCl2), and 3% sucrose buffer in three 10 minute rinses and incubated (on ice and in the dark for 1 hour) in reduced 1% osmium with 0.8% potassium ferrocyanide in 0.1 M sodium cacodylate. This was followed by three 0.1M maleate buffer rinses and en bloc stained with 2% uranyl acetate (0.22 μm filtered, 1hr, dark) in 0.1M maleate buffer. Cells were dehydrated in a graded series of ethanol before embedding in EPONATE 112 resin (Ted Pella). Samples were incubated at 37°C for 2-3 days before moving to a 60°C oven overnight. Regions of interest were selected and sections picked up on 2x1 mm copper slot grids (Ted Pella, Inc., Redding, CA, USA). Sections were triple stained with 1% tannic acid (aqueous) (Mallinckrodt Pharmaceuticals, St. Louis, MO, USA), aqueous 2% uranyl acetate (Polysciences, Inc., Warrington, PA, USA) and 0.04% lead citrate (aqueous-filtered). Samples were imaged on a Philips CM120 TEM with a 16-bit, 8 megapixel AMT XR80 CCD.

3.6.4 Cell immunostaining

In order to identify the glial cell types, immunostaining of cells was performed on fixed cells. The cells were cultured for 6-7 days in scaffolds at 300k cells per well (lower than previous experimental conditions) for better observation of cellular processes. Cultures were washed with phosphate-buffered saline (PBS) and fixed for 20 minutes

at room temperature with 4% paraformaldehyde (PFA). Cells were washed twice in PBS following fixation and incubated in blocking solution, containing 0.25% Triton-X and 5% normal donkey serum for 1 hour at room temperature.

Different combinations of primary antibodies for separate wells were prepared: rabbit GFAP (1:1000, Dako, Cat Z0334) with mouse-microtubule MT (1:500, Invitrogen, Cat 322700), rabbit-Oligodendrocytes (1:1000, Millipore, Cat 371726) with mouse-microtubule, and finally a combination of rabbit-IBA1(1:1000, Wako Chemicals, Cat 019-19741) and mouse-microtubule diluted in blocking solution. Blocking solution was applied overnight at 4°C. Cultures were washed three times in PBS and incubated with Alexa Fluor 555-conjugated donkey anti-rabbit (1:250, Invitrogen) and Alexa Fluor 488-conjugated donkey anti-mouse (1:250, Invitrogen) for 2 hours at room temperature. Wheat germ agglutinin, Alexa Fluor 647 conjugated (Invitrogen, Cat W32466), was added at 5 μg/ml in 1X HBSS for 10 minutes at room temperature, washed 2X with 1X HBSS followed by incubation for 5 minutes with 1 μM of DAPI ((4', 6-diamidino-2-phenylindoldihydrochloride, Invitrogen) as a nuclear counter-stain. The coverslips were mounted in slides post drying and images were taken in confocal LSM-800. Results from the immunostaining are presented in Chapter 5.

3.7 Concluding remarks

Here we have provided a description of the principles behind our experimental setup, and an analysis of the limitations due to alignment issues, optical trap holding strength, and noise within the experiment. The final aspect of the experiment that needs further consideration is the accurate analysis of the measured force-displacement relationship to provide nonlinear material properties. Although some papers describe hyperelastic indentation formulations for flat cells, none have considered hyperelastic indentation on cylindrical-shaped cells. The following chapter considers the latter geometry, and uses computational modeling to develop the appropriate force-displacement relationships for use with cylindrical bodies having nonlinear hyperelastic material properties.

Chapter 4

Nonlinear contact mechanics for indentation of hyperelastic cylindrical bodies

4.1 Introduction

Measuring the mechanical response of biological cells is an important key to developing new biomedical materials [157], understanding injury or disease progression [34] [158] [159], and potentially improving clinical diagnostic technologies [160] [14]. Commercially available indenters such as the atomic force microscope (AFM) have made it possible to estimate the elastic moduli of cells by applying the well-known Hertzian contact theory to experimentally measured forces and displacements. Al-

though the elastic moduli of cells are accurately found for small indentations, some cells can be subjected to large deformations due to their soft nature, often surpassing the linear elastic regime associated with classic Hertz theory [161] [58] [162]. Since the usefulness of the elastic modulus is limited, it is desirable to obtain hyperelastic parameters that can account for the finite deformations [149] [150] and strain stiffening behavior [163] of biological materials.

In classical Hertz theory [164], aside from assuming an isotropic linear elastic material, the solution is limited to small deformations since the shape of the spherical indenter is given by a parabolic function approximated as $r^2/2R_s$, where r is the radial coordinate and and R_s is the indenter radius [165], [166]. It is possible to model larger indentation depths (up to 0.8 times the indenter radius) by using a higher order function to describe the spherical indenter [167]. However, such a solution will still be limited by providing only the linear elastic modulus from the experimentally found forces and displacements.

In recent decades, several approaches have been taken to modify the Hertz solution, in order to obtain parameters that describe the material of the specimen as hyperelastic. The first approach involves the derivation of an approximate analytical expression, and validation of the expression with a finite element calculation [56] [168]. A second approach is to use a finite element model to investigate the effects of hyperelasticity on indentation and then create correction factors to use in conjunction with the equations of Hertzian theory [169] [170]. Finally, if the sole purpose of a

study is to determine the material properties in a specific experiment, it is possible to disregard the classical Hertzian solution, and parametrically run a series of finite element simulations, varying the material properties for a given constitutive model, until the experimentally found force-displacement relationships are obtained [4] [171].

However, the aforementioned solutions are for the case of a rigid sphere indenting a half space or another spherical body. There are no force-displacement relationships that exist for finding hyperelastic parameters in structures with a cylindrical morphology. Quantifying these relationships is essential for finding properties of cylindrical cellular structures—neuronal axons, cell processes, filopodia, and certain types of bacteria, to name a few—that undergo large deformations during indentation testing. Here we only consider a spherical indenter, as previous works have found that pyramidal indenters produce stresses and indent depths that are too large for cells [172] [146].

The ratio of length scales between the indentation depth, indenter radius, and specimen radius is important for selecting the appropriate indentation formulation. The indentation depth is given by δ, R_s is the radius of a spherical indenter tip, and R_c is the radius of the cell. For indenter tips with a radius much smaller than the radius of the cell ($R_s << R_c$), one can approximate that the cell is a half space, and it is no longer necessary to consider the cylindrical morphology. Although AFM indenter tips with small radii (<100 nm) are readily available, a larger indenter tip might be desirable in applications where it is necessary to probe mechanical properties over a larger area [173], [174], [175], to avoid nonlinear effects [176], [57], or create loads over

a larger area when studying cellular injury [177] and mechanotransduction [178].

In this paper we use a computational model to investigate the force-displacement relationships for spherical indentation into hyperelastic cylindrical bodies (Figure 4.1). We provide analytical expressions, with the calculated corrective functions, that can be used to obtain hyperelastic material properties from indentation testing on flat and cylindrical bodies (using both flat and spherical indenters). The force-displacement relationships were found to be dependent on the ratio of indenter to specimen radius (R_s/R_c), as well as the ratio of indentation to indenter size (δ/R_s). We observe the strains at which the indentation is large enough that the solution deviates from linear elastic theory. Finally, we evaluate the proposed hyperelastic corrective functions for large indentations in order to quantify the extent of error due to interactions with the substrate.

4.2 Methods

4.2.1 Elliptical contact onto linear elastic bodies

In the case of a rigid spherical indenter in contact with a flat half-space made of an isotropic linear elastic material, the force-displacement relation is given by the classical Hertz solution:

$$F_H = \frac{4}{3} R_s^{1/2} \frac{E}{1-\nu^2} \delta^{3/2} \tag{4.1}$$

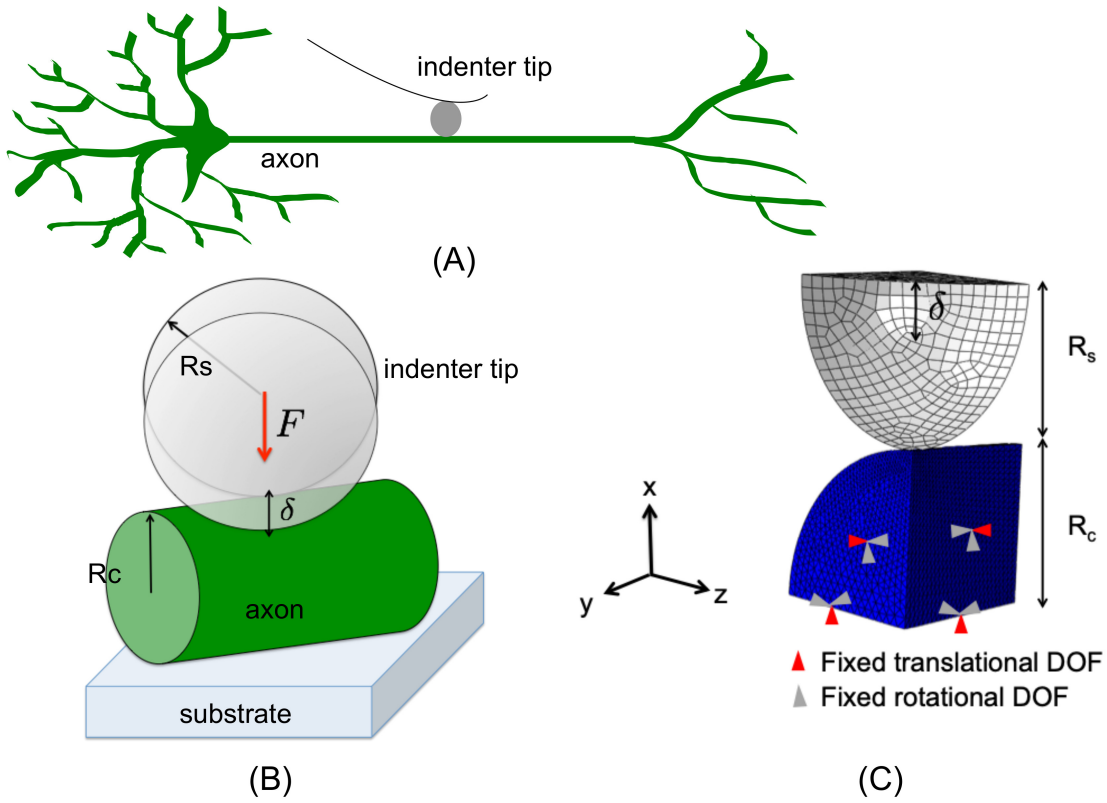

Figure 4.1: (A) Example of a cylindrical body (e.g. axon) subjected to indentation by a spherical indenter. (B) Experiment is simplified as a sphere indenting a cylindrical body (C) A finite element model of spherical indentation. Note that due to symmetry, only one-fourth of the model needed to be simulated. The indenter was modeled as a rigid body and displaced along the negative x-direction by δ.

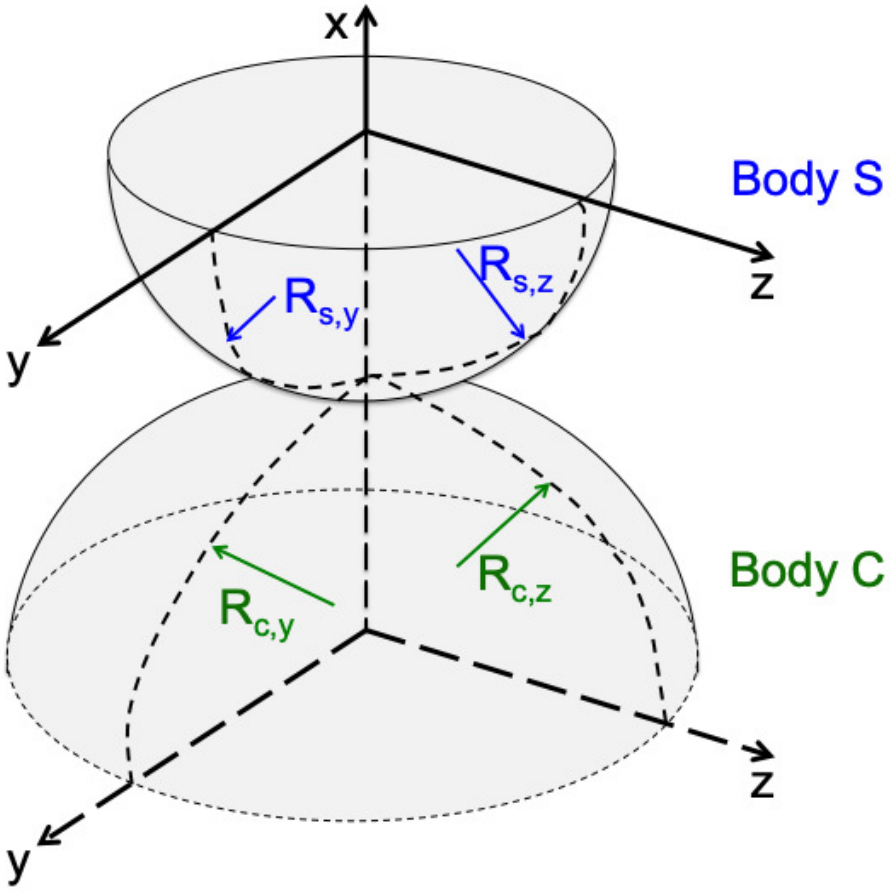

Figure 4.2: Generalized case of two ellipsoidal volumes ('Body S' and 'Body C') and their respective geometries. The equivalent radii of curvature are given in equations 4.3 and 4.4. In the case of a spherical indenter (Body S), $R_{s,y} = R_{s,z}$. For a cylindrical specimen (Body C) with the longitudinal axis aligned in the y-direction, $R_{c,y} \to \infty$.

Where F_H is the magnitude of the force applied to the indented body (e.g., a cell), R_s is the effective radius of the spherical indenter, ν is the Poisson's ratio of the cell, and E is the Young's modulus of the cell. This relationship is for a spherical contact area, and can only be used when probing the somal (spherical) compartment of a cell, or a large, flat cell with a radius of curvature much larger than the indenter.

In the case of the silica bead indenting an axon or cell process, this can be idealized as a rigid sphere (with radius R_s) indenting a cylindrical body (with radius R_c), and thus an elliptical contact area is formed. A schematic of two generalized ellipsoidal shaped bodies and their respective geometries is shown in Fig. 4.2. To account for the eccentricity in the contact area, correction factors are used to modify Equation 4.1. We will also introduce the parameters R_z and R_y which are the effective radii of curvature in the z-plane and y-plane, respectively. The effective curvature sum R, a quantity of importance in the analysis of contact mechanics, is defined by [179] [180]:

$$\frac{1}{R} = \frac{1}{R_z} + \frac{1}{R_y} \tag{4.2}$$

where

$$\frac{1}{R_z} = \frac{1}{R_{c,z}} + \frac{1}{R_{s,z}} \tag{4.3}$$

$$\frac{1}{R_y} = \frac{1}{R_{c,y}} + \frac{1}{R_{s,y}} \tag{4.4}$$

For a cylinder where $R_{c,y}$ goes to infinity, the last expression simplifies to $R_y = R_{s,y}$. For a spherical indenter, $R_{s,z} = R_{s,y}$. Now, the relation for force-displacement during

an elliptical contact for this linear elastic case can be written as:

$$F_{ellip}^{LE} = \frac{2\pi}{3}(2R)^{1/2}\frac{E}{1-\nu^2}\delta^{3/2}\chi_{ellip} \tag{4.5}$$

Where χ_{ellip} is a product which is solely dependent on the ratio between the indenter radius R_s and the cylinder radius R_c and can be written as:

$$\chi_{ellip} = k\mathcal{F}^{(-3/2)}\mathcal{E}^{1/2} \tag{4.6}$$

where k is the eccentricity parameter of the contact area (given as the ratio of semi-major to semiminor axis), $\mathcal{F}$ is the complete elliptic integral of the first kind, and $\mathcal{E}$ is the complete elliptic integral of the second kind. The eccentricity parameter is related to the elliptic integrals of the first and second kind [165], [180]:

$$k = \sqrt{\frac{2\mathcal{F} - \mathcal{E}(1+\gamma)}{\mathcal{E}(1-\gamma)}} \tag{4.7}$$

where

$$\gamma = R(\frac{1}{R_z} - \frac{1}{R_y}) \tag{4.8}$$

$$\mathcal{F} = \int_0^{\pi/2} [1 - (1 - \frac{1}{k^2})\sin^2\phi]^{-1/2} d\phi \tag{4.9}$$

$$\mathcal{E} = \int_0^{\pi/2} [1 - (1 - \frac{1}{k^2})\sin^2\phi]^{1/2} d\phi \tag{4.10}$$

One can numerically evaluate the elliptical equations using iterative procedures or utilizing lookup tables [181]. Here, in order to provide the most useful result to the reader, we will utilize the algebraic approximations from Brewe and Hamrock

(1977) [179] to replace the elliptical integrals of $\mathcal{F}$ and $\mathcal{E}$ with numerically found approximations of $\overline{\mathcal{F}}$ and $\overline{\mathcal{E}}$. These are given by:

$$\overline{\mathcal{F}} = 1.5277 + .6023 \ln \frac{R_y}{R_z} \tag{4.11}$$

$$\overline{\mathcal{E}} = 1.0003 + \frac{0.5968 R_z}{R_y} \tag{4.12}$$

The approximate eccentricity parameter is now approximated:

$$k \approx \sqrt{\frac{2\overline{\mathcal{F}} - \overline{\mathcal{E}}(1+\gamma)}{\overline{\mathcal{E}}(1-\gamma)}} \tag{4.13}$$

It follows that the approximate expression for χ_{ellip} is now given by:

$$\chi_{ellip} \approx k\overline{\mathcal{F}}^{(-3/2)}\overline{\mathcal{E}}^{1/2} \tag{4.14}$$

Thus, we can rewrite the relation for force-displacement during an elliptical contact as a product of the classic Hertzian force relationship (F_H) and a correction factor, that depends on the ratio of R_s to R_c, which we will call Ω^{LE}_{ellip}:

$$F^{LE}_{ellip} = \frac{2\pi}{3}(2R)^{1/2}\frac{E}{1-\nu^2}\delta^{3/2}k\overline{\mathcal{F}}^{-3/2}\overline{\mathcal{E}}^{1/2} \tag{4.15}$$

$$= F_H \Omega^{LE}_{ellip} \tag{4.16}$$

where

$$\Omega^{LE}_{ellip} = \frac{\pi\chi_{ellip}}{\sqrt{2}}\frac{\sqrt{\frac{R_s R_c}{2R_c+R_s}}}{\sqrt{R_S}}. \tag{4.17}$$

The superscript LE denotes that these expressions are for linear elastic bodies. Note that the force-displacement $F-\delta$ relationship retains the 3/2 power, arising out of linear elasticity.

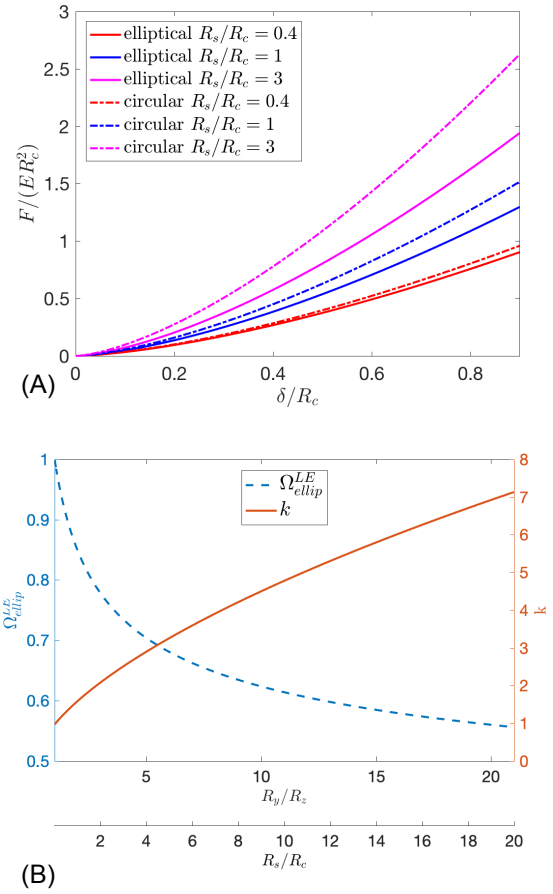

Figure 4.3: (A) Non-dimensional plot of the force-displacement relationship for different ratios of R_s/R_c. Solid lines show $F - \delta$ curves using the elliptical contact formulation of Eqn. 4.16, whereas dashed lines show the $F - \delta$ relationships with a circular contact area (classical Hertz theory). (B) Plot of the elliptical contact correction factor Ω^{LE}_{ellip} (orange) and eccentricity ($\overline{k}$, blue) as a function of varying R_s/R_c (and hence, R_y/R_z).

A comparison between the force-displacement relationships of Equations 4.1 and 4.16 is shown in Figure 4.3A. The ratio between the indenter tip size versus specimen size will effect the ellipticity of the contact area, determining the usefulness of Equation 4.16. Figure 4.3A shows that for sufficiently small indenter tips ($R_s/R_c \leq 0.4$), the elliptical contact solution differs from the circular contact solution (Equation 4.1) by $< 6\%$ for extremely large indentations ($\delta/R_c = 0.9$). In other words, if the radius of the cylindrical specimen is at least 2.5 times larger than the indenter tip, the elliptical contact solution approaches the classic Hertzian solution (analogous to a sphere indenting a half-space). For large values of the size ratio R_s/R_c, the eccentricity will become large enough that the behavior will approach a line contact formulation ($k \approx 10$).

Figure 4.3B plots the eccentricity parameter k and the elliptical contact correction factor Ω^{LE}_{ellip} as a function of R_s/R_c. Note that if R_y/R_z=1, then $\mathcal{F} = \mathcal{E} = \pi/2$, $k = 1$, and there is no need to use Ω^{LE}_{ellip} ($\Omega^{LE}_{ellip} = 1$) since it is a circular contact area. As R_s/R_c becomes large, k also becomes large, and will eventually approach the limit of a rectangular line contact. For all values of R_s/R_c, Ω^{LE}_{ellip} must be ≤ 1 (and hence $F^{LE}_{ellip} \leq F_H$).

4.2.2 Elliptical contact on hyperelastic neo-Hookean bodies

The preceding section considered a linearly elastic material subjected to small deformation. In the case of biological materials subjected to large deformation, a hyperelastic material model is more appropriate. We begin by considering a neo-Hookean material (perhaps the simplest constitutive model within the class of hyperelastic models). The neo-Hookean model for an incompressible material uses a strain energy density of the form:

$$W_{NH} = C_{10}(I_1 - 3); \tag{4.18}$$

where C_{10} is a material property and I_1 is the first invariant of $\mathbf{C}$ (the right Cauchy-Green deformation tensor). In the small strain regime, the material constant C_{10} can be related to the linear elastic shear modulus μ and linear elastic Young's modulus through $C_{10} = \mu/2 = \frac{E}{4(1+\nu)}$, where ν is the Poisson's ratio. For an incompressible material, $\nu = 0.5$.

For the case of a neo-Hoookean body subjected to spherical indentation, we propose a solution which takes the form:

$$F_{NH} = F_H \Omega^{LE}_{ellip} \Omega_{NH} \tag{4.19}$$

$$= \frac{2\pi}{3}(2R)^{1/2}\frac{E}{1-\nu^2}\delta^{3/2}\chi_{ellip}\Omega_{NH} \tag{4.20}$$

where Ω_{NH} is a new correction function that must be solved for. Although Ω^{LE}_{ellip}

is solely dependent on the ratio between the indenter radius and specimen radius (R_s/R_c), the correction factor for the neo-Hookean material will have an additional dependence on the extent of deformation since hyperelastic materials exhibit stiffening at larger strains. Here, the extent of deformation is characterized by the ratio between indentation depth and the indenter radius (δ/R_s). Thus, Ω_{NH} will be dependent on (δ/R_s) and (R_s/R_c). For simplicity in calculating the material property C_{10} (explained in later sections), the following sections will obtain expressions for the corrective function Γ_{NH} (the inverse of Ω_{NH}):

$$\Gamma_{NH}(\delta/R_s, R_s/R_c) = \frac{1}{\Omega_{NH}}. \tag{4.21}$$

4.2.3 Elliptical contact on hyperelastic Mooney Rivlin bodies

A Mooney-Rivlin material model is another hyperelastic constitutive model that is considered an extension of the neo-Hookean model since it incorporates a second invariant of the left Cauchy-Green tensor. For an incompressible material, its strain energy takes the form:

$$W_{MR} = C_{10}(I_1 - 3) + C_{01}(I_2 - 3) \tag{4.22}$$

where C_{10} and C_{01} are material constants. Generally speaking, expressions which include the dependence on the second invariant can model the stress response of rubber-like materials and soft biomaterials more accurately [182]. For small deformations, the

constants C_{10} and C_{01} are related to the elastic modulus by $E = 4(1+\nu)(C_{10}+C_{01})$. For $C_{01} = 0$, Equation 4.22 reduces to the neo-Hookean strain energy. Similar to the correction factor for the neo-Hookean body Ω_{NH}, an expression for a Mooney Rivlin body subjected to spherical indentation will have a correction factor Ω_{MR}:

$$F_{MR} = F_H \Omega^{LE}_{ellip} \Omega_{MR} \tag{4.23}$$

Again, we will be finding solutions to the inverse corrective function: $\Gamma_{MR} = \frac{1}{\Omega_{MR}}$. In this case, the corrective function will have an additional dependence on the ratio between the parameters C_{10} and C_{01}. Therefore, Γ_{MR} will be a function of (δ/R_s), (R_s/R_c), and κ, where κ is a dimensionless parameter defined by:

$$\kappa = \frac{C_{10}}{C_{10}+C_{01}} \tag{4.24}$$

Note that $\kappa = 1$ corresponds to a neo-Hookean material.

4.2.4 Computational model

4.2.4.1 Geometry considerations

3D finite element simulations of spherical indentation on cylindrical specimens were performed with the commercially available software Abaqus (Dassault Systèmes Simulia Corp.). The indentation was simulated as frictionless contact between a rigid sphere (with R_s varying between 2 to 100 μm), and a cylindrical specimen ($R_c = 5\mu$m) with either linear elastic or hyperelastic material properties. Figure 4.1C shows the

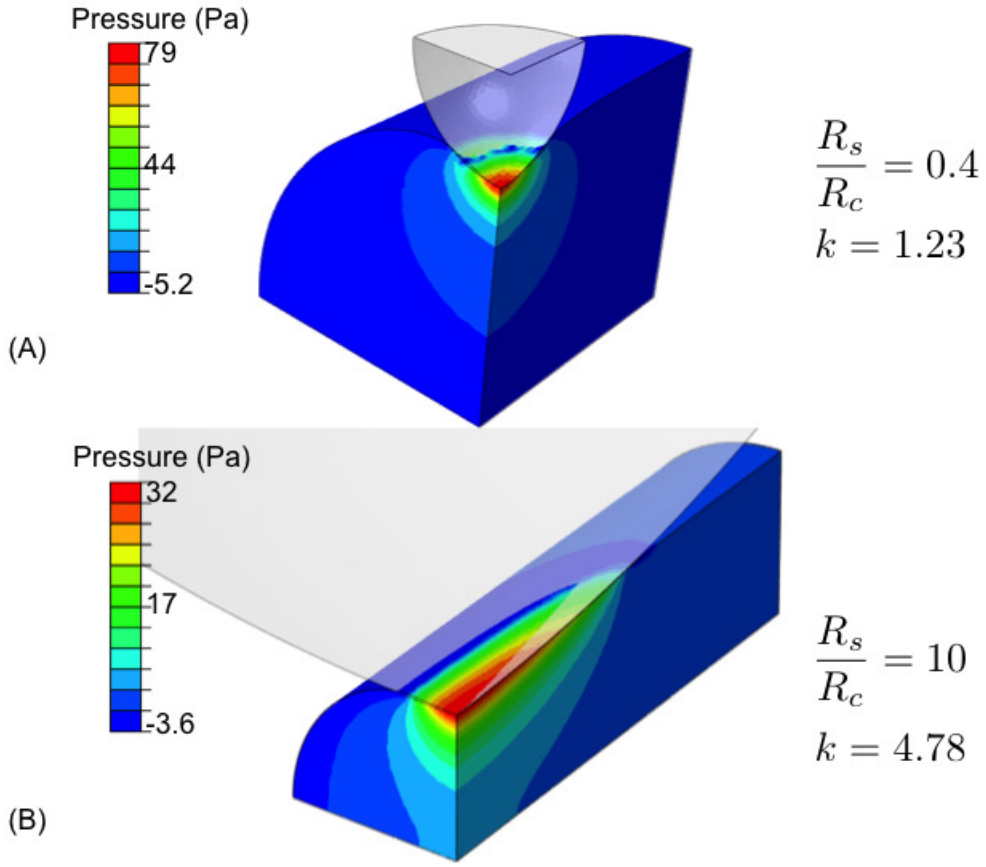

Figure 4.4: Example of finite element simulations which demonstrate the effect of R_s/R_c ratios on the ellipticity of the contact area. For $R_s/R_c = 0.4$ (top simulation), the contact area is almost circular, while for $R_s/R_c = 10$, the contact area has greater eccentricity (k).

computational model with the applied boundary conditions. Taking advantage of symmetry, a quartered section of the model, with approximately 200-400k ten-node quadratic tetrahedral elements, was utilized to reduce computational costs. The magnitude of indentation strain (δ/R_c) remained constant across all simulations, while a different R_s/R_c value was used for each simulation. A total of six indenter sizes were simulated, with R_s equal to 2, 3, 5, 7, 10, 20, 30, 50, 75, and 100 μm. These correspond to R_s/R_c ratios of 0.4, 0.6, 1, 1.5, 2, 4, 6, 10, 15, and 20, respectively. Consequently, the maximum value of δ/R_s will be different across each simulation.

The range of R_s/R_c values were determined by considering the appropriate amount of ellipticity. It was shown in the previous section that for $R_s/R_c < 0.4$, the ellipticity parameter $k \to 1$, and the indentation can be approximated by a circular contact formulation, such as those provided by Lin et al. 2009 [56]. At the upper limit, a line contact exists for large values of k, or when $R_s/R_c \approx 20$ (see Fig. 4.4). This range is also applicable to experimental data since commonly used silica bead indenter tips range from 5-100 microns while probing cellular components with cylindrical radii on the order of 1-10 microns.

For simulations with larger ellipticity in the contact area (larger indenters), the cylindrical specimens were made to be geometrically longer along the longitudinal direction (y-axis) so that the free boundary normal to the y-axis would not affect the solution. Across all models, the length of the specimen was made to be approximately twice as long as the major axis of the contact area during the maximum indentation

depth.

4.2.4.2 Material parameters

For each of the seven indenter sizes, three different types of material models were implemented for the cylindrical specimen: linear elastic, neo-Hookean, and Mooney Rivlin. For the linear elastic material model, we used a Young's modulus of $E = 100$ Pa and assumed that the specimen was incompressible ($\nu = 0.5$). Note that the correction factors for Ω_{ellip}, Γ_{NH}, and Γ_{MR} are dimensionless functions that do not depend on the specific material parameters. For the Mooney Rivlin models, additional simulations with varying κ values (κ=0.1, 0.2, 0.3, ...1.0) were performed for each ratio of R_s/R_c.

4.2.4.3 Mesh convergence

The mesh size of the cylindrical specimen was biased to be more refined near the area of contact with the indenter. A mesh convergence study was performed for the linear elastic model of the smallest R_s/R_c ratio, since this was the case that corresponded to the largest indentation strains. To find the necessary minimum element size, several simulations were performed with the smallest element size at the center of contact varying between 2.5×10^{-5} mm and 5×10^{-4} mm. Although all simulations (including the coarsest mesh) were able to accurately resolve the theoretical force-displacement curves at small strains (F^{LE}_{ellip} of Eq. 4.16), it was found that a

minimum element size of 1×10^{-4} mm was necessary for the convergence of the total internal energy.

4.2.4.4 Boundary conditions

The rigid sphere was displaced by $\delta = 700$ μm in the negative x-direction in 100 ms. This loading rate is comparable to some AFM experiments [56], however, it should be noted that viscoelastic effects are not considered in these computations. The interface between the indenter and specimen was assumed to be frictionless. The model was given symmetric boundary conditions along surfaces normal to the positive y- and z-directions and the negative x-direction, while it remained free to expand in the negative y-direction. A schematic of the fixed translational and rotational degrees of freedom which create the symmetric boundary conditions is shown in Figure 4.1C. In summary, the negative x-normal plane of symmetry was not allowed to move in the x-direction, the positive y-normal plane was not allowed to move in the y-direction, and the z-normal plane of symmetry was not allowed to move in the z-direction.

4.2.5 Calculation of corrective functions

Since analytical expressions are known for F_H and Ω_{ellip}, our aim is to utilize the results from the following sections to obtain expressions for the correction functions Γ_{NH} and Γ_{MR}. After obtaining these correction functions, simplistic algebraic expressions are provided and can be used to extract hyperelastic material properties

from experiments of cylindrical specimens undergoing spherical indentation.

In order to obtain algebraic expressions for the corrective functions, we obtained the *simulated* corrective factors $\widehat{\Gamma}_{NH}(\delta/R_s)$ and $\widehat{\Gamma}_{MR}(\delta/R_s)$ from various R_s/R_c values over a useful range. Hereafter we will use the symbol ($\widehat{-}$) to denote the values obtained with the finite element model. Each simulation provides a total reaction force (F_{NH} or F_{MR}), which can be divided by the analytical expression of F^{LE}_{ellip} (Equation 4.16) in order to obtain the corrective factors $\widehat{\Gamma}_{NH}(\delta/R_s)$ and $\widehat{\Gamma}_{MR}(\delta/R_s)$, respectively. From $\widehat{\Gamma}_{NH}(\delta/R_s)$ and $\widehat{\Gamma}_{MR}(\delta/R_s)$ it is possible to deduce the final expressions for $\Gamma_{NH}(\delta/R_s, R_s/R_c)$ and $\Gamma_{MR}(\delta/R_s, R_s/R_c, \kappa)$.

Results

Linear elastic specimen simulations

Although the aim of this study is to obtain corrective functions to describe the specimen with a nonlinear constitutive model, an analogous "corrective factor" ($\widehat{\Gamma}_{LE}$) can be computed which compares the FEM simulation of a linear elastic (LE) specimen with the theoretical curve for F^{LE}_{ellip}. The analytical solution of F^{LE}_{ellip} can be divided by the total reaction force obtained during a given simulation (F_{LE}) in order to obtain $\widehat{\Gamma}_{LE}$ such that:

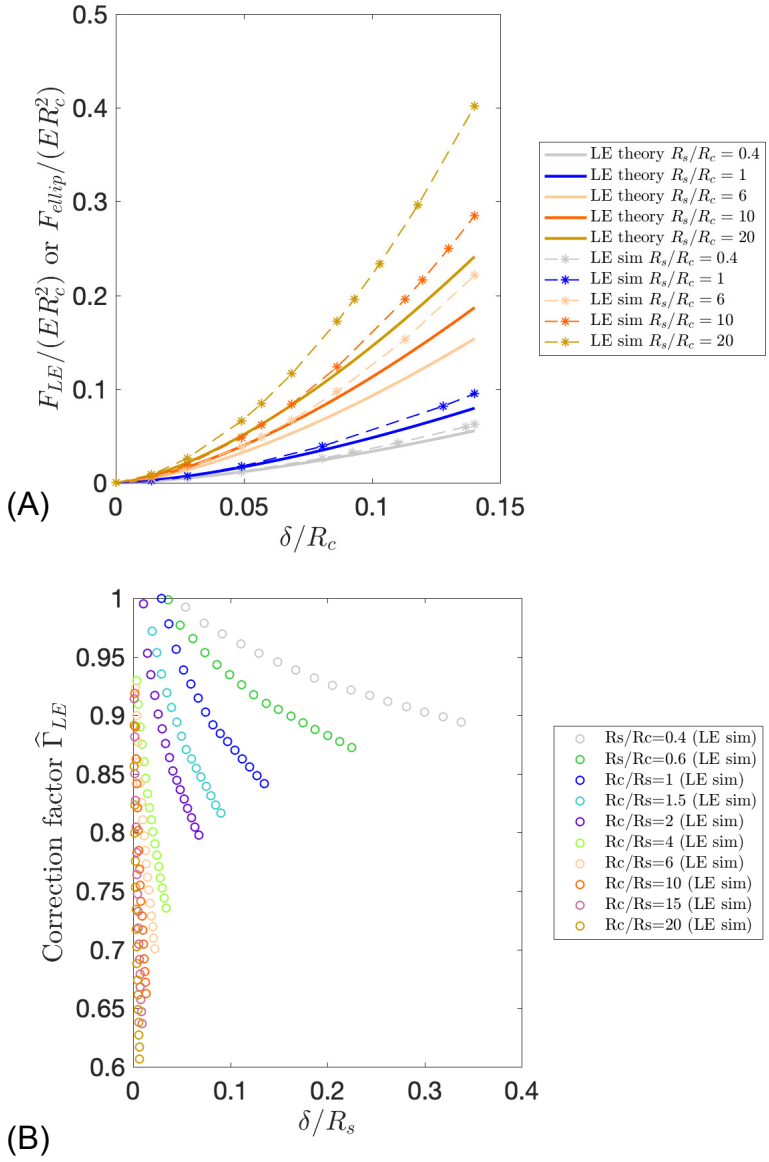

Figure 4.5: (A) Non-dimensional forces (both simulations and theoretical) plotted over non-dimensional indentation depth for various values of R_s/R_c with a linear elastic (LE) specimen. Each curve corresponds to a value of R_s/Rc. Finite element simulations (dashed lines) are compared to the linear elastic theory of elliptical contact (solid lines) given in Equation 4.16. (B) The calculated correction factors ($\widehat{\Gamma}_{LE}$) from the simulations of a linear elastic specimen. $\widehat{\Gamma}_{LE}$ measure the deviation from the linear elastic theory of elliptical contact, and is plotted over the non-dimensional indentation δ/R_s.

$$\widehat{\Gamma}_{LE} = \frac{F^{LE}_{ellip}}{F_{LE}} = \frac{F_H \Omega^{LE}_{ellip}}{F_{LE}} \tag{4.25}$$

Due to the discretization of surface elements in the finite element model, the simulation will be inherently inaccurate for very small indentations. In order to find the minimum indentation depths that allow for an accurate FEM solution, we began by performing simulations with a linear elastic material model for the cylindrical specimen. At the indentation depth where the linear elastic simulation matches the elliptical contact theory, the simulation matches the theoretical curve for F^{LE}_{ellip}, and we therefore only consider fitting the corrective functions beyond this indentation depth.

A comparison between the theoretical force-displacement relationship of Equation 4.16 for various values of R_s/R_c and simulations with linear elastic specimens is shown in Figure 4.5. In Figure 4.5A, the non-dimensional forces (for both the simulation and theoretical F^{LE}_{ellip}) are plotted against δ/R_s. For small values of R_s/R_c (approaching the behavior of spherical contact), the linear elastic theory for elliptical contact (Eq. 4.16) predicts the behavior quite accurately, even for fairly large indentation ($\delta/R_c > 0.1$). For larger values of R_s/R_c and larger indentations ($\delta/R_c > 0.1$), the simulations deviate farther from Equation 4.16, as shown more clearly in Figure 4.5B. This is due to a decrease in accuracy of the algebraic expressions in Equations 4.7, 4.9, and 4.10 for larger values of eccentricity k [179].

For a given R_s/R_c, when $\widehat{\Gamma}_{LE} = 1$, the indentation is large enough for the sim-

ulation to be considered accurate enough for obtaining corrective functions. Figure 4.5B plots $\widehat{\Gamma}_{LE}$ over the relative indentation δ/R_s. The divergence of $\widehat{\Gamma}_{LE}$ from 1 is a result of two causes: 1) larger indentations creating a deviation from small strain theory and 2) larger ratios of R_s/R_c (and consequently, larger eccentricity values) impart less accuracy in Γ_{ellip}. The values of δ/R_s at which $\widehat{\Gamma}_{LE} = 1$ are smallest for the largest values of R_s/R_c, since a larger indenter will impart a larger area of contact onto the specimen (therefore, the limiting mesh size within the contact area becomes less significant).

Neo-Hookean specimen simulations

Figure 4.6A compares Equation 4.16 to the force-displacement response obtained from simulations with neo-Hookean (NH) specimens across various ratios of R_s/R_C. The neo-Hookean contact also shows increased deviation from the theoretical elliptical contact theory (F^{LE}_{ellip}) at higher values of R_s/R_c and at higher relative indentations (δ/R_s). For comparison, the elliptical contact theory curves used a Young's modulus of $E = 4C_{10}(1+\nu)$. These results are in agreement with previous indentation studies on hyperelastic materials which have shown that the indentation response is stiffer than that predicted by linear elasticity [168]. As expected, F_{NH} is similar to F_{LE} at small indentation, but begins to differ from F_{LE} at larger indentations (Figure 4.6B).

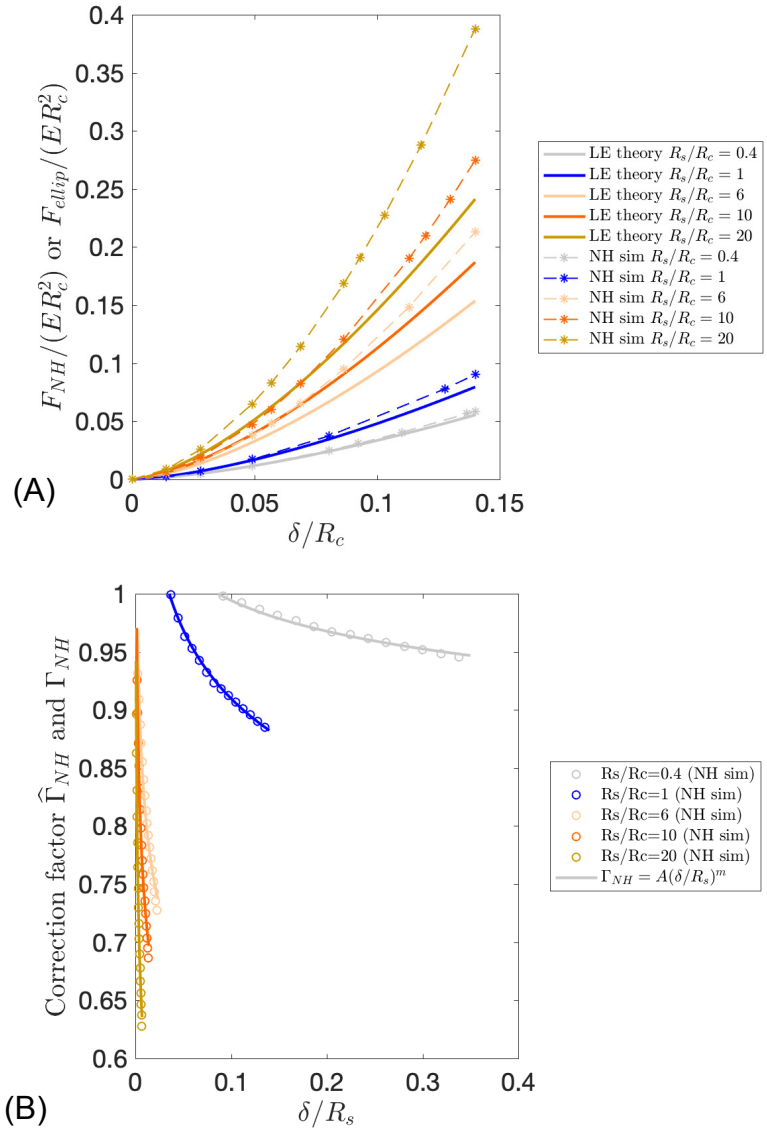

Figure 4.6: (A)Non-dimensional forces (both the simulations of the neo-Hookean specimen as well as the theoretical curve for F_{ellip}^{LE}) plotted over non-dimensional indentation depth for various values of R_s/R_c. Finite element simulations (dashed lines) are compared to the linear elastic theory of elliptical contact (solid lines) given in Equation 4.16. (B) The calculated correction factors ($\widehat{\Gamma}_{NH}$) from the simulations of a neo-Hookean specimen. Each curve corresponds to a value of R_s/R_c. The correction factors calculated from the simulations (circles) are plotted alongside the corresponding fitted power-law functions (solid lines). Only selected values of R_s/R_c are shown for clarity. A complete list of the power-law function coefficients is provided in Table 4.1.

The simulated corrective factors $\widehat{\Gamma}_{NH}$ were calculated by:

$$\widehat{\Gamma}_{NH} = \frac{F^{LE}_{ellip}}{F_{NH}} \tag{4.26}$$

The corrective factors for the neo-Hookean specimen (shown in Figure 4.6B) are plotted as a function of indentation and follow a similar trend to the $\widehat{\Gamma}_{LE}$ factors. That is, it is apparent that the neo-Hookean correction factors are a function of δ/R_s. A power-law function is used to fit the correction factor curves such that:

$$\widehat{\Gamma}_{NH}(\delta/R_s) = A(R_s/R_c)\left(\frac{\delta}{R_s}\right)^{m(R_s/R_c)} \tag{4.27}$$

For a given R_s/R_c, the power law functions were fitted to $\widehat{\Gamma}_{NH}$ for values of δ/R_s that were greater than the indentation at which $\widehat{\Gamma}_{LE}\leq 1$. For clarity, only selected values of R_s/R_c are shown, however a complete list of the fitted power-law function coefficients is provided in Table 4.1.

Figure 4.7 shows that $A(R_s/R_c)$ and $m(R_s/R_c)$ logarithmically decay with increasing the size ratios R_s/R_c. For smaller ratios of R_s/R_c the solution becomes analogous to circular contact with a half-space, and therefore $A \to 1$, $m \to 0$, and $\widehat{\Gamma}_{NH}(\delta/R_s) \to 1$ for all values of R_s/R_c. The corrective function for a neo-Hookean material can now be written in its final form as:

$$\Gamma_{NH} = \left[A_1 \ln(\frac{R_s}{R_c}) + A_2\right]\left(\frac{\delta}{R_s}\right)^{m_1 \ln(\frac{R_s}{R_c})+m_2} \tag{4.28}$$

A summary of the coefficients for the neo-Hookean corrective function are given in Table 4.2. Note that the function $m(R_s/R_c)$ remains small and negative over the range of R_s/R_c.

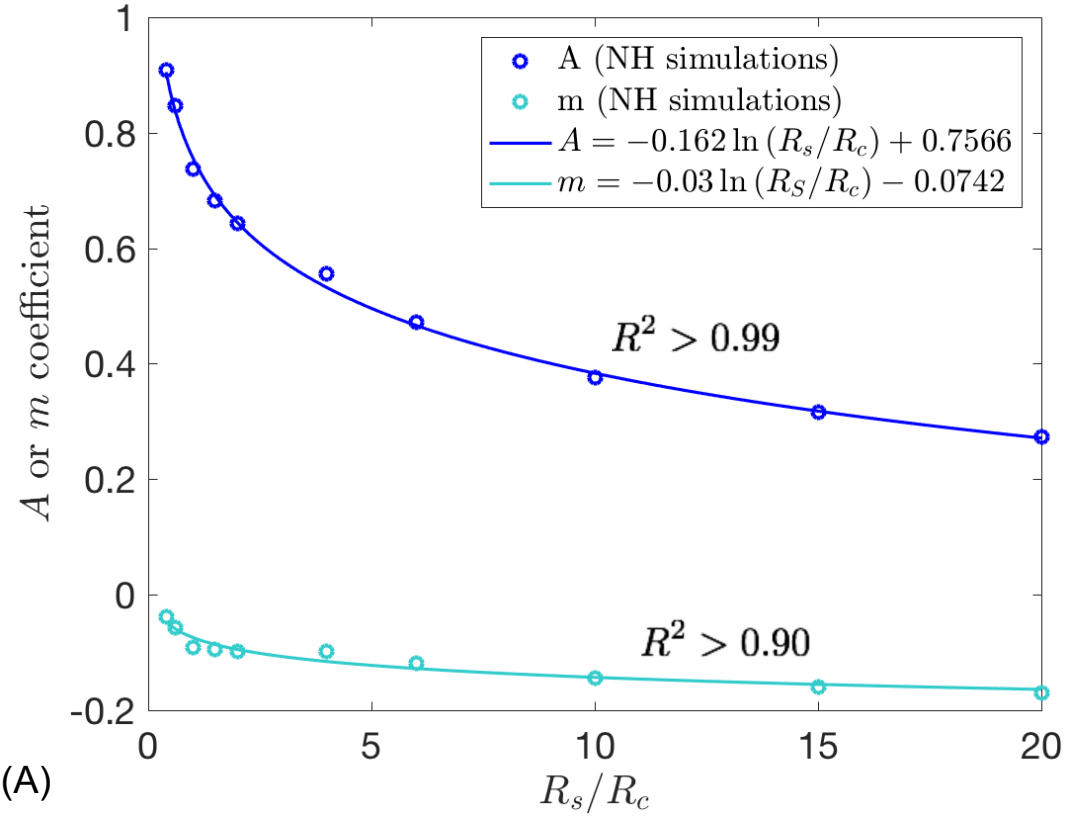

Figure 4.7: A) Logarithmic functions found for curve fitting of Γ_{NH} (solid lines). The logarithmic functions fitted to the simulation results (circles) showed an excellent fit, with R^2 values, or coefficients of determination, greater than 0.90.

Table 4.1: Summary of power-law coefficients, A and m for the corrective functions of Equation 4.28 (neo-Hookean model) for various values of R_s/R_c. The power law functions take the form of $\widehat{\Gamma}_{NH} = A(\frac{\delta}{R_s})^m$

R_s/R_c	A	m
0.4	0.9089	−0.039
0.6	0.8473	−0.056
1	0.7378	−0.091
1.5	0.6824	−0.095
2	0.643	−0.098
4	0.5561	−0.098
6	0.4713	−0.119
10	0.3768	−0.144
15	0.3157	−0.16
20	0.2726	−0.171

4.2.6 Mooney Rivlin specimen simulations

In order to obtain a correction function for the Mooney Rivlin model (MR), simulations with varying parameter ratios (κ=0,0.1, 0.2, 0.3, ...1.0) were performed for each size ratio of R_s/R_c. Since ten different size ratios were considered, this resulted in 110 total simulations analyzed for a Mooney Rivlin specimen. Similar to the previous approach with the linear elastic and neo-Hookean materials, the corrective factors

$\widehat{\Gamma}_{MR}$ are calculated by the relationship:

$$\widehat{\Gamma}_{MR} = \frac{F^{LE}_{ellip}}{F_{MR}} \tag{4.29}$$

For each value of κ, the calculated value of Γ_{MR} plotted over δ/R_s still follows a power-law behavior, however, in contrast to the neo-Hookean simulations, the functions A and m now have an additional dependence on the parameter ratio κ such that:

$$\widehat{\Gamma}_{MR}(\delta/R_s, \kappa) = A(R_s/R_c, \kappa)\left(\frac{\delta}{R_s}\right)^{m(R_s/R_c,\kappa)} \tag{4.30}$$

We begin by finding an expression for the function A for the ten simulations (R_s/R_c =0.4, 0.6, 1, 1.5, 2, 4, 6, 10, 15, 20) for each specified value of κ. The simulations show that the function A can be rewritten as:

$$A(R_s/R_c, \kappa) = A_1(\kappa)\ln\left(\frac{R_s}{R_c}\right) + A_2(\kappa) \tag{4.31}$$

where $A_1(\kappa)$ and $A_2(\kappa)$ are functions determined after comparing the functional $A(R_s/R_c, \kappa)$ across all values of κ. Similarly, the equation for the functional expression m, at a given value of κ, is described by:

$$m(R_s/R_c, \kappa) = m_1(\kappa)\ln\left(\frac{R_s}{R_c}\right) + m_2(\kappa) \tag{4.32}$$

Likewise, $m_1(\kappa)$ and $m_2(\kappa)$ are functions determined following a comparison of the functional $m(R_s/R_c, \kappa)$ across all values of κ.

As shown in Figure 4.8, the parameters A_1 and m_1 can be approximated as constant values across κ. The functions A_2 and m_2, however, show some dependence

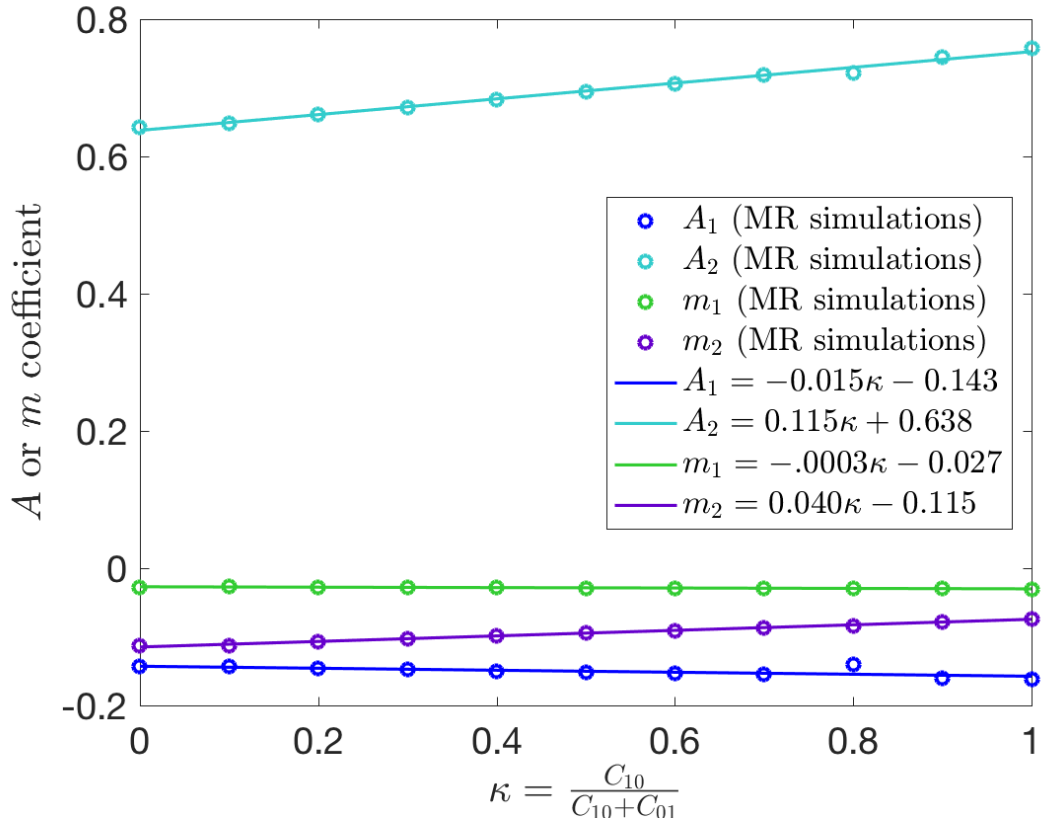

Figure 4.8: Plot of Γ_{MR} coefficients as functions of κ found in simulations (circles) and the corresponding fitted linear functions (solid lines). The R^2 values, or coefficients of determination, are 0.50, 0.99, 0.81, and 0.99 for A_1, A_2, m_1, and m_2, respectively.

on κ, and can be described with the linear functions:

$$A_2 = .117806\kappa + .635907 \tag{4.33}$$

$$m_2 = .0417\kappa - .1159 \tag{4.34}$$

The generalized form for the Mooney Rivlin corrective function is now given by:

$$\Gamma_{MR} = \left[A_1 \ln(\frac{R_s}{R_c}) + A_2(\kappa)\right] \left(\frac{\delta}{R_s}\right)^{m_1 \ln(\frac{R_s}{R_c}) + m_2(\kappa)} \tag{4.35}$$

Table 4.2: Summary of coefficients for the generalized corrective functions of Equation 4.28 (NeoHookean Model) and Equation 5.1 (Mooney Rivlin model)

	NH coefficient values	MR coefficient values
A_1	-0.162	-0.143
A_2	0.756	$0.115\kappa + 0.638$
m_1	-0.031	-0.027
m_2	-0.074	$0.040\kappa - 0.115$

A summary of the calculated parameters for the Mooney Rivlin corrective function is given in Table 4.2. In theory, the calculated model parameters for $\kappa = 1$ (the parameter $C_{01} = 0$) should be identical to the parameters found with the neo-Hookean form. One can see that while the coefficients for A_2 and m_2 show excellent agreement between the neo-Hookean and Mooney Rivlin forms (when $\kappa = 1$), the coefficients A_1 and m_1 are slightly different. This is most likely due to the fact that the linear functions that describe A_1 and m_1 have a poorer fit to the data ($R^2 = 0.50$ and 0.81, respectively) in comparison to the functions describing A_2 and m_2 ($R^2 > 0.99$). Note

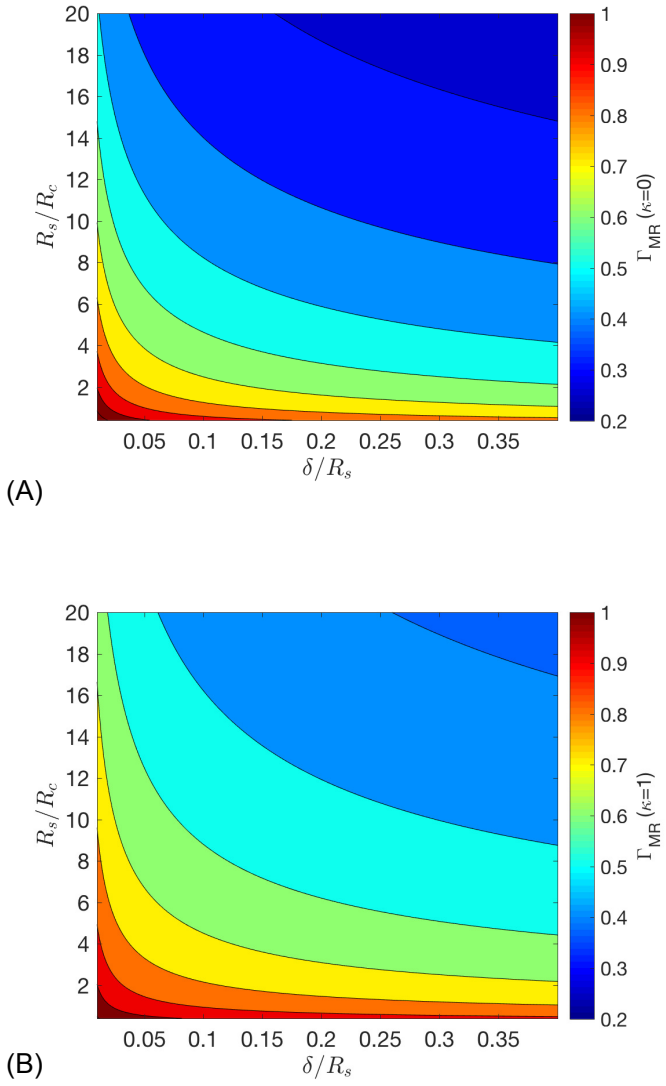

Figure 4.9: (A) Contour plot of corrective function Γ_{MR} over the nondimensional variables (R_s/R_c and δ/R_s) for $\kappa = 0.1$. (B) Γ_{MR} over the nondimensional variables (R_s/R_c and δ/R_s) for $\kappa = 1$. Both contour plots show Equation 5.1 with the coefficients specified in Table 1.

that Equation 5.1 can be further simplified by approximating $m_1 = 0$, although m_1 remains included in the assessment for accuracy.

From the corrective function, we see that $\Gamma_{MR} \propto \delta^{-0.027 \ln \frac{R_s}{R_c} + (.040\kappa - .115)}$. It follows that

$$F_{MR} \propto \delta^{3/2} \delta^{0.027 \ln \frac{R_s}{R_c} - 0.040\kappa + 0.115}. \tag{4.36}$$

Therefore, our nonlinear solution deviates from linear elastic theory ($F^{LE}_{ellip} \propto \delta^{3/2}$) by increasing the indentation power term. For the range of R_s/R_c examined in this study, the additional indentation power term varies from 0.053 ($R_s/R_c = 0.4$, $\kappa = 1$) to 0.1772 ($R_s/R_c = 20$, $\kappa = 0$). Consequently, the force (F_{MR}) is proportional to the indentation within the range of $\delta^{1.55}$ to $\delta^{1.68}$.

Comparison of corrective functions

Smaller values of Γ_{MR} (i.e., $\Gamma_{MR} << 1$) indicate stronger deviation from the linear elastic elliptical contact theory. Figure 4.9 shows contour plots of the corrective functions for Γ_{MR} against the non-dimensional variables of size ratio (R_s/R_c) and indentation ratio (δ/R_s) for the two extreme cases: $\kappa = 0$ (Fig. 4.9 A) and $\kappa = 1$ (Fig. 4.9 B). For values of small R_s/R_c and δ/R_s, the corrective function approaches a value of 1 ($\Gamma_{MR} \approx 1$), and linear elasticity theory may be used. For a given set of δ/R_s and R_s/R_c, a comparison between Figure 4.9A and B shows that when $\kappa = 0$, Γ_{MR} is smaller (Γ_{MR} deviates farther from 1). Therefore the material demonstrates an increase in nonlinear behavior. As expected, the corrective function deviates farthest

from linear elasticity ($\Gamma_{MR} = .025$) when $\kappa = 0$, R_s/R_c is large, and δ/R_s is large.

One can see the most variation in Γ_{MR} across R_s/R_c. For a given value of R_s/R_c the corrective function changes slowly with respect to the extent of indentation δ/R_s. This is explained by the fact that m_1 and m_2 are small across all values of κ, and therefore Eqn, 5.1 will demonstrate greater dependence on R_s/R_c.

4.3 Discussion

Effects of large deformations and accuracy of corrective functions

In this section we discuss the accuracy of our corrective functions. For incompressible thin specimens under large deformation (large values of indentation strain, δ/R_c), the specimen experiences restricted deformation in the direction of applied loading, and will therefore experience more expansion along the sides and length of the cylinder. In the previous section, all simulations for computing Γ_{MR} utilized an indentation strain of 0.14, however, in this section we extend the analysis to larger indentation strains ($\delta/R_c > 0.30$) to assess the accuracy of our solution.

Figure 4.10A shows the force-displacement curves calculated with the proposed corrective functions (Equation 5.1) in comparison to additional finite element simulations performed at a larger indentation depth. A plot of the corresponding sum-

of-squares error (SSE) is shown in Figure 4.10B (SSE values are given by $SSE = \Sigma(\widehat{y} - y)^2$, where $\widehat{y}$ are the forces obtained through the new simulations, and y are the force values calculated using the corrective function of Eqn. 5.1). One can see that for smaller values of R_s/R_c, the corrective function provides an excellent fit ($SSE < 0.25$) up until $\delta/R_c = 0.45$. For larger ratios of R_s/R_c, the corrective function only seems suitable for indentation strains less than 0.25, after which the SSE values exceed 0.25.

As expected, the theoretical curves from linear elastic theory ('+' curves) show a much larger error. For $R_s/R_c = 1$, the linear elastic theory provides a reasonable estimate for $\delta/R_c < 0.28$. For $R_s/R_c = 20$ the linear elastic theory of elliptical contact shows significant errors ($SSE > 0.25$) for $\delta/R_c < 0.08$.

4.3.1 Substrate effects

As mentioned in the preceding section, one way in which substrate interactions affect the solution is by restriction of deformation along the direction of loading. Another way in which the substrate interactions affect the solution is by modifying the boundary conditions between the specimen and substrate. For the ease of creating a symmetric model (Figure 4.1C), we chose to use a boundary condition that allows the specimen to slip along the longitudinal direction, while being restricted in the direction normal to the loading (i.e., "non-adhered" boundary condition). Alternatively, one could also examine the effects of a "fully adhered" boundary condition, which is

expected to to behave differently than the "non-adhered" boundary condition at large values of δ/R_c. In reality, the boundary condition between a cell and its substrate is not entirely fully adhered or entirely non-adhered. As described by Mahaffey et al. 2004, cell membranes will often have a higher abundance of focal adhesion sites around the edges. A combination of full-adhesion and no-adhesion modeling can be used to obtain material properties for different regions of the cell [183].

4.3.2 Regimes for R_s/R_c

The correction factors provided in this study were found using computational models with R_s/R_c between 0.4 and 20. This range of R_s/R_c was sufficient to encompass the lower bound of elliptic contact (rigid spherical indenter on a deformable half-space specimen) and the upper bound of elliptic contact (rigid half-space indenter on a deformable cylinder). The lower bound of elliptic contact becomes a circular contact area, while the upper bound becomes a rectangular/line contact area. As mentioned previously, for values of $R_s/R_c < 0.4$, the cylindrical specimen is relatively "flat", and the conventional formulations for circular contact areas (spherical indentation on a half-space) can be utilized. Previous works have also considered the effects of large indentation and substrate interaction for spherical indentation on a half-space. For a spherical indentation on a flat cellular specimen ($R_s/R_c < 0.4$) of finite thickness h ($h \geq 0.1R_s$), one can use the analytical expressions provided by Dimitriadis [145]. However, they assume linearity, and the result is meant for small

indentations ($\delta \leq 0.1h$). For very thin flat specimens ($R_s/R_c < 0.4$, $h \leq 0.1R_s$), an analytical expression is provided by Chadwick [184].

Here, we do not specify a theoretical upper bound for R_s/R_c, although $R_s/R_c = 20$ is the maximum value used in fitting the expression of the corrective function. For very large values of R_s/R_c, the behavior is expected to approach the theoretical limit for the indentation of a half-space on a cylinder. This is also equivalent to the case of two parallel cylinders in contact (although with one cylinder having a radius that tends to infinity). The two parallel cylinders brought into contact will result in a rectangular contact area. Precise equations for the contact between two cylinders are provided in previous works [165] [181] (although a major drawback of these models is that the contact force cannot be explicitly defined as a function of indentation in closed form [185]). The indentation depth for a rigid half space with a linear elastic cylinder of length L is given by [181] :

$$\delta = \frac{F}{\pi L E^*}\left(1 + \ln\frac{\pi E^* L^3}{R_{cyl} F}\right), \tag{4.37}$$

assuming that the half-space is rigid, $\frac{1}{E^*} = \frac{1-\nu^2}{E}$. Equation 4.37 is plotted in Figure 4.10A (circles). It is observed that the theoretical force-displacement curve for the elliptical contact of $R_s/R_c = 20$ is very close to the upper bound where R_s approaches infinity (i.e., rigid half-space indenter), indicating that the range of R_s/R_c values we selected for our computational studies is sufficient for capturing both the lower and upper bounds of ellipticity.

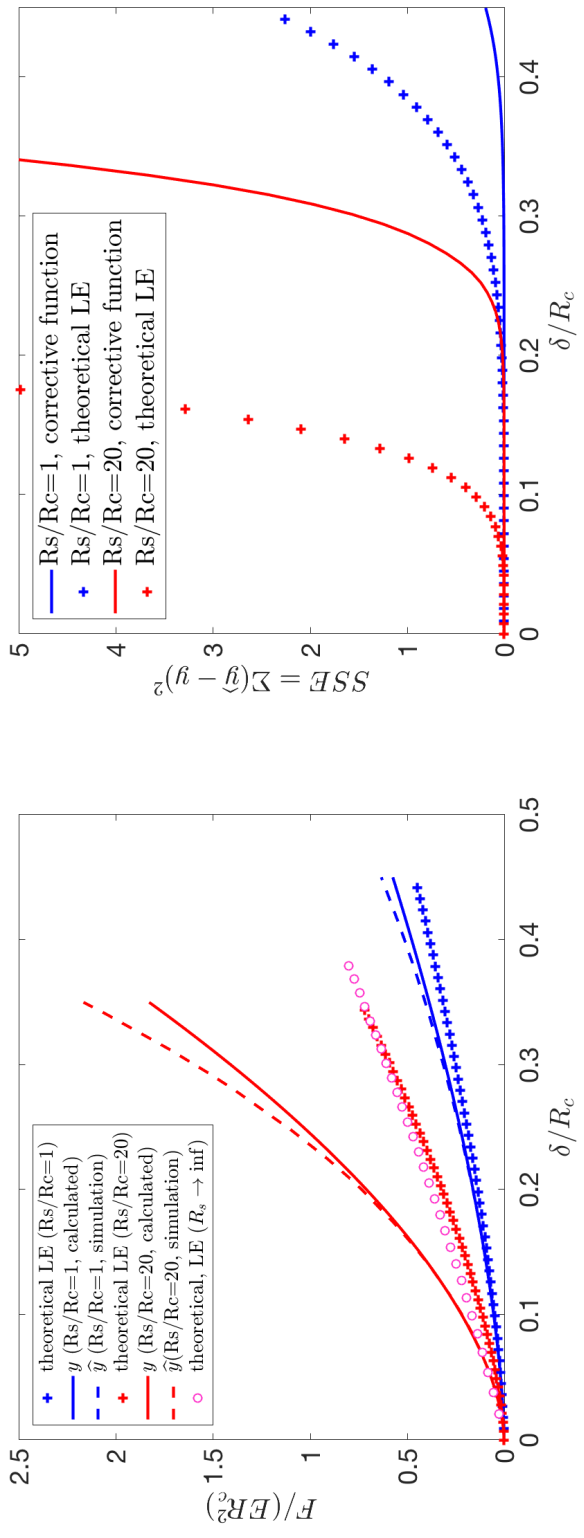

Figure 4.10: (A)Plot of normalized force over the non-dimensional variables (δ/R_c) for the case of $R_s/R_c = 1$ (blue) and $R_s/R_c = 20$. Simulations performed over large indentations (dashed lines) are compared to force-displacement curves calculated with the correction functions ($\kappa = 1$) found in this study (solid lines) and linear elastic theory ('+' lines). The approximation to the indentation of a cylinder by a half-space is also shown for comparison (circles). (B) Plot of the sum of squared errors for the correction functions found in this study (solid lines) and compared to linear elastic elliptical contact theory ('+' lines).

4.3.3 Limitations and future considerations

This study examined two simple and well-known hyperelastic (neo-Hookean and the Mooney-Rivlin) models, although these are not the only possibilities for hyperelastic strain energy functions. More sophisticated material models, however, might require more material parameters, and could result in more complex corrective functions.

For values of R_s/R_c less than 0.4, one can expect $\Gamma_{MR} \approx 1$ for fairly large indentation depths (until $\delta/R_c = 0.45$). For larger size ratios ($R_s/R_c > 20$), the correction factors are precise until values of $\delta/R_c > 0.25$. Errors at larger indentation depths should be considered, as discussed in the previous section. Large values of δ/R_c could also result in large errors when applying the model to experimental data where the observed interaction between the specimen and substrate is fully adhered.

4.3.4 Potential applications

In order to obtain the hyperelastic material properties from the experimental data, one could use the following procedure:

1. Multiply the experimental data (F_{exp}) by the corrective function for the neo-Hookean model ($F_{exp}\Gamma_{NH}$).

2. Set $F_{exp}\Gamma_{NH} = \frac{2\pi}{3}\frac{4C_{10}(1+\nu)}{1-\nu^2}\sqrt{2R}\delta^{3/2}k\overline{\mathcal{F}}^{-3/2}\overline{\mathcal{E}}^{1/2}$

   where,

$$\Gamma_{NH} = \left[A_1 \ln(\tfrac{R_s}{R_c}) + A_2\right]\left(\tfrac{\delta}{R_s}\right)^{m_1 \ln(\frac{R_s}{R_c})+m_2}$$

$\nu = 0.5$, and the constants are given by: $A_1 = -0.162$, $A_2 = 0.756$, $m_1 = -0.031$, and $m_2 = -0.074$.

3. Calculating k, $\overline{\mathcal{F}}$, and $\overline{\mathcal{E}}$ with the known dimensions of R_s and R_c, and assuming $\nu = 0.5$, use the preceding expression to obtain C_{10}.

An equivalent result can also be obtained by using Γ_{MR} (setting $\kappa = 1$) instead of Γ_{NH}. Once C_{10} is obtained, one can use Γ_{MR} and find an appropriate value for κ by numerically solving for the minimization of squared errors between the estimated F_{MR} curves and the experimental results. Therefore, an initial value of C_{10} should be determined first, otherwise, κ cannot be uniquely determined [186].

The formulations provided in this study can be applied to several cylindrical-shaped specimens that appear in biological materials. In Fig. 4.1 we showed an example of spherical indentation on a neuronal axon (cylinders with diameters on the order of a few microns). In addition to axons, the vast majority of brain cells contain cylindrical-like morphologies in their processes (glial cell processes, neurites, dendrites, etc.).

Examples of other cells that exhibit a stellate-like morphology (i.e., have processes) include osteocytes, mesenchymal stem cells, pericytes, and fibroblasts. Due to the heterogeneity of the mechanical properties of cells, it is important to obtain properties with respect to specific cellular compartments [47] [187] (and not just measuring the

response of the spherical somal body with classical Hertz formulations). Aside from probing fibrous cellular components, other uses of this work include probing other types of cylindrical-shaped biological specimens such as certain strains of bacteria (i.e., bacilli), as well as fibrous materials of the extracellular matrix (such as fibrin, collagen, and elastin). With respect to non-biological applications, this work can be applied to measuring hyperelastic properties of cylindrical synthetic polymer fibers and natural fibers that can be used in fiber-reinforced composites (provided that they can be approximated as incompressible).

4.4 Conclusions

Our approach provides a generalized formulation that can be used to extract mechanical properties from indentation into soft cylindrical bodies. The generalized corrective function Γ_{MR} of Equation 5.1 with the corresponding coefficients of Table 4.2 can be applied to force-displacement relationships for cylindrical incompressible hyperelastic materials subjected to spherical indentation. These corrective functions are valid for a wide range of specimen and indenter sizes: with small values of R_s/R_c approaching the limit of a flat specimen subjected to spherical indentation, and large values of R_s/Rc approaching the limit of a flat indenter with a cylindrical specimen. For large values of R_s/R_c and large indentations (δ/R_s), the force-displacement behavior deviates farther from linear elastic elliptical contact theory.

Although the motivation of this study was to provide a theoretical framework for obtaining useful mechanical properties of cylindrical cellular bodies subjected to large indentation and deformation, the results can be applied to experimental data of non-cellular soft specimens (collagen, fibrin, biomimetic polymer strands, etc.) where a hyperelastic model is also required. Given the availability of indentation experiments over various length scales, the corrective functions provided in this study are a promising tool for measuring the hyperelastic properties of soft materials in a wide range of applications.

Chapter 5

Mechanical properties of glial cells

5.1 Introduction

Using the indentation formulations presented in Chapter 4, the experimental techniques presented in Chapter 3 provide the necessary measured forces and indentations which can be used to obtain the hyperelastic mechanical properties of cells. Due to the soft nature of the glial cells, this can result in large strains. If we define the *indentation strain* as the indent depth over the specimen radius, the preceding section demonstrates that although the linear elastic approximation can be surprisingly accurate up until $\delta/R_c = 0.25$ for large cells, the linear elastic approximation is inaccurate as early as $\delta/R_c > 0.05$ for smaller cells ($R_s/R_c = 20$).

Since the majority of the specimens probed in our experiments are small cellular process ($R_c < 2.5\mu$m) subjected to large indentations strains, it is necessary to

consider the hyperelastic correction factors presented in Chapter 4. There is a lack of experimental characterization of hyperelastic properties of brain cells in literature. Nonlinear material properties obtained in this way are useful for implementation into future computational models of brain tissue, especially in the case of TBI models, where the cells are subjected to large deformations that exceed normal physiological conditions.

5.2 Data analysis

5.2.1 Force-displacement curves

We start with the example of the raw data curves shown in Section 3.3.2, where the specimen stage was translated in the y-direction towards the cell. A schematic of the experimental setup and corresponding coordinate systems is shown in Fig. 5.1. The raw data from all experiments (strain gauge readings, QPD readings, and images of the cell specimens) can be accessed from the HEMI Craedl website. Plots of the processed indentation history and force histories obtained from the raw data curves of Fig. 3.6 in Section 3.3.2 are shown in Fig. 5.2A,B.

Indentation was calculated as $\delta = \Delta\psi - \Delta d$, where $\Delta\psi$ is the scaffold translation, and Δd is the bead deflection measured from the QPD sensor. The indentation history (δ) was plotted for ($t > 0$), where $t = 0$ was determined as the time at which the indentation velocity ($\dot{\delta}$) reached a maximum value. The initial "jump" from the

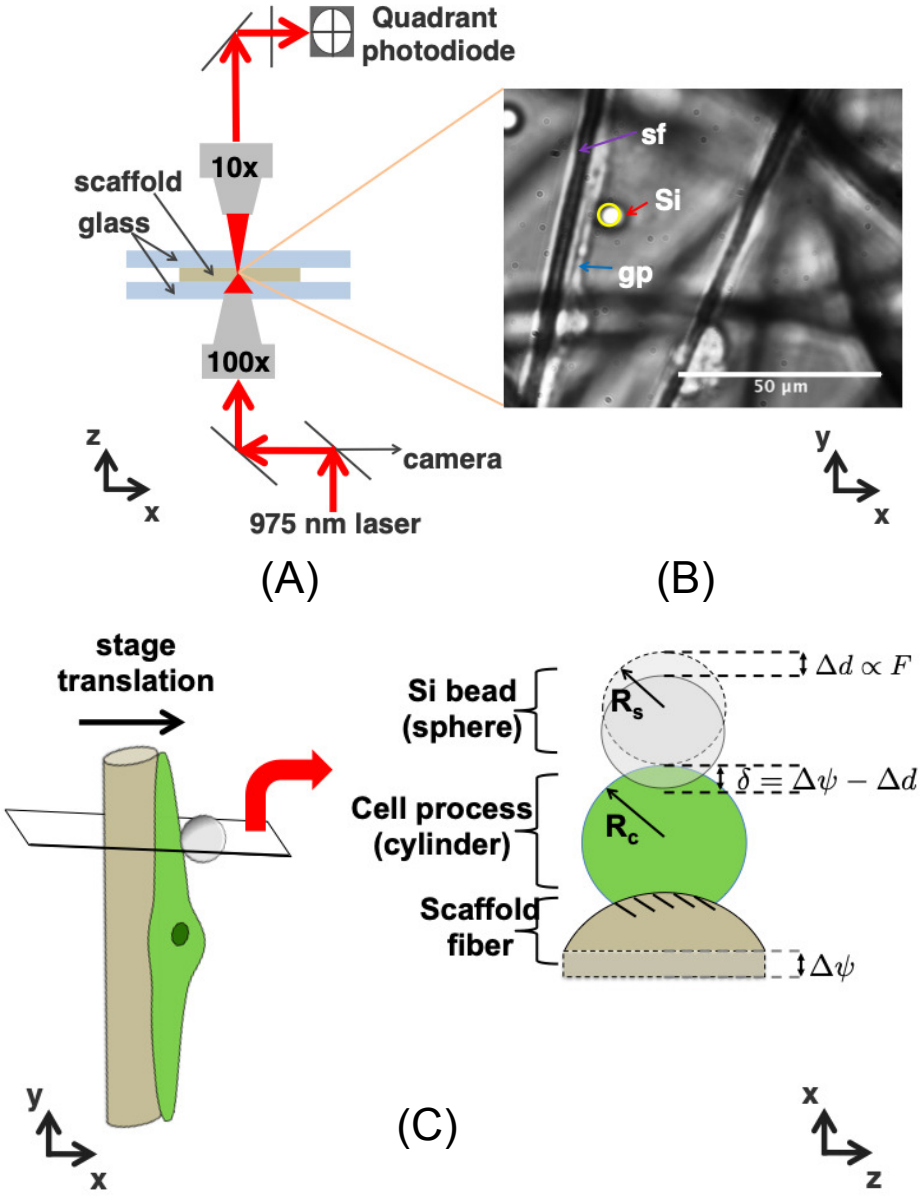

Figure 5.1: (A)Specimens are clamped into a translational piezoelectric stage at the focal point of the trapping laser. A quadrant photodiode at the back-focal plane is used to detect deflection of the 975 nm laser, thereby providing X,Y, and Z changes of bead displacement. (B) Example image of glial process (gp) grown along a scaffold fiber (sf). An optically trapped streptavidin-coated silica bead (Si) is brought into contact with the biotinylated surface of the cell. (C) The specimen stage is translated in the direction perpendicular to the fiber (+x direction in the example shown). The cross-sectional view depicts the scaffold translation ($\Delta\psi$), measured bead deflection (Δd), and cell indentation ($\delta = \Delta\psi - \Delta d$). The bead deflection ($\Delta d$) is related to force through prior calibration of the OT.

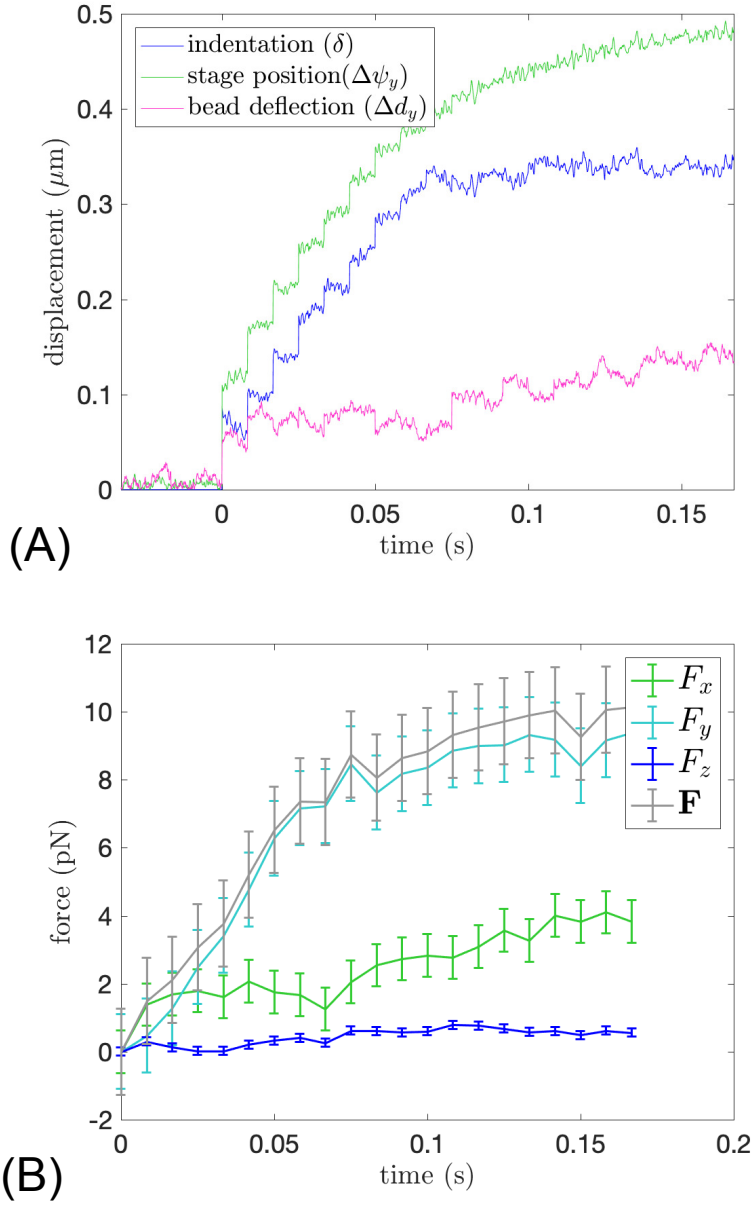

Figure 5.2: (A) Measured displacement of the specimen stage ($\Delta\psi_y$) over time and the computed indentation ($\delta = \Delta\psi_y - \Delta d_y$) over time. (B) Force components and magnitude measured by bead deflection ($F_i = k_i \Delta d_i$) over time. Error bars are plotted at increments of every 100 data points for clarity.

actuator stage ($\Delta\psi_y$ shown in Fig. 5.2A) corresponds to an initial rapid movement of the actuator followed by a slower approach to the final stage position. Consequently, this results in a "jump" in the bead displacement and indentation histories.

The force components in the x-, y-, and z- directions were calculated as $F_i = k_i \Delta d_i$ (i=x, y, z), where the trap stiffness k_i was calibrated to be $k_x = 34.9$ pN/μm, $k_y = 34.2$ pN/μm, and $k_z = 24.1$pN/μm, as discussed in Section 3.3.3. A moving average differentiation was performed on the raw QPD data over a window of 2.5 ms in order to improve clarity of the force data. Figure 5.2B shows the corresponding force history calculated from the bead deflection. Error bars were calculated from the uncertainty in bead deflection in the x-, y-, and z-directions, as described previously in Section 3.4.1. The ratio of tangential to force magnitude ($F_z/\mathbf{F}$) was calculated across all time points to verify that the indenter bead was adequately aligned with the cellular specimen along the z-axis . Any experiment with an average ratio of $F_z/\mathbf{F}$ exceeding 0.41 (see Section 3.5.1) was not used for further analysis.

The final force-displacement relationship is plotted in Fig. 5.3. Note that the data appears discontinuous over δ, which is due to the fact that the actuator stage produces small jumps in displacement, as was shown in Fig. 5.2A. There are two sources of error which are overlaid on Fig. 5.3: error from random fluctuations in the bead position, and the error from the stiffness calibration of the trap. The trap stiffness values k_x, k_y, and k_z had an uncertainty of 3.75, 3.85, and 3.81 pN/μm, respectively. The calculated errors from the random fluctuations in bead position

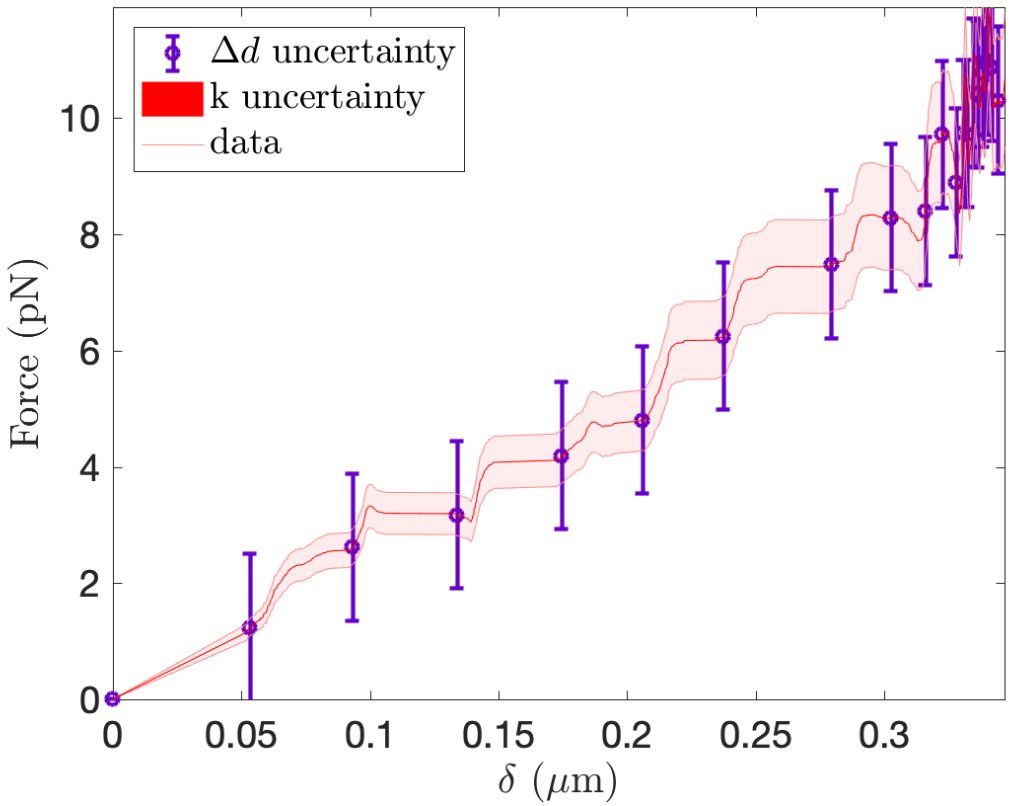

Figure 5.3: Comparison of errors due to trap stiffness uncertainty (shaded red) versus uncertainty in bead position (purple error bars). For clarity, error bars for bead displacement (Δd) are plotted at increments of every 100 and 25 data points.

measurements dominate any uncertainty in trap stiffness. At larger indent depths, the uncertainty of trap stiffness generates significant errors, but these errors remain slightly less than the errors generated by bead position uncertainty.

In Fig. 5.3 there is a higher density of data points near the maximum indentation depth (δ_{max}). This is the result of the actuator moving the specimen with an initial "jump" followed by slower approach to its final position. Thus a constant sampling rate generates a different density in data points based on different indentation velocities, which will be discussed more in depth in the following section.

5.2.2 Parameter fitting

As discussed in Chapter 3, the determination of the initial contact point is important for characterization of the force-displacement relationship [145]. Therefore, to ensure that the initial contact point is known, we utilized streptavidin-coated silica beads that could adhere to biotinylated cell membrane surfaces. This allows us to specify that the bead is in contact with the cell membrane when $\delta = 0$.

The strain rate was calculated using the conventional definition of indentation velocity over indentation depth ($\dot{\epsilon} = \dot{\delta}/\delta$) [188]. Across all experiments, an initial "jump" in the displacement of the piezo stage resulted in a high apparent initial strain rate, while the slower approach to the final position resulted in a slower strain rate (Fig. 5.4A,B). The initial and strongly varying high strain rate regime ($\dot{\epsilon}_1 \approx 50-400s^{-1}$) is substantially larger than the later low strain rate regime ($\dot{\epsilon}_2 \approx 2-40s^{-1}$)

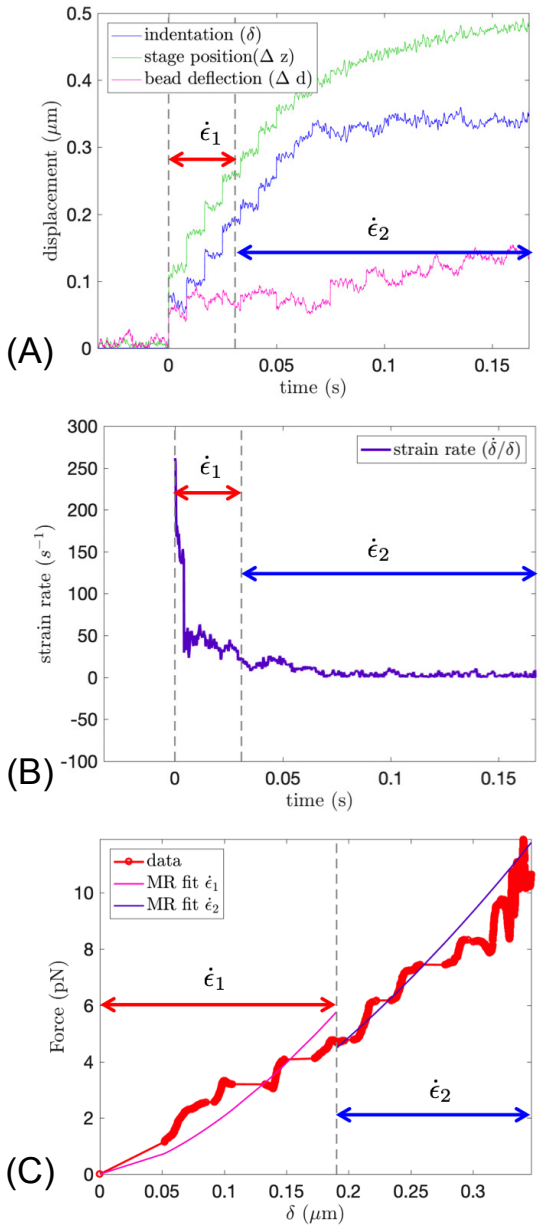

Figure 5.4: Depiction of force-displacement relationship obtained from a single experiment. (A)The piezo stage initially jumps (green line) to a large displacement during $\dot{\epsilon}_1$ resulting in a large jump in indentation depth (blue line). The piezo stage then slows down to its final position during $\dot{\epsilon}_2$. (B) The average initial strain rate ($\dot{\epsilon}_1$) is at least one order of magnitude larger than the second strain rate ($\dot{\epsilon}_1$). The time at which the strain rate transitions from high ($> 100s^{-1}$) to low ($< 10s^{-1}$) is calculated for each test. Strain rate is defined as $\dot{\delta}/\delta$. (C) The displacement at which the strain rate transitions is found (vertical dashed gray line) so that a hyperelastic force-displacement curve is fit to each strain rate regime.

as shown in in Fig. 5.4B. The desired material properties can be fitted separately for the two strain rate regimes (denoted as $\dot{\epsilon}_1$ and $\dot{\epsilon}_2$ in Fig. 5.4A-C). The second strain rate regime has an essentially constant strain rate and thus provides a better measure of material behavior. The end of the first strain rate regime was defined at the first point in time where the instantaneous strain rate dropped below $20s^{-1}$.

Although details of the hyperelastic indentation formulae are described in Chapter 4, a brief version is provided below for convenience. The corrective function for indentation of a Mooney Rivlin material (Γ_{MR}) was found to be :

$$\Gamma_{MR} = \left[A_1 \ln(\frac{R_s}{R_c}) + A_2(\kappa)\right] \left(\frac{\delta}{R_s}\right)^{m_1 \ln(\frac{R_s}{R_c}) + m_2(\kappa)} \tag{5.1}$$

where

$$A_1 = -0.143$$

$$A_2 = 0.115\kappa + 0.638$$

$$m_1 = -0.027$$

$$m_2 = 0.040\kappa - 0.115$$

Note that κ is a non-dimensional ratio of the hyperelastic constants:

$$\kappa = \frac{C_{10}}{C_{10} + C_{01}} \tag{5.2}$$

The final force-displacement for indentation of a hyperelastic cylinder is then given by:

$$F_{MR} = \frac{F_{ellip}}{\Gamma_{MR}} \tag{5.3}$$

Where F_{ellip} is the force for a linear elastic material under elliptical contact given by:

$$F_{ellip} = \frac{2\pi}{3}(2R)^{1/2}\frac{4C_{10}(1+\nu)}{1-\nu^2}\delta^{3/2}\chi_{ellip} \tag{5.4}$$

In the above expression, the Young's modulus E of Equation 5.4 has been replaced by $4C_{10}(1+\nu)$. χ_{ellip} is a product which is solely dependent on the ratio between the indenter radius R_s and the cylinder radius R_c, and can be approximated by an algebraic expression found in previous work [179, 180] and is provided in Equation 4.14.

Note that although we are less interested in the Young's modulus due to its limitation to small strains, our hyperelastic formulation is essentially a correction factor to the linear elastic formulation, as shown in Equation 5.3. The ratio of our indenter tip (R_s) to cell process radius (R_c) varied from 0.85 to 14.83 across all experiments (well within the appropriate range of R_s/R_c examined in Chapter 4).

Since we are considering short time scales, we approximated the cell as an incompressible material ($\nu = 0.5$). For each of the two strain rate regimes of our experiment, the force-displacement curves are fit to a Mooney Rivlin model by minimizing the squared error between the theoretical curve and data in the following steps:

1. An initial guess for the hyperelastic constant (C_{10}^0) is defined based on the maximum force and displacements observed.

2. A range of possible constants ($C_{10} \in [0.5C_{10}^0, 1.5C_{10}^0]$) is specified.

3. Setting $\kappa = 1$ (first enforcing the neo-Hookean case), the theoretical curves for F_{ellip} and F_{MR} were calculated with the range of C_{10} across all indentation depths ($\delta \in [0, \delta_{max}]$).

4. The root-mean-square errors between the experimental data and the theoretical F_{MR} curves found in the previous step were calculated. The theoretical curve with the smallest RMSE across the range of δ within the strain rate regime is the best fit approximation for C_{10}.

5. The range of $\kappa \in [0, 1]$ is used to calculate F_{MR} using the fitted C_{10} value

6. Again, the minimum RMSE between the theoretical F_{MR} curves and the experimental data is calculated across the range of δ within the strain rate regime. The theoretical curve with the smallest RMSE at δ_{max} is the best fit approximation for κ.

7. The second Mooney Rivlin parameter (C_{01}) was found from: $C_{01} = \frac{C_{10}}{\kappa} - C_{10}$

To quantify how well our hyperelastic parameters fit the experimental force-displacement data, the RMSE values from Steps 4 and 7 were normalized by the maximum force found in each experiment. The normalized RMSE between the experimental and theoretical curves was greater during the higher strain rates. It should also be noted that the range of δ_{max}/R_c observed in our experiments varied from $R_s/R_c \in 0.083, 0.86$. In the cases of large δ_{max}/R_c, the hyperelastic formulae are less

accurate (especially in the case of smaller cells). For $R_s/R_c = 1$, the hyperelastic formulae are only accurate until $\delta/R_c = 0.45$ (as discussed in Chapter 4).

5.3 Strain rate and indentation velocity effects

5.3.1 Effect of strain rate

Fig. 5.5A and B show the parameters C_{10} and κ as a function of strain rate for both strain rate regimes. Since the strain rates vary within the strain rate regime, the reported strain rate values in Fig. 5.5 were computed as the mean value of strain rate within their respective time intervals. At the high strain rate regime ($\dot{\epsilon_1}$), the strain rate varies significantly, and therefore the reported strain rate values are less meaningful. For this reason, plots showing the parameters as a function of rate in the second strain rate regime ($\dot{\epsilon_2}$) is shown in more detail in Fig. 5.6.

A paired-sample two-tailed t-test was performed on the values of C_{01} and κ between the high and low strain rate (Fig. 5.5A,B). It was found that both C_{01} and κ were significantly higher at high strain rates (p-value$<<$ .05). Larger deviations are found for both C_{01} and κ during the high strain rate regime, although this could be attributed to variations between specimens at the membrane surface since $\dot{\epsilon_1}$ probes the smaller indentation depths. Note that since $\kappa = 1$ corresponds to a neo-Hookean

model, the higher values of κ correspond to a response that is more similar to a linear elastic material.

Taking a closer look at the parameters within the second strain rate regime (Fig. 5.6), it is again evident that C_{10} and κ increase at higher strain rates ($\dot{\epsilon} > 10s^{-1}$). When comparing the lowest strain rates ($< 10s^{-1}$) to the higher strain rates ($> 30s^{-1}$), the stiffness C_{10} increases approximately by a factor of 2. A one-tailed t-test showed that C_{10} is significantly lower for $\dot{\epsilon} < 10s^{-1}$ (p-value=0.041). A stiffer cellular response is expected at higher strain rates, which will be discussed more in Section 5.6. At lower strain rates, κ was also significantly lower (t-test, p-value=0.045).

A summary of the material properties for various strain rates is shown in Table 5.3.1. It should be noted that for strain rates $> 40s^{-1}$ (comprised of the $\dot{\epsilon_1}$ regime), all of the strain rates were grouped into a single wide range (40-360 s^{-1}) since the strain rates were nonuniform with large deviations during the first strain rate regime. Therefore, the large standard deviation from the mean values in the range of 40-360 s^{-1} is mostly attributed to the fact that it is a comprised of a wide range of strain rates.

5.3.2 Maximum forces and indentation depth

Figure 5.7 shows that the majority of the tests (with the exception of a single outlier) were well below the maximum holding force of the OT of 22.1 pN. No linear correlation was found between F_{max} and δ_{max} (p-value=0.698). Since the maximum

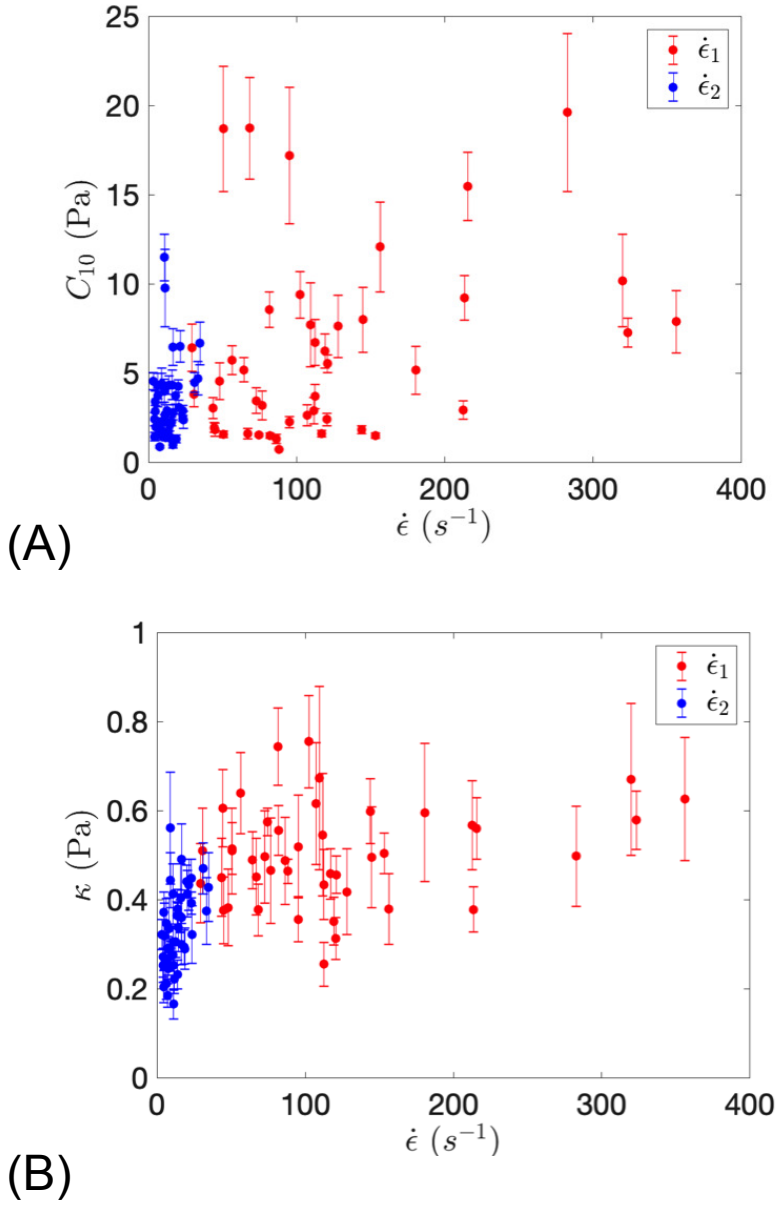

Figure 5.5: Comparison of the fitted hyperelastic constants to the strain rates within the second strain rate regime ($\dot{\epsilon_2}$). (A) Comparison of the obtained material parameter C_{10} across the varying calculated strain rates. (B) Comparison of the parameter κ across the varying calculated strain rates (n=44 for each plot).

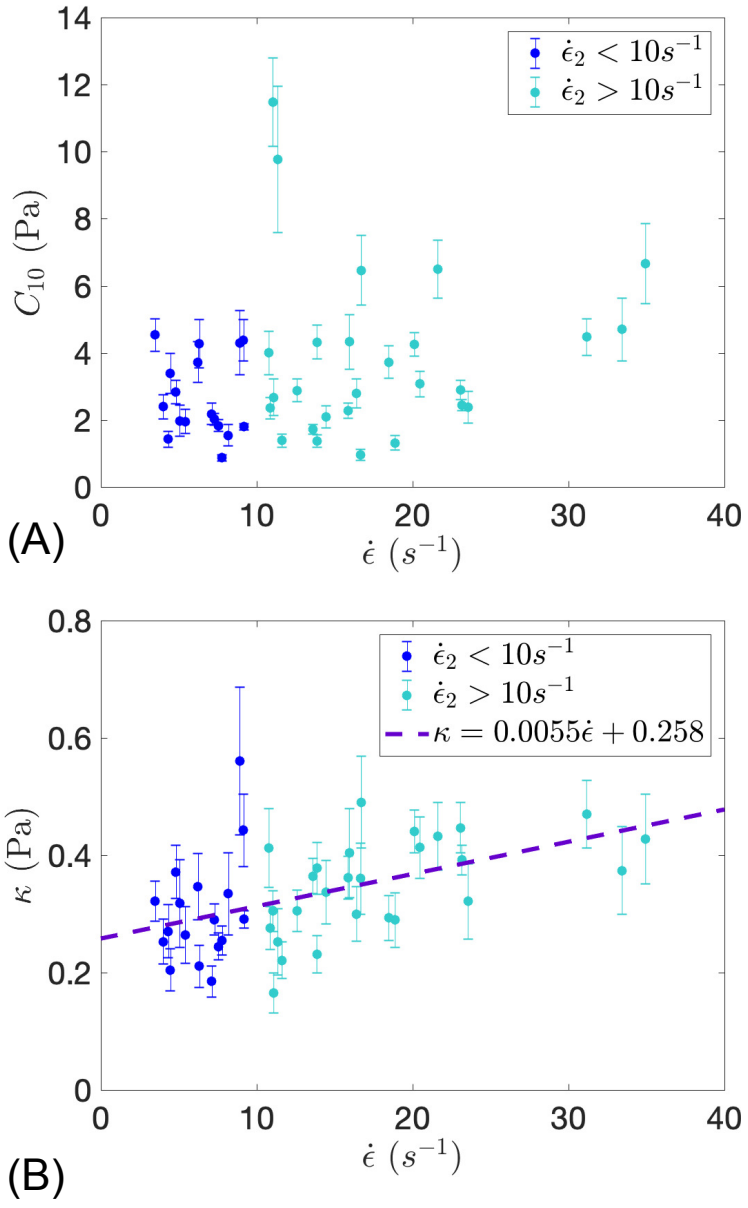

Figure 5.6: Comparison of the fitted hyperelastic constants to the strain rates examined within the second strain rate regime $\dot{\epsilon_2}$. (A) Comparison of the obtained material parameter C_{10} across the varying calculated strain rates. A linear regression analysis showed that the response could not be fit to a linear fit (p-value$>$ 0.05). However, the higher strain rates $\dot{\epsilon} > 10s^{-1}$ showed a stiffer response (t-test, p-value$=$ 0.041). (B) Comparison of the parameter κ across the varying calculated strain rates showed a linear fit (linear regression, p-value$<<$ 0.05) and statistical significance for higher κ values when $\dot{\epsilon} > 10s^{-1}$ (t-test,p-value$=$ 0.045).

strain rate	mean $C_{10}(Pa)$	mean κ	*E (Pa)	sample size
0-10 s^{-1}	2.7 $\pm$1.2	0.30 $\pm$ 0.09	52.8	n=17
10-40 s^{-1}	3.9 $\pm$2.4	0.36 $\pm$ 0.09	64.3	n=30
40-360 s^{-1}	6.3 $\pm$5.3	0.50 $\pm$ 0.11	74.3	n=41

Table 5.1: Table of hyperelastic material properties with respect to $\dot{\epsilon}$. Results are presented as the mean value with standard deviations. *Elastic moduli values (E) are given by the small strain approximation, $E = 4(1+\nu)(C_{10}+C_{01})$.

indentation depth is limited by the prescribed stage translation, no global conclusions regarding cell stiffness can be drawn by the trends of Fig. 5.7B. However, since it is known that 590 nm is close to the upper limit of maximum bead deflection allowed by the trap, we can see that a 590 nm indentation depth did not necessarily correspond to maximum allowable forces. Therefore, cells were soft enough such that the bead did not deflect to its maximum limit, even though the cellular indentation reached almost to 600 nm depths. Consequently, this ensures that we do not need to worry about losing the trap during the larger stage displacements.

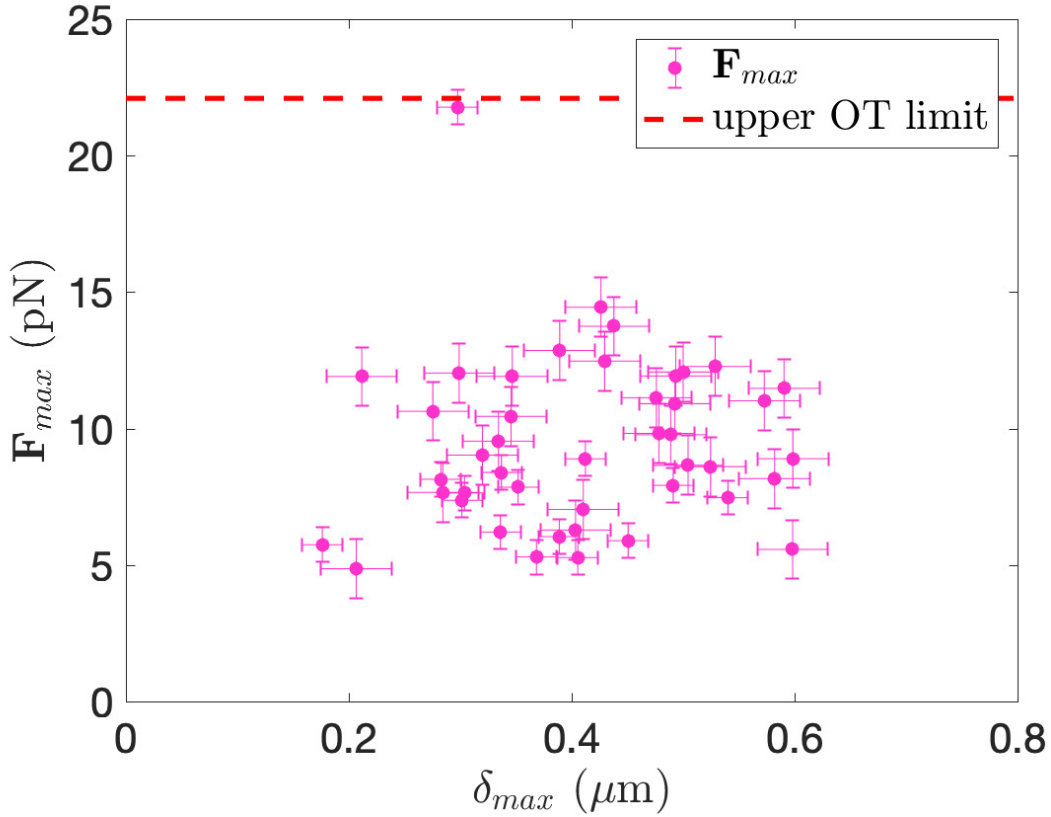

Figure 5.7: No correlation was found between the maximum force and maximum indent depth (p-value> 0.05).However, our our results indicate that the experiments were within the working limits of the optical trap

5.4 Effects of length scales and indentation depth

5.4.1 Effect of cell size on stiffness

Since one motivation of this experimental study is to find possible length scales at which mesoscale models can be homogenized, we began by attempting to correlate the material parameters C_{10} and κ to the observed cell process diameter in each test. We hypothesized that there might be a noticeable increase in stiffness for larger processes since smaller glial cell processes lack certain cytoskeletal components, such as microtubules [11,12]. Across all cell process sizes, we expected that the beginning of the force-indentation curves should behave similarly since shallow indentation depths are mostly probing the cell membrane and actin.

The actin cortex is a specialized actin network localized to a layer just underneath the cell membrane. Although the primary function of the actin cortex is to help regulate migration and morphogenesis [189], it has also been shown to greatly contribute to cell stiffness, especially in the case of indentation testing [46, 190, 191]. Approximately the first 200 nm of indentation is the actin cortex [192]. Larger indentation depths ($>$ 500 nm) would presumably probe the underlying cytoskeletal components. Vargas-Pinto et al. showed with computational modeling that a spherical indenter tip is able to probe a more global response outside of the actin cortex, while sharp

indenter tips are probing the local properties of the actin cortex only [46].

A plot of the calculated material parameter C_{10} against glial process diameter is shown in Fig. 5.8A. The cell process diameter here refers to the total height of the specimen directly underneath the initial contact point of the indenter. Using light microscopy images taken during each experiment, the cell process diameter was measured as the perpendicular distance between the edge of the scaffold fiber and the contact point with the bead. Diameters ranged from about 700 nm to 12 μm. A one-way ANOVA test followed by Bonferroni's multiple comparison test was used to determine the significance (p-value$<<0.05$) between the calculated values of C_{01} and glial process diameter for the higher and lower strain rate regimes (Fig. 5.8B and C). Although we expected to see differences between small cellular processes $< 1\mu$m and larger processes, we found that no groups had means significantly different from each other. The sample size within the groups of $< 1\mu$m, $1-2\mu$m, $2-3\mu$m, and $> 3\mu$m were n=6, n=9, n=18, and n=11, respectively.

5.4.2 Effect of indentation depth on stiffness

In order to understand where heterogeneities due to cytoskeletal constituents might occur along the indentation depth, a statistical comparison was performed between the maximum indent depth locations (δ_{max}) and the material properties. Figure 5.9A-B compares material properties for the higher strain rates ($\dot{\epsilon_1}$, red) and the lower strain rates ($\dot{\epsilon_2}$, blue) with the maximum indentation depth δ_{max}. For

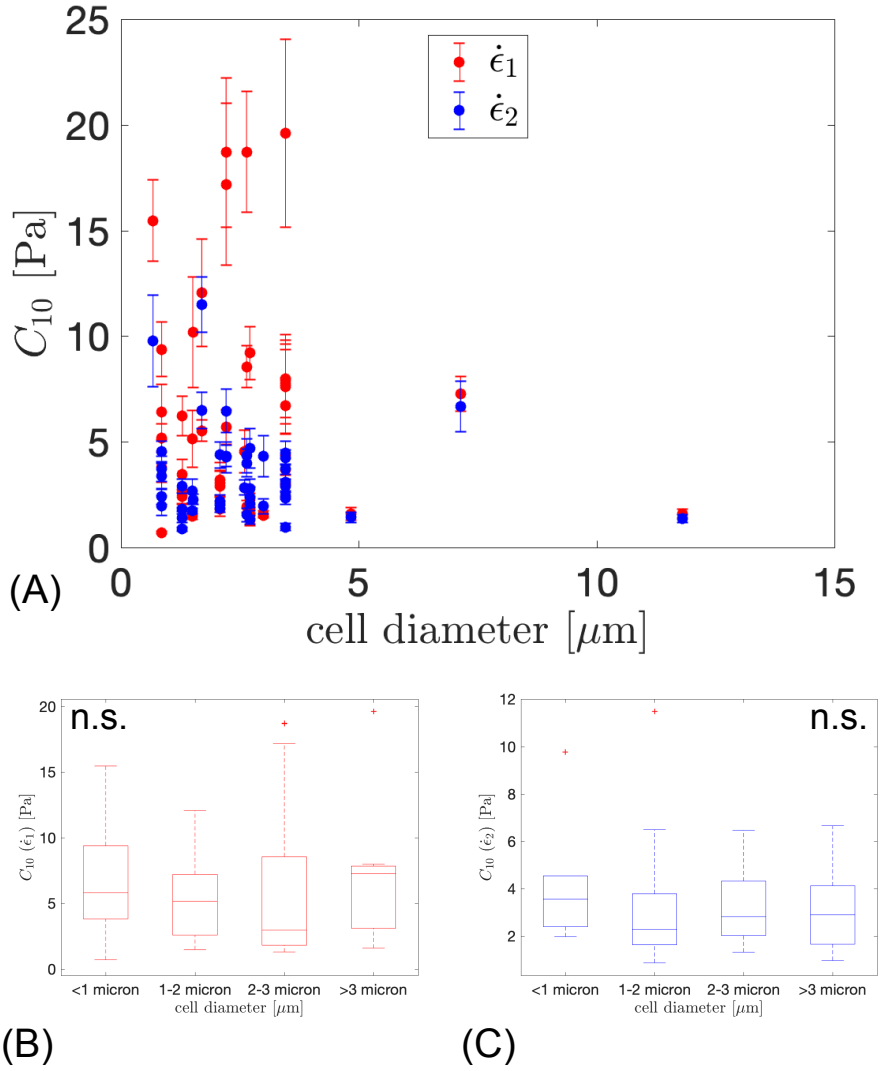

Figure 5.8: (A) Comparison of the fitted hyperelastic constants to the glial process diameters for the higher strain rate ($\dot{\epsilon}_1$, red) and slower strain rate ($\dot{\epsilon}_2$, blue). (B). A multiple comparison Bonferroni test showed no significant (n.s.) differences between C_{10} in the high strain rate regime (significant if p-value$<<$ 0.05) . (C) A multiple comparison Bonferroni test also showed no significant differences (n.s.) between C_{10} in the slower strain rate regime. Outliers in (B) and (C) are indicated with '+' signs for clarity.

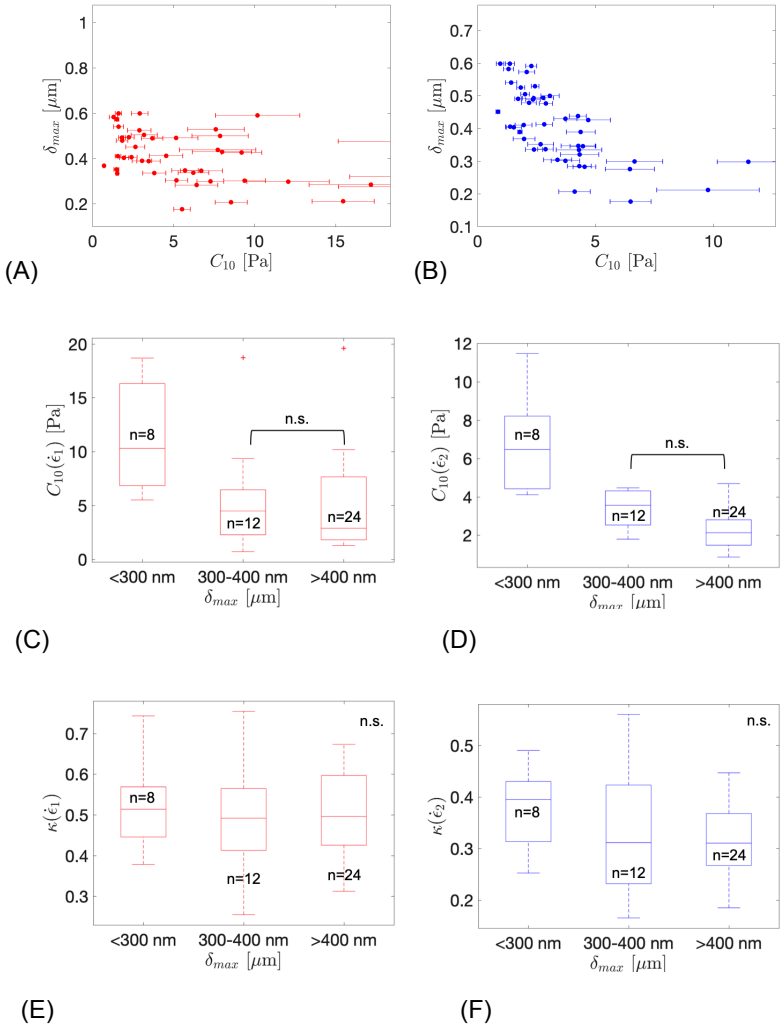

Figure 5.9: Comparison of material properties at (A) high strain rates ($\dot{\epsilon}_1$, red) and (B) lower strain rates ($\dot{\epsilon}_2$, blue) and the maximum indentation depth δ_{max}. (C) A multiple comparison Bonferroni test shows that although there was no significant difference between intermediate and large values of δ_{max}, the high strain rate regime showed that C_{10} values within $\delta_{max} < 300$ nm were significantly different ($p < 0.05$) to the other two groups. (D) Although there was no significant difference between intermediate and large values of δ_{max}, the low strain rate regime showed that C_{10} values within $\delta_{max} < 300$ nm were significantly different ($p < 0.05$) to the other two groups. (E-F) Comparison of the parameter κ across the varying calculated strain rates (n=44 for each strain rate). No statistically significant difference was found between δ_{max} and κ in neither the high strain rate (E) or low strain rate (F) regime. Outliers are indicated with '+' signs in (C).

Fig. 5.9C,D,E, and F, a one-way ANOVA test followed by Bonferroni's multiple comparison test was used to determine the significance (p-value$<<0.05$). Although no significance was found between intermediate and large indentation depths for C_{10} at both strain rate regimes (indicated by "n.s." in Fig. 5.9B-C), there existed a significant difference between $\delta_{max} < 300$nm and the two other groups ($\delta_{max} = 300-400$ and $\delta_{max} = 400$). Thus, for both strain rate regimes, differences in stiffness can occur within the first 300 nm of the surface.

In each box shown (Fig. 5.9C,D,E, and F), the central mark indicates the median, while the bottom and top edges of the box indicate the 25th and 75th percentiles, respectively. Looking at the 25th and 75th percentiles in Fig. 5.9D, we see that there was small variation in C_{10} within each group (especially for the two groups of largest δ_{max}). This demonstrates that for the majority of cells (n=36), there remained a homogeneously low stiffness value which allowed for large maximum indentations (300 - 600 nm).

We did not see any correlation between κ and the indentation depth δ_{max} (Fig. 5.9E-F). Furthermore, κ shows significant variations across each of the indentation δ_{max} groups. In other words, large variations in κ exist across variation indentation depths.

Figure 5.10 shows the effects of κ on the force displacement curves in comparison to the average experimental uncertainty in bead position. Note that changes in κ create subtle changes in the force-displacement curves at small indentation strains,

and the experimental uncertainty in bead position could make it difficult to accurately reflect differences in κ, as shown in Fig. 5.10. The error bars between the curves for $\kappa = 1$ and $\kappa = 0$ show some overlap, but only at small indentation strains. Fig. 5.10 also demonstrates how the neo-Hookean case ($\kappa = 1$) is slightly closer to the linear elastic approximation. As $\kappa \to 0$, the force-displacement curve deviates farther from linear elastic theory for an elliptical contact.

Figure 5.11 shows the values of C_{10} for $\dot{\epsilon}_2$ with the corresponding cell process diameters and maximum indentation depths. With the exception of a few specimens showing a high stiffness (and hence a small maximum indentation depth), the values of C_{10} remained relatively constant across the various cell process diameters. For a given maximum indentation depth, the stiffness C_{10} also appears uniform (independent of cell process diameter).

5.5 Identification of cell types

Although we were unable to distinguish between glial cell types during the experiment, we performed immunostaining on fixed specimens to have an idea of the cell type populations present in our scaffolds. As shown in Fig. 5.12, microglia, oligodendrocytes, and astrocytes were identified in the cell cultures. Although astrocytes were the most prevalent in the cell cultures, the experimental results contain a mix of these cell types, and thus no conclusions should be drawn regarding differences between cell

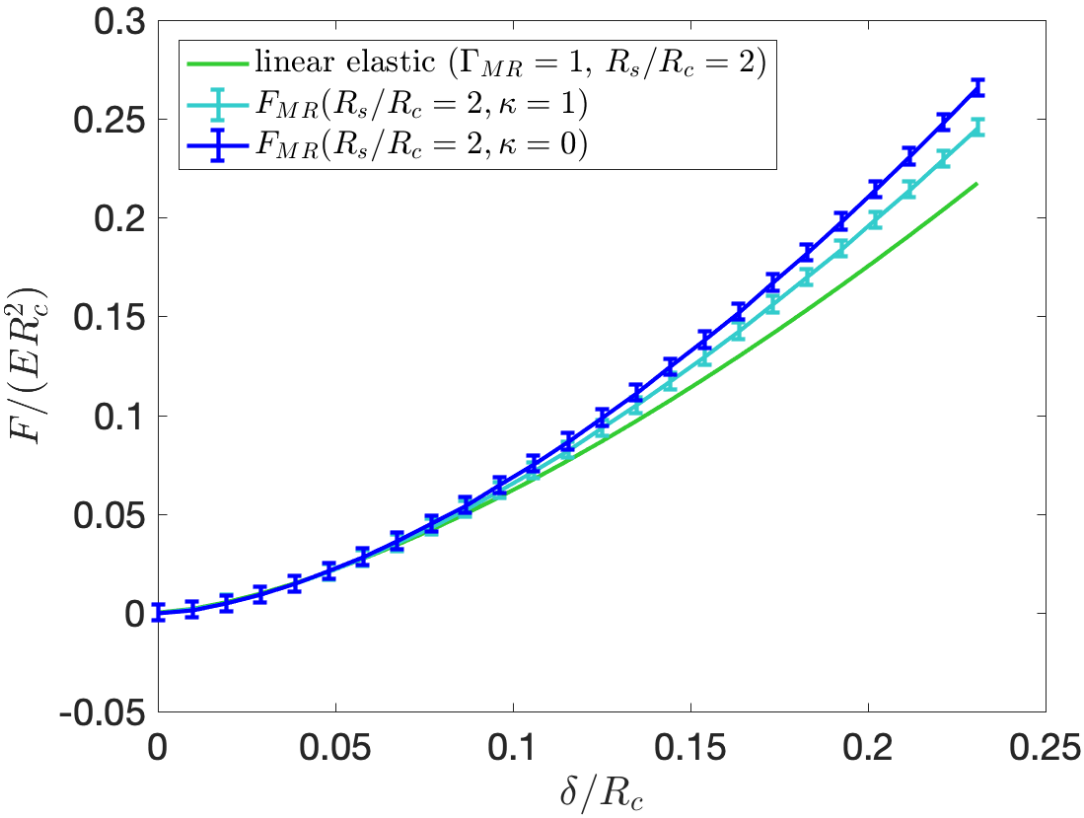

Figure 5.10: Non-dimensional theoretical force-displacement curves that compare the error from bead position uncertainty to effects of κ on the behavior of the force-displacement curve. We have superimposed error bars that correspond to errors in the force magnitude due to bead position uncertainty. Differences between $\kappa = 1$ and $\kappa = 0$ are small when compared to the predicted errors. Note that $\kappa = 1$ is closer to the linear elastic approximation, as expected.

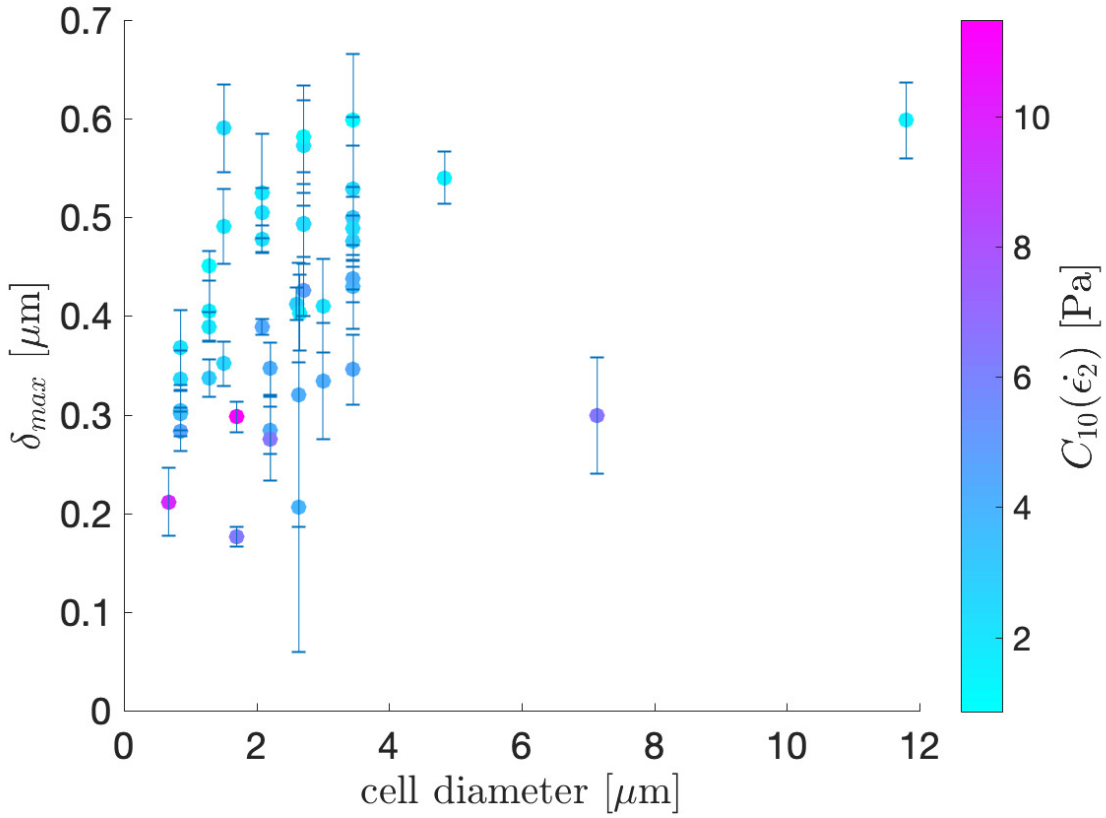

Figure 5.11: Comparison of maximum indentation depth (δ_{max}) and C_{10} for $\dot{\epsilon}_2$ across various cell process diameters.

type and properties. Figure 5.12 also demonstrates the different morphologies shown between 2D cell cultures and the PVDF 3D scaffold cell cultures across all cell types. On flat substrates, the glial cells showed a larger, more polygonal morphology in comparison to the 3D cultures.

Aside from staining for identification of cell types, we also stained for microtubules in all three cell types, since microtubules are believed to have a large influence on the compressive stiffness of cells [193], and have also been shown to be less prevalent in small processes of astrocytes [12] and oligodendrocytes [11]. Interestingly, it was observed that the microglia showed very little microtubule expression, although the amount of microtubule expression in microglia is dependent on reactivity/phenotype [194]. It is expected that microglia, oligodendrocyes, and astrocytes are expected to have some slight variations in mechanical response due to differing underlying cytoskeletons, although the extent of variation could be insignificant. Since fluorescence microscopy is compatible with the experimental OT platform, future work could consider isolating the glial cell cultures into specific cell types with endogeneously expressed fluorescent proteins that identify the cell types to investigate the possibility of material property differences between cell types.

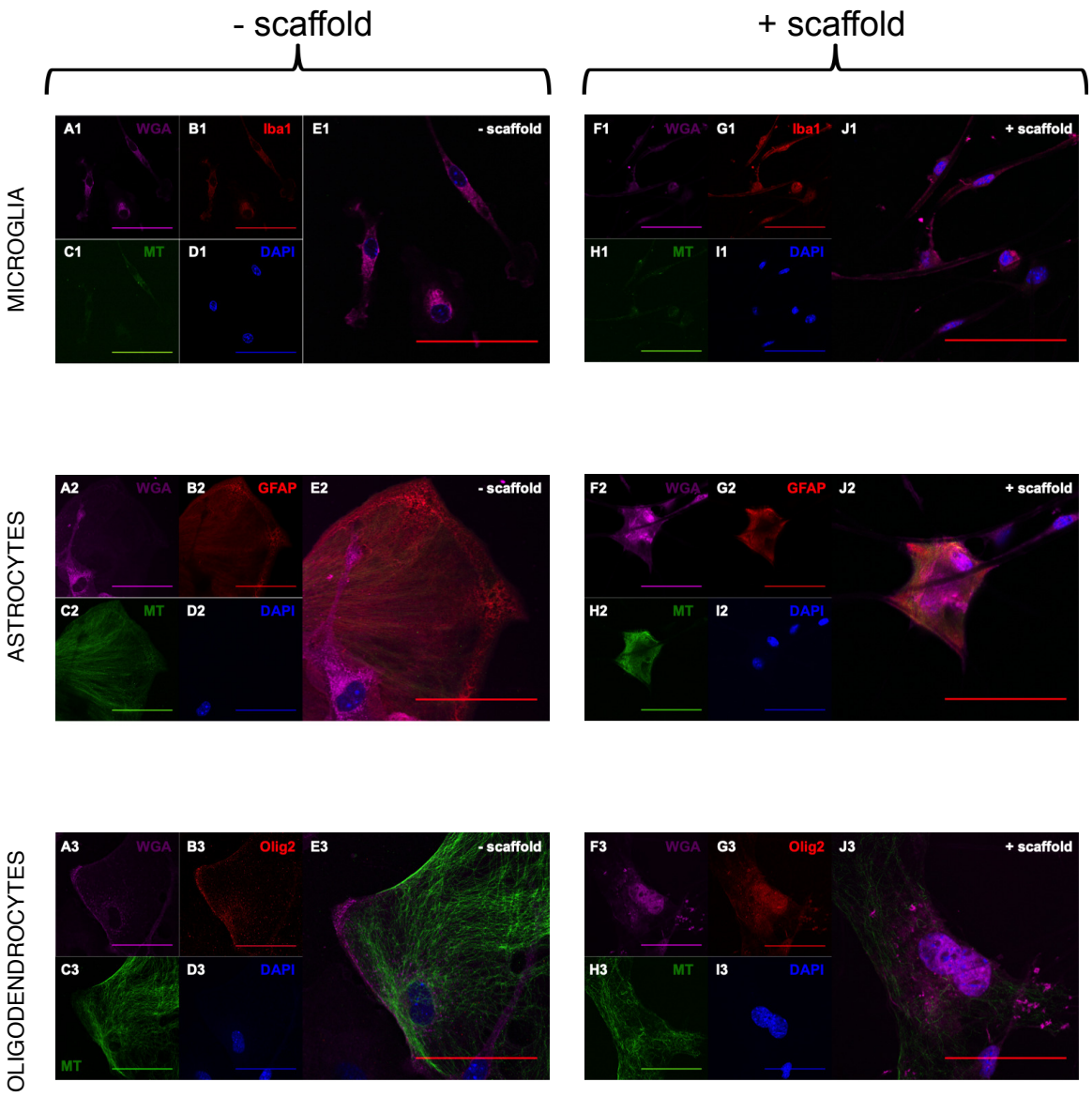

Figure 5.12: Immunostaining of glial cell cultures to determine cell type: **first row**=microglia, **second row**=astrocytes, **last row**=oligodendrocytes. **Left column**:Cells grown for 7 days on a glass substrate. **Right column**: Cells grown for 7 days on electrospun PVDF scaffolds. Cells were stained for plasma membranes (A1, A2, A3, F1, F2, F3), microtubules (C1, C2, C3, H1, H2, H3), and nuclei (D1, D2, D3, I1, I2, I3). For cell identification, Iba1 was used for microglia (B1, G1), GFAP was used for astrocytes (B2,G2) and Olig2 was used for oligodendrocytes (B3,G3). Merged fluorescence images are shown in E1, E2, E3, J1,J 2, and J3.

5.6 Discussion

5.6.1 Strain rate sensitivity

Biological materials, such as cells, often exhibit strain rate sensitivity, demonstrating a higher stiffness at higher strain rates [187]. This is believed to be partially due to the fact that when forces are applied slowly, crosslinkers in the cytoskeleton have sufficient time to rearrange, offering little resistance [195,196]. At higher strain rates, there is not enough time for crosslink rearrangement, and the cytoskeletal networks (e.g., actin networks) behave more rigid [195, 196]. Cells posses a variety of actin filament crosslinkers that bind with various affinities, which will ultimately cause variations in the strain-rate response in different types of actin networks (e.g., the actin cortex versus actin bundles associated with focal adhesions) [196].

5.6.2 Comparison to previously reported values

Our Young's moduli are comparable to some of the values reported by others [1,2]. The most comprehensive examination of the compartmental mechanical properties of glial cells was done by Lu et al. [1], where the Young's modulus of glial cell processes was found to be between 0.1-1 kPa. Using a small strain approximation, our experimental results show equivalent Young's moduli that are slightly lower (∼50-100 Pa). The difference in our softer values of Young's modulus could be attributed to the fact

that Lu et al. used 2D substrates and AFM, as well as a linear elastic theoretical force-indentation relationship for finding the material parameters. Assuming that cells exhibit hyperelastic behavior due to their biopolymeric composition, a linear elastic formulation could overestimate the Young's moduli by not considering strain stiffening effects.

There are also previously reported values of Young's moduli of glial cells that are orders of magnitude higher ($> 10,000$ kPa). The experiments used to obtain these high moduli shared in common the use of a sharp pyramidal indenter tip [8,10]. There are several reasons that could potentially cause sharper indenter tips to demonstrate higher stiffness, including: strain stiffening [56], substrate interactions from large deformation [145], contact area uncertainty [197], and the fact that sharp tips probe a more local region of the cell [46].

5.6.3 Limitations of the experimental platform and future work

The OT setup presented here is capable of high temporal and spatial resolution. However, it is limited by the maximum force (∼22 pN) and maximum allowable deflection (∼610 nm) of the trap. With the particular laser beam intensity and silica beads used in our experiment, the maximum allowable deflection limited us to probing only the first 600 nm from the cell membrane surface. It is uncertain if the majority

of our results only reflect the actin cortex, although we did see evidence of variation in stiffness values within the first 300 nm. It should also be noted that, even though our results show nearly homogeneous values of stiffness for the first 600 nm of indentation, there could be a higher limit (> 600 nm) that also shows relative homogeneity.

As mentioned earlier, the experimental uncertainties make it difficult to determine how accurately κ can be determined. Obtaining clean force-displacement curves was also a challenge since the OT will draw nearby floating molecules into its center. Thus, experiments could not be repeated for an extended amount of time since the trap would bring in nearby molecules that would stick to the bead and generate more noise. Furthermore, even in the case of minimal noise, it was not possible to precisely check for alignment until post-processing the tangential forces from the QPD sensor data.

This experiment provides a more realistic morphology, but the underlying substrate is not the same as *in vivo* conditions, which could alter the underlying cytoskeleton and mechanical behavior. Nevertheless, it allows us to probe glial cellular processes, a morphological feature that is nearly lost when cells are grown on flat 2D substrates. The smallest processes probed in our experiments were roughly 700 nm in diameter, but this setup can be used to probe smaller processes (as small as 270 nm), as defined by the Rayleigh criterion: $d = \frac{1.2\lambda}{2N.A.}$ (where d is the minimum resolved feature size, $\lambda \approx 550$ nm, and N.A.=1.25 in our experimental setup).

5.6.4 Implications for homogenization length scales in mechanics-based models

Our results demonstrate that C_{10} values did not correlate with glial cell process diameter across the range observed (600 nm to 12 μm). However, since our experiments only probe the first 600 nm of indentation depth from the cell membrane, it is possible that C_{10} values become larger at greater indentation depths for large processes. Our experiments suggest that even though some heterogeneities within 300 nm of the membrane can result in a slightly stiffer response (with an average $C_{10} = 7 - 10$ Pa), the majority of cells showed a homogeneous response (with an average $C_{10} = 3 - 5$ Pa).

Our analysis also suggests that for glial cell processes < 600 nm, one can homogenize the mechanical properties of the glial cellular network using the strain-rate dependent material properties provided in Table 5.3.1. A schematic showing the proposed homogenization scale is shown in Figure 5.13. For small cell processes with $R_c < 600$ nm ("material 2" in Fig. 5.13), the mechanical response can be characterized by the properties of Table 5.3.1. For large cell processes with $R_c > 600$, the first 600 nm layer from the cell surface also exhibits homogeneous properties, but no conclusions can be drawn regarding homogeneity at this length scale since our experiment only probed the first 600 nm. Therefore, at length scales where cell processes possess radii > 600 nm, the bulk behavior of the material ("material 1" in Fig. 5.13)

could be attributed to both an outer "material 2" and deeper cytoskeletal structures with varying stiffnesses.

5.7 Summary

By obtaining positional data during the indentation of an optically trapped bead on cells grown in scaffolds, we have developed a new method to obtain local mechanical properties of cells grown in a 3D environment. Although, this technique is developed specifically for glial cells grown on a relatively rigid 3D polymeric scaffold, it can be used to probe the strain-rate dependent and nonlinear properties of various adherent cell types in a more native environment. Our key findings are summarized below:

- The hyperelastic constant C_{10} ranged from 1-20 Pa across all experiments and strain rates, while κ ranged from .17 to .75
- As expected of a biopolymeric material, our cells exhibited a statistically significant stiffer response at higher strain rates (2-3 times higher than the slower strain rates). The higher strain rates also showed significantly higher values of κ.
- Our results also show that although there are occasional inhomogeneities within the first 300 nm of the cell surface that can cause differences in stiffness, the first 600 nm of indentation depth into the cell surface show overall homogeneous material properties for a given strain rate.

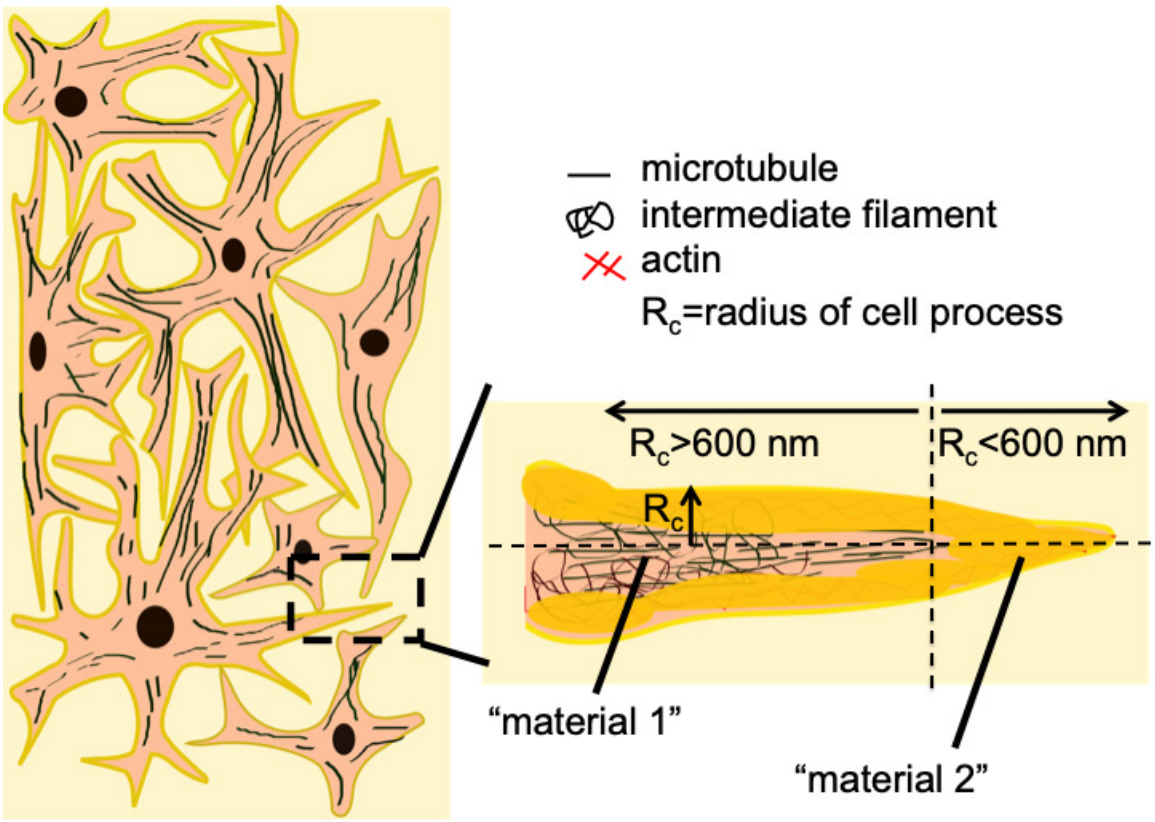

Figure 5.13: Schematic showing the homogenization scale examined in this study. The low standard deviation in hyperelastic material properties during the second strain rate regime (0 to 40 s^{-1}) suggest that we can homogenize the material (yellow region indicated as "material 2") at length scales smaller than $R_c < 600$ nm. Note that since our experiments only probe the first 600 nm of indentation depth from the cell membrane, it is possible that homogenization can be applied at larger length scales ($>$ 600nm) which are outside the scope of this work.

In summary, we have demonstrated that glial cellular features that are smaller than 600 nm in diameter can be approximated as a homogeneous material with the strain-rate dependent hyperelastic properties provided herein. Given the structural complexity of glial cellular networks in the brain, we hope that this can help simplify future mechanical models of brain tissue at small length scales.

Chapter 6

Conclusion

6.1 Contributions of the work

Our simulations of cerebral arteriole inflation in Chapter 2 demonstrated a practical example where heterogeneity observed at the mesoscale is important for quantifying the cellular injury seen in neuropathology. Since mild TBI is typically undetectable with current *in vivo* imaging methods, it is necessary to rely on post mortem analysis of specimens at the mesoscale. However, as the heterogeneity within the mesoscale is not fully characterized to date, we sought to obtain experimental data to aid in simplifying future mechanics-based models of complex CNS structures. This work provides a starting point for characterizing the mechanical properties of glial cells for future mesoscale models of traumatic brain injury, as well as improvements to conventional techniques in characterizing the mechanical properties of any type of

cell. The following are the key contributions from this thesis:

- Chapter 2 provides an example of the importance of studying the mechanical properties at the mesoscale. It was demonstrated that the heterogeneity in material properties between the arterioles and surrounding brain tissue determined the type of resulting damage pattern ("normal" or "honeycomb").

- Chapter 3 presented a novel experimental platform that allowed for probing the mechanical properties of cells in a 3D fibrous polymer network. To our knowledge, this is the first reported experimental method that can probe mechanical properties of adherent cells in a 3D environment.

- We developed a nonlinear contact formulation for the indentation of hyperelastic cylindrical bodies in Chapter 4. This was not only useful for our own particular experiment, but can be used in the future for a wide variety of applications (e.g., indentation testing on collagen, bacteria, neurites, etc.)

- In Chapter 5 we presented various findings on the mechanical properties of glial cells. We found that the hyperelastic material properties were similar at indentation depths up to 600 nm, with some inhomogeneities that can occur within the first 300 nm. Although there was a statistical difference of C_{10} when $\delta_{max} < 300$nm, the actual difference was $C_{10} = 10$ Pa instead of $C_{10} = 5$ Pa (not a very large difference in the big picture of reported values on glial cel properties).

- Contrary to what we expected, no correlation was found between hyperelastic properties and cell diameters in the range of cell process diameters examined (0.8-12 μm).

- Cell stiffness was largely dependent on strain rate, with moduli being approximately 2 times larger for high strain rates ($> 30 - 40s^{-1}$) in comparison to lower strain rates ($< 10s^{-1}$).

Results from our experimental data suggest that glial cellular networks are roughly homogeneous for feature sizes < 600 nm. Thus, future mesoscale models can be great simplified with this length scale in consideration. It should be noted however, that 600nm was the maximum testable limit of our experiment, and that a larger upper limit for a homogenization scale might exist.

6.2 Suggestions for future work

Due to the importance of linking the mechanics of brain tissue with post mortem pathology, as well as the increased availability of mesoscale structural connectome datasets [41, 201–203], it is likely that computational models at smaller length scales will emerge. The work provided herein is a contributor to one small aspect in the development of future computational models–the homogenization (and therefore, simplification) of glial cellular networks. In our experiments we only probed compartmental properties of glial cells, which as previously stated, only comprise about half

of the non-vasculature content of the brain. Some possible extensions of this work towards the realization of mesoscale physics-based models are summarized below:

- Since neurons are also known to grow on electrospun PVDF scaffolds [198,199], this experimental setup could be applied to obtain mechanical properties of neurites, such as axons and dendrites, as well. Based on previous reports [1], it is expected that neurons would be stiffer than glial cells, while soft enough to still probe with the OT platform.

- The OT platform, as established in this work, would most likely not be useful for probing mechanical properties of capillaries, which are shown to have a high density throughout brain tissue (roughly 100 capillaries/mm^3 [200]). As discussed in Chapter 2, there is a scarcity of data on human cerebral vasculature, which includes not only arterioles, but capillaries as well. Incorporation of accurate mechanical properties of cerebral microvasculature would presumably be very important in mesoscale models of TBI.

- It remains to be determined whether or not homogenization of the mechanical properties of glial cell feature sizes < 600 nm would successfully simplify a real-life 3D dataset of mesoscale CNS structures. It is possible that the majority of glial cell process volume is larger than this feature size. However, examination

of a 3D electron microscopy dataset would be able to provide an idea of the volume fractions of glial cell processes and neurites that are are sufficiently small enough to have homogeneous material properties. With the growing availability of cellular connectomics data [41, 201–203], this might also be readily tested in the near future.

- As the mechanical properties of glial cells could be important for studying CNS regeneration, one could also expand this work into considering the changes in stiffness of glial cells as a function of reactivity following injury. In more severe cases of TBI, there is the formation of a glial scar, a relatively stiffer area comprised of reactive astrocytes which inhibits neural regeneration [204]. Studying the mechanical properties of reactive astrocytes could aid in the design of future scaffolds to promote neuronal regeneration, as well as assisting in the development of future diagnostic technologies.

- As shown in the comparison between cellular mechanical properties across the literature (Fig. 1.4), there is a need in the field of cellular biomechanics for establishing more uniformity and standardization during testing. Even within the same cell type, different types of mechanical testing procedures can result in elastic moduli which vary 1,000-fold due to the extent of deformation, the rate of deformation, the geometry of the probe, the location probed in the

cell, and the extracellular microenvironment [44]. Therefore, it could be useful to perform additional testing with the setup presented here to probe different cellular compartments at different loading rates.

Although we have left out the mechanical properties of neurons in this experimental study, simplifying glial cell networks at the mesoscale might be sufficient for modeling white matter regions, which are comprised primarily of a single neurite type (axons). Since previous studies have examined the mechanical properties of axons, and since they are roughly similar cross-sectional sizes, the white matter would presumably be an easier starting point for modeling the mesoscale. Expanding the experimental work to obtain mechanical properties of various dendrites and cell bodies, is something that would be critical for more complex gray matter mesoscale models.

Herein we focused on obtaining collective microscale properties in order to infer homogenization at the mesocale. We did not discuss how future mesoscale models will be bridged to the macroscale. In the future, the mechanical behavior at the macroscale could be used to help understand the collective behavior of cells (e.g., cell-cell adhesion and sliding). However, relating these two length scales would require a different type of experimental setup, which is outside the scope of the current work.

6.3 Concluding remarks

Due to the difficulties in detecting mild TBI with non-invasive imaging techniques, it is critical to improve our knowledge of mesoscale mechanics of brain tissue in order to understand the mechanisms surrounding cellular-level injury. Cellular damage surrounding arteriole inflation, blood-brain-barrier (BBB) rupture, accumulation of phosphorylated tau proteins, and astrocyte reactivity, are just a few examples of injury caused by damage to mesoscale structures during TBI. We hope this work will aid in the creation of models that help relate how macroscale brain injury events translate to damage in cellular networks. With a better understanding of the mechanical response of the cellular constituents that comprise the CNS, we might gain new physics-based insights on neuropathological observations following TBI events.

Appendix A

A.1 Derivation of the analytical solution for heterogeneous tissue under inflation

The equilibrium equations for a cylinder subjected to internal/external pressures in the absence of body forces reduce to:

$$\frac{d\sigma_{rr}}{dr} + \frac{\sigma_{rr} - \sigma_{\theta\theta}}{r} = 0 \tag{A.1}$$

Although soft tissues exhibit nonlinear large deformation responses, we will only consider a heterogeneous linear elastic material for simplicity. The strain-displacement relations for small axisymmetric deformations in cylindrical coordinates are given by:

$$\epsilon_{rr} = \frac{du_r}{dr}, \epsilon_{\theta\theta} = \frac{u_r}{r}, \epsilon_{zz} = \frac{du_z}{dz} \tag{A.2}$$

To represent the heterogeneity between the relatively stiff arteriole wall and softer brain tissue, we will assume a Young's modulus $E(r)$ that varies radially throughout the cylinder, as considered in previous work with pressurized functionally graded cylinders (Horgan and Chan 1999). To further simplify the problem, we consider the *plane stress* state ($\sigma_{zz} = 0$) and assume that the Poisson's ratio ν is constant (independent of r). The stress-strain relations are then:

$$\sigma_{rr} = \frac{E(r)}{1-\nu^2}\left[\frac{du}{dr} + \nu\frac{u}{r}\right] \tag{A.3}$$

$$\sigma_{\theta\theta} = \frac{E(r)}{1-\nu^2}\left[\frac{u}{r} + \nu\frac{du}{dr}\right] \tag{A.4}$$

One can obtain the *plane strain* idealization by replacing $E(r)$ with $\frac{E(r)}{1-\nu^2}$ and replacing ν with $\frac{\nu}{1-\nu}$. Substitution of Equations A.3 and A.4 into Equation A.1 gives:

$$\frac{d^2u}{dr^2} + \frac{1}{r}\frac{du}{dr} - \frac{u}{r^2} + \frac{1}{E(r)}\frac{dE(r)}{dr}\left(\frac{du}{dr} + \nu\frac{u}{r}\right) = 0 \tag{A.5}$$

Equation A.5 is now simplified to:

$$\frac{d^2u}{dr^2} + \frac{(n+1)}{r}\frac{du}{dr} + (n\nu - 1)\frac{u}{r^2} = 0 \tag{A.6}$$

which is an Euler differential equation with roots $m_1 = (-n-k)/2$ and $m_2 =$

$(-n+k)/2$ for $k=\sqrt{n^2+4-4n\nu}$. Solutions will take the form:

$$u(r) = Ar^{m_1} + Br^{m_2} \tag{A.7}$$

Substituting Equation A.7 into Equations A.3 and A.4, we can rewrite the Cauchy stress in terms of the constants A and B:

$$\sigma_{rr} = \frac{E(r)}{(1-\nu^2)r}[(m_1+\nu)Ar^{m_1} + (m_2+\nu)Br^{m2}] \tag{A.8}$$

$$\sigma_{\theta\theta} = \frac{E(r)}{(1-\nu^2)r}[(1+\nu m_1)Ar^{m_1} + (1+\nu m_2)Br^{m_2}] \tag{A.9}$$

After applying the inner and outer boundary conditions, $\sigma_{rr}(r=a) = -p$ and $\sigma_{rr}(r=b) = -q$, one obtains the constants A and B:

$$A = \frac{(-ab^{m_2}E_b p + a^{m_2}bE_a q)(\nu^2-1)}{(a^{m_2}b^{m_1} - a^{m_1}b^{m_2})(m_1+\nu)E_a E_b} \tag{A.10}$$

$$B = \frac{(ab^{m_1}E_b p - a^{m_1}bE_a q)(\nu^2-1)}{(a^{m_2}b^{m_1} - a^{m_1}b^{m_2})(m_2+\nu)E_a E_b} \tag{A.11}$$

Where we have defined $E_a = E(r=a)$ and $E_b = E(r=b)$. Note that $E_a \geq E_b$. Using Equations A.10 and A.11 in Equations A.8 and A.9, we obtain the final form for the radial and tangential stresses:

$$\sigma_{rr} = C_1\frac{E(r)}{r}\left[C_2 r^{m_1} + C_3 r^{m_2}\right] \tag{A.12}$$

$$\sigma_{\theta\theta} = C_1 \frac{E(r)}{r} \left[C_4 C_2 r^{m_1} + C_5 C_3 r^{m_2} \right] \tag{A.13}$$

where C_1, C_2, C_3, C_4, and C_5 are given by:

$$C_1 = \frac{1}{E_a E_b (a^{m_1} b^{m_2} - a^{m_2} b^{m_1})} \tag{A.14}$$

$$C_2 = -ab^{m_2} E_b p + a^{m_2} b E_a q \tag{A.15}$$

$$C_3 = ab^{m_1} E_b p - a^{m_1} b E_a q \tag{A.16}$$

$$C_4 = \frac{1 + \nu m_1}{m_1 + \nu} \tag{A.17}$$

$$C_5 = \frac{1 + \nu m_2}{m_2 + \nu} \tag{A.18}$$

The well-known solution for the homogeneous case ($E(r) = E_0$) can be retrieved by setting $n = 0$ (and therefore $k = 2$, $m_1 = -1$, and $m_2 = 1$) in equations A.12 and A.13:

$$\sigma_{rr} = \frac{pa^2 - qb^2 + a^2 b^2 (q - p)/r^2}{b^2 - a^2} \tag{A.19}$$

$$\sigma_{\theta\theta} = \frac{pa^2 - qb^2 - a^2 b^2 (q - p)/r^2}{b^2 - a^2} \tag{A.20}$$

We then compute the resulting strains for the heterogeneous case:

$$\epsilon_{rr} = \frac{\sigma_{rr}}{E(r)} - \frac{\nu}{E(r)}(\sigma_{zz} + \sigma_{\theta\theta}) \tag{A.21}$$

$$= \frac{C_1}{r}(C_2 r^{m_1} + C_3 r^{m_2}) - \nu\frac{C_1}{r}(C_4 C_2 r^{m_1} + C_5 C_3 r^{m_2}) \tag{A.22}$$

$$\epsilon_{\theta\theta} = \frac{\sigma_{\theta\theta}}{E(r)} - \frac{\nu}{E(r)}(\sigma_{rr} + \sigma_{zz}) \tag{A.23}$$

$$= \frac{C_1}{r}(C_4 C_2 r^{m_1} + C_5 C_3 r^{m_2}) - \nu\frac{C_1}{r}(C_2 r^{m_1} + C_3 r^{m_2}) \tag{A.24}$$

$$\epsilon_{zz} = \frac{\sigma_{zz}}{E(r)} - \frac{\nu}{E(r)}(\sigma_{rr} + \sigma_{\theta\theta}) \tag{A.25}$$

$$= -\frac{\nu C_1}{r}(C_2(1 + C_4) r^{m_1} + C_3(1 + C_5) r^{m_2}) \tag{A.26}$$

In the homogeneous case, $E(r) = E_0$ and the axial strain, under plane stress ($\sigma_{zz} = 0$) is:

$$\epsilon_{zz} = -\frac{\nu}{E_0}\left[\frac{2(a^2 p - b^2 q)}{b^2 - a^2}\right] \tag{A.27}$$

Thus for a constant Young's modulus, the axial strains for a homogeneous cylinder under applied pressures p and q, are independent of r. The distance r at which strains transition from negative to positive depends on the choice of parameter n. The locations at which the axial strain becomes positive, are simply calculated as the values ρ at which $\epsilon_{zz}(r = \rho) = 0$ in Equation 2.7:

$$\rho = \left[\frac{(m_1 + \nu + 1 + \nu m_1)A}{(-1 - \nu m_2 - m_2 - \nu)B}\right]^{(1/k)} \tag{A.28}$$

Where the constants A and B are given in Appendix A. Real solutions to equation

A.28 exist when the expression in the brackets ($\left[\cdot \right]$) is positive.

A.2 Analytical solution results (no external pressure)

Here we will discuss the analytical solution for homogeneous and heterogeneous cylinders in the case of no external pressure ($q = 0$, i.e., isolated arterioles). We first reiterate the standard solutions for the case of a homogeneous cylinder under internal inflation only ($q = 0$), where the radial and tangential stresses (Fig. A.1a) are equal in magnitude, opposite in sign, and independent of E_0/p. Although the radial and circumferential strains will vary across r, the axial strains remain constant across all values of r (Fig. A.1b). When we consider the heterogeneous case of $q = 0$ (Fig. A.1c), the radial and tangential stresses now become dependent on the choice of n. For illustrative purposes, two values for the parameter n were chosen: $n = -1.5$ and $n = -0.5$. For $q = 0$, the stronger heterogeneity ($n = -1.5$) results in a steeper decrease in stress with respect to the radial distance r (Fig. A.1c). The axial strains (Fig. A.1d) are negative (compressive), and gradually decay towards zero as a function of r. The magnitude of ϵ_{zz} depends on the value of n selected for the function $E(r)$.

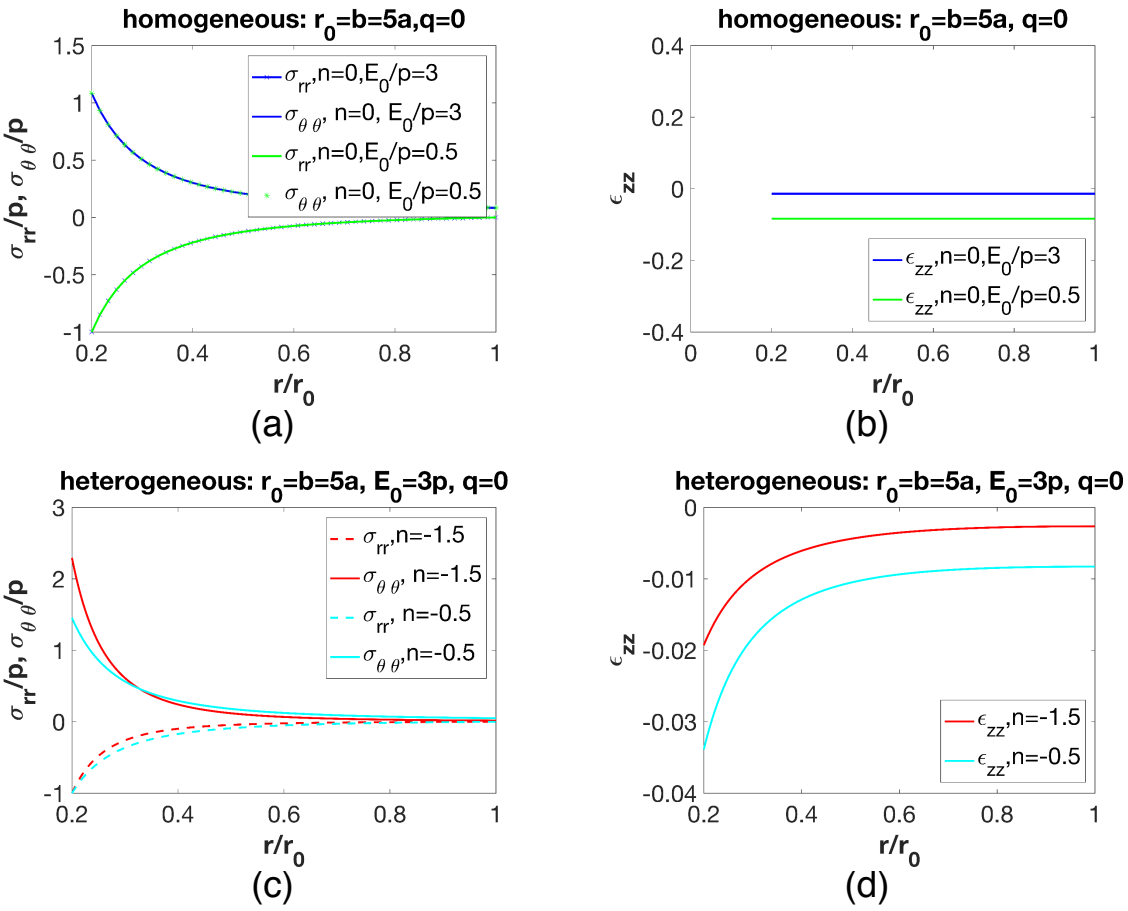

Figure A.1: Results for a single cylinder with internal pressurization p and no external pressurization ($q = 0$). Top row (a-b) shows stresses and strains in the homogeneous case ($n = 0$) for two different ratios of E_0/p, while the bottom row (c-d) shows the heterogeneous case. For all cases, a=17.5 microns, b=5a, and Poisson's ratio $\nu = 0.5$. The parameter n was changed to simulate the variation in arteriole wall thickness and stiffness. For a steep heterogeneity, $n = -1.5$, while for a gradual heterogeneity $n = -0.5$.

In the heterogeneous case of Fig.A.1c, we see similar behavior as before, although now the radial stresses plateau to the value of q_0 instead of $q = q_{eff}$. In the case of no effective external pressure ($q = 0$, Fig. A.1b and Fig. A.1d), only compressive strains arise in the case of a single cylinder, for both homogeneous or heterogeneous materials.

A.3 Simplified expression of analytical solution

Fig. A.2a shows the dependence of m_1 and m_2 on the chosen value of n. Note that m_1 is nearly independent of n (for the range of n chosen), and we can therefore approximate $m_1 = -1$ if we wish to simplify the solution. The solution for displacement at equilibrium is simplified as:

$$u(r) \approx \frac{A}{r} + Br^{m_2} \tag{A.29}$$

and our expression of axial strain as:

$$\epsilon_{zz} \approx -\frac{\nu C_1^*}{r}(C_3(1 + C_5)r^{m_2}) \tag{A.30}$$

The constants C_3 and C_5 are independent of m_1. C_1^* simplifies to:

$$C_1^* \approx \frac{1}{E_a E_b(\frac{b^{m_2}}{a} - \frac{a^{m_2}}{b})} \tag{A.31}$$

Figure A.2b compares the axial strains of the exact solution versus the approximate

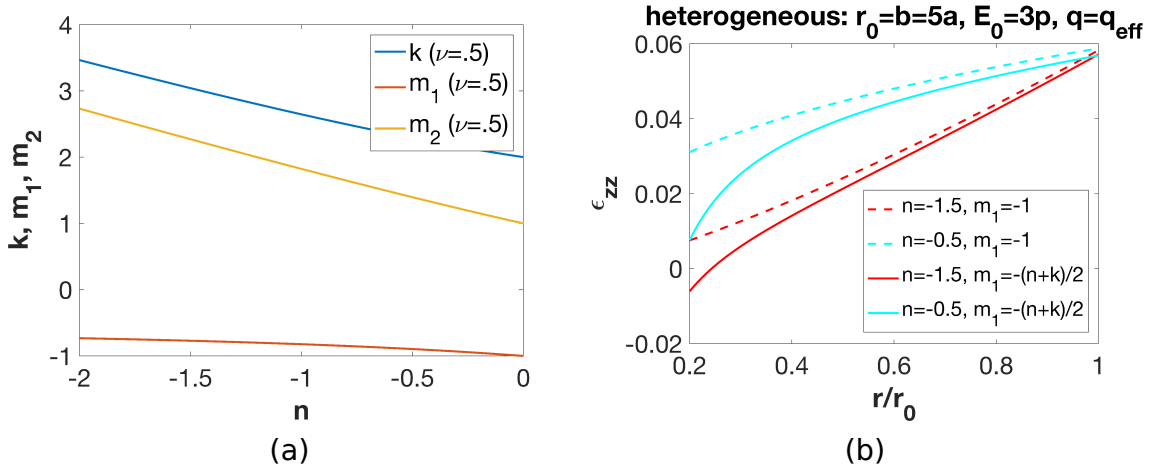

Figure A.2: **(a)** Linear dependence of exponents (m_1,m_2) for the displacement solution in Equation A.7. **(b)**Comparison of analytical model used in this study (m_1 as a function of n, solid lines), versus a simplified model that approximates a constant value of m_1 (dashed lines). A steeper heterogeneity ($n = -1.5$, red lines) is compared to a gradual heterogeneity ($n = -0.5$, blue lines).

solution using $m_1 = -1$ for the case of a hetergeneous cylinder subjected to external pressure. Although both cases ($n = -0.5$ and $n = -1.5$) demonstrate poor agreement of axial strain at the arteriole wall ($r/r_0 = 0.2$), the solutions converge to similar magnitudes when r/r_0 is greater than 0.5.

Appendix B

B.1 Practical considerations while "trapping"

B.1.1 Sample preparation for calibration of OT

1. To prepare a sample, begin with a regular microscope slide and apply two pieces of double sided tape (roughly a half-inch apart).

2. Place a rectangular coverslip (thickness of .17 mm needed for most high NA objectives) directly over the two pieces of tape, and perpendicular to the microscope slide). This results in a microchannel, approximately 100 microns in depth.

3. Prepare the microbead solution. Vortex the silica bead solution (Bangs Laboratories) and add 5 μl from the stock container to 1 ml of filtered DI water.

Although this dilution is sufficient for trapping, it is recommended to dilute it further (about 10x more) so that only one bead exists in the microscope field of view. This will prevent the trapping of multiple beads, which can ruin the calibration process. The bead solution should be placed in the refrigerator for storage. If it is desirable to have more beads "stuck" to the coverslip for calibration purposes, the DI water in this step can be replaced with sterilized phosphate buffer solution (PBS).

4. Pipette approximately 20-40 μl of the bead solution into the microchannel until the channel is filled.

5. The bead solution in the microchannel can dry out quickly, so it is important to seal the two channel openings with either vacuum grease or clear nail polish.

6. Place a drop of immersion oil onto the 100x (1.2 NA) objective. Make sure to remove any tiny microbubbles within the oil by gently popping them with the corner of a wipe. Before and after each experiment, make sure the objective is thoroughly cleaned with an ethanol soaked lens cleaning tissue

7. Place the specimen into the specimen holder stage, with the coverslip side down. The specimen stage should be in the highest z-position and roughly positioned in the proper X,Y location of interest. Slowly lower the z-position until it touches the oil objective. You should see the spot of oil spread as the slide moves into closer contact. Watch the camera acquistion software for the specimen to come

into focus.

8. If the camera screen is too dark, the sample is not being illuminated properly. Try adjusting the relative distance between the illumination source and the objective and make sure the illumination source is properly aligned.

B.1.2 Recognizing trapping

1. Focus in the z-direction until a few beads appear within the field of view.

2. For 2-5 micron diameter silica beads, trapping is easily achieved with 200-600 mA of applied current to the laser diode. Set the current limit for the laser diode at 400 mA, and slowly move the stage in the x and y directions.

3. If the current is too high, and lighter beads (like polystyrene) are being used, it is possible that the scattering force will be too high and a stable trap cannot be achieved. Note that for our particular laser diode, the lowest current possible to provide a stable laser spot is set at 50 mA.

4. A trapped bead will "jump" into the laser trap focus and stay in the trap's same X and Y location, even as you translate the stage. If trapping only happens in the X and Y directions, the laser is probably not properly aligned, or the laser power might be too low or too high.

B.2 OT calibration

B.2.1 Calibration of QPD

Using our strain gauges on the actuator stage, the QPD sensor is calibrated to determine how the QPD voltage output corresponds with the bead position. This is done by "scanning" the transmitted laser over the area of a bead stuck on the bottom glass by moving the stage accordingly. After plotting the voltages over the measured strain gauge distances, a conversion factor (units volts/μm) is obtained. A QPD calibration in the x-, y-, and z-directions should be done for each type of bead required for the experiment. It is important that the bead remains adhered to the bottom glass and does not get pulled into the laser trap. To promote adhesion to the glass substrate, the bead can be suspended in 10X PBS solution (or any saline solution), as mentioned in the previous section.

B.2.2 Stiffness calibration: PSD (power spectral density) method

The stiffness of an optical trap can be calibrated by any of the following techniques:

- **Stokes flow**. By applying a constant velocity to the sample, the drag force on the particle is given by $F_d = 6\pi\eta R v_s = k_i x_i$ where x_i is the observed displace-

ment. R is the radius of the bead, and v_s is the flow velocity. The effective dynamic viscosity, η, can be measured experimentally from the mean squared displacement of particles in solution (see Appendix B.3 for more details).

- **Equipartition theorem**. Uses the principle that each degree of freedom in a system at thermal equilibrium will have an energy of $\frac{1}{2}k_bT = \frac{1}{2}k_i < x_i^2 >$, where k_i is the stiffness and $< x_i^2 >$ is the statistical variance of the particle position.

- **PSD roll-off method**. Relates the observed frequencies of particle motion in the trap to the theoretical frequencies of a damped massless oscillator.

The power spectrum density (PSD) roll-off analysis of the position of a trapped bead is usually considered to be the most reliable method for optical tweezer calibration [147]. The main principle is that the frequency of the particle motion is related to the strength of the trap: as the stiffness increases, high frequency movements dominate. Typically the frequencies of the particle motion go up to several kHz, so one must use photodetectors which have a large bandwidth. Since the sampling frequency should be at least twice as large as the largest expected frequency in our system, the sampling rate for the photodiode (in this case, set through a Labview program) should be > 12 kHz.

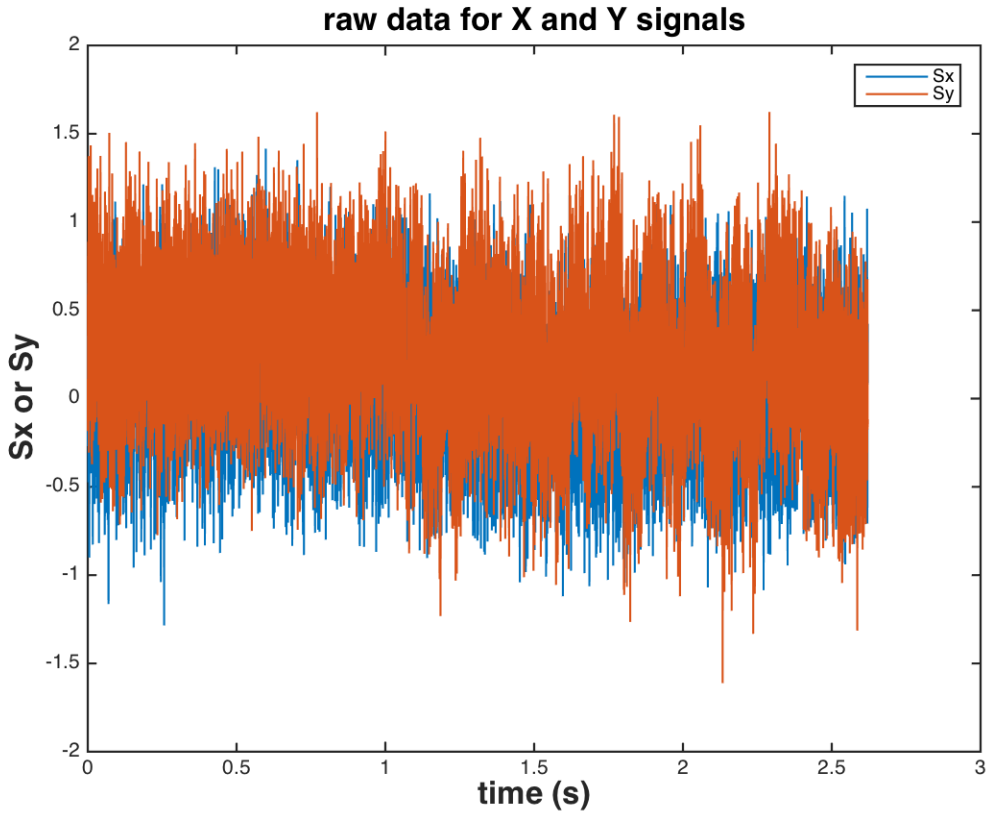

Figure B.1: voltage signal S(t) from QPD response recording movements of a trapped microsphere

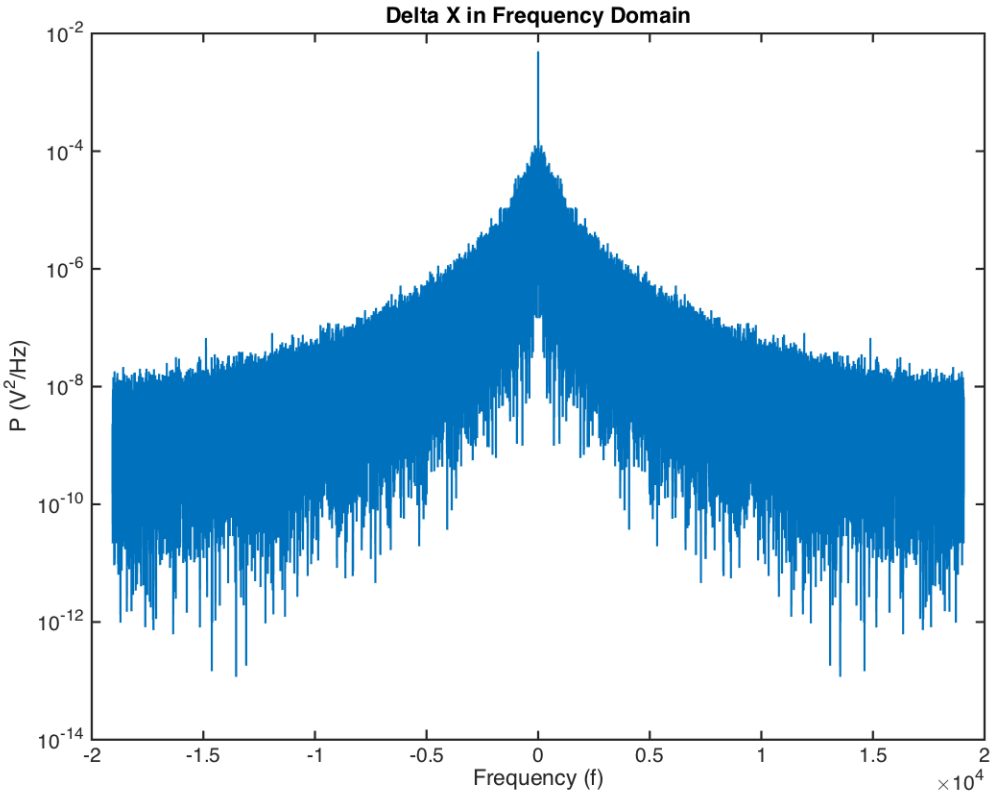

Figure B.2: two-sided power spectrum

The power spectrum for a signal over time S(t), such as figure B.1 can be represented as:

$$P = |S(f)^2| \tag{B.1}$$

Where $S(f)$ is the Fourier transform (FT) of the original signal over time S(t). The power spectrum can be plotted over the Nyquist frequency range (one-half of the sampling frequency).

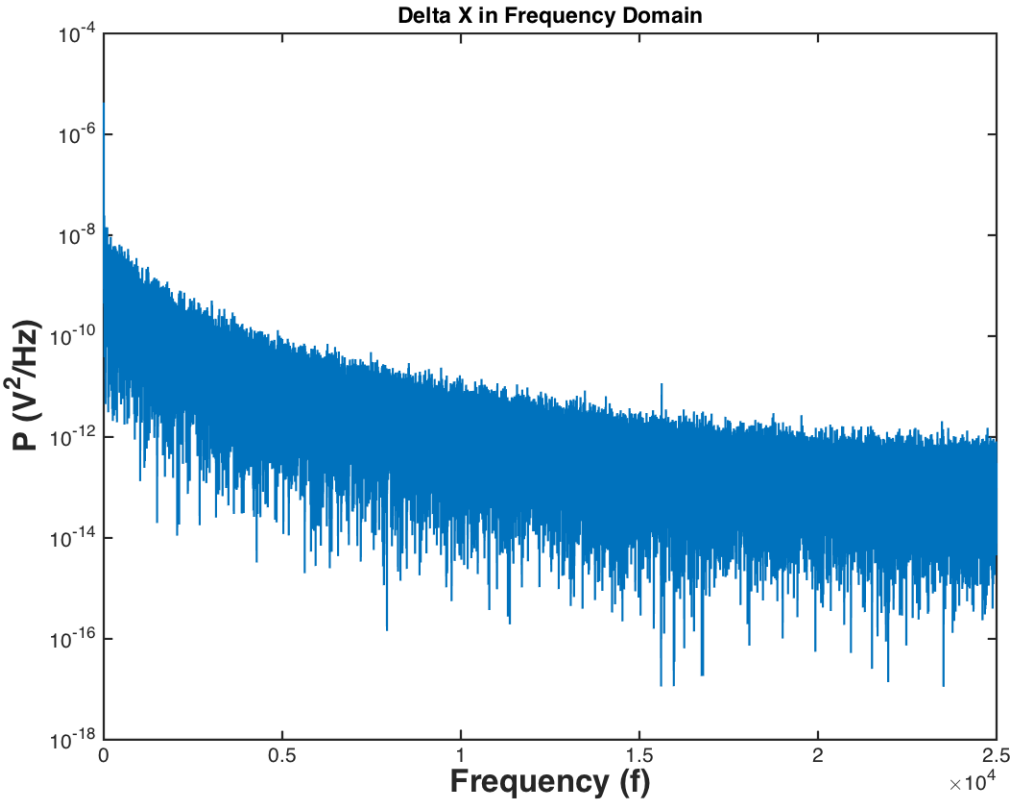

Figure B.3: one-sided power spectrum

Since the power spectrum is symmetric, it is common to ignore the redundant information of the negative frequencies, and look at the one-sided spectrum instead (Figure B.3).

It is more useful to plot the power spectrum on a log-log axes, as shown in figure B.4. The power spectrum can be fit with an overall scaling factor and a rolloff frequency to a Lorentzian curve which describes the equation of motion of a damped oscillator with Brownian motion. The mass of the bead is small and thus inertial forces are much weaker than those of hydrodynamic drag. The equation of motion

for a massless damped oscillator is given by:

$$F(t) = \beta\dot{x}(t) + kx(t) \tag{B.2}$$

Where x is the position of the bead, β is the drag coefficient, and $F(t)$ is the fore induced by the thermal fluctuations of water molecules surrounding the bead. The drag coefficient, $\beta = 6\pi\eta r$, is a function of the bead radius r and the viscosity of the surrounding fluid ($\eta = 8.9 \times 10^{-4}$Pa s for water at room temperature). The Fourier transform of the equation of motion is

$$\tilde{F}(f) = 2\pi\beta(\frac{k}{2\pi\beta} - if)\tilde{x}(f) \tag{B.3}$$

Where the Brownian noise source is given by $|\tilde{F}(f)|^2 = 4\beta k_b T$. Rearranging the last result gives us the theoretical Lorentzian power spectrum:

$$|\tilde{x}(f)|^2 = \frac{k_b T}{\pi^2\beta[(\frac{k}{2\pi\beta})^2 + f^2]} \tag{B.4}$$

$$= \frac{k_b T}{\pi^2\beta[f_c^2 + f^2]} \tag{B.5}$$

Where f_c is also referred to as the corner frequency of the power spectrum. Thus by fitting one's data to the proper corner frequency, the trap stiffness can be determined, $k = 2\pi\beta f_c$. Note that this stiffness corresponds only to stiffness in the X-direction (one must measure displacement fluctuations in the y-direction y(t), in order to also get the trap stiffness in the y-direction). Axial stiffness can also be measured from the power spectrum of the z-direction QPD signal, but wall effects create larger drag

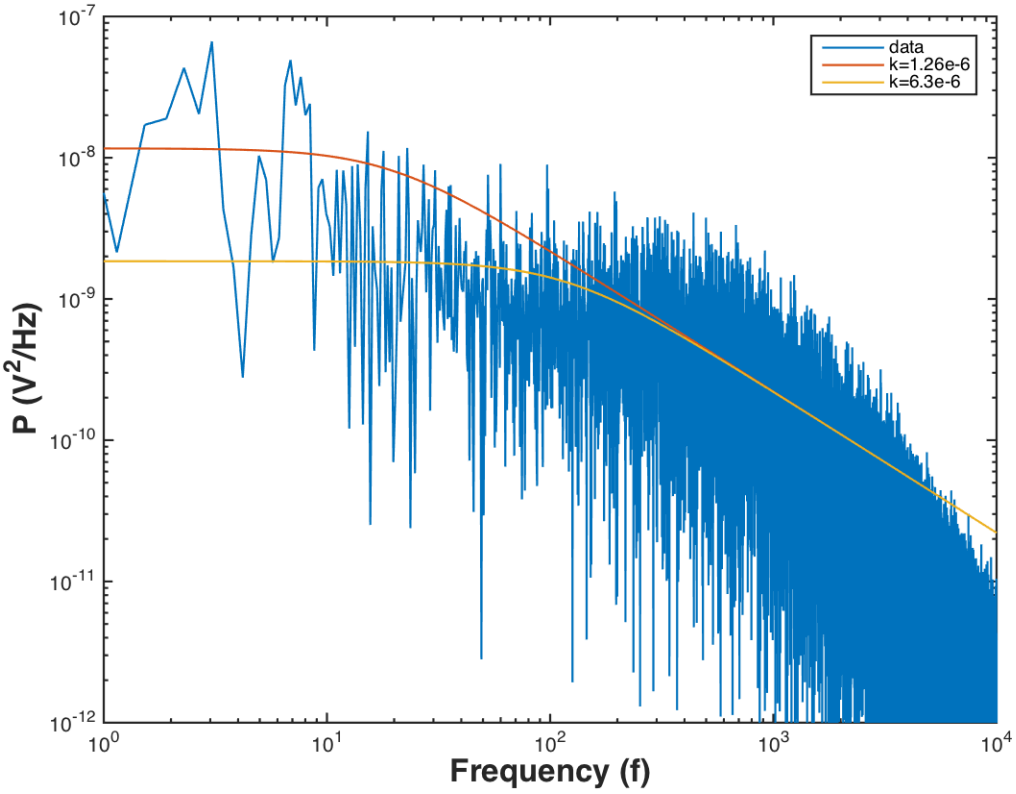

Figure B.4: Power spectrum roll-off overlaid with examples of the theoretical Lorentzian curves of two different corner frequencies (stiffness values given in N/m). Note that the stiffer trap has a higher corner frequency. The data shown is in its raw form, without taking into account the effects of hydrodynamic interactions and acquistion instrumentation filters.

forces in the axial direction than in the lateral directions, and should be accounted for [205]. With the PSD method, it is not necessary to convert the photodiode voltage to displacement, therefore no position calibration is required (although an assumption is made on the drag coefficient).

B.2.3 Fitting PSD data to the Lorentzian

As one can see, the spectrum falls significantly lower than the Lorentzian curve for higher frequencies. A more precise calibration method was investigated by [206] and [147], which accounts for frequency-dependence of hydrodynamic effects, interaction with the nearby coverslip, effects of finite-sampling (aliasing), and possible anti-alias filtering in the data acquisition electrons. Trap stiffness was calibrated in the x, y, and z-directions through power spectrum density calibration with these considerations [147, 206].

B.3 Calculating the maximum trap holding force

We can relate the maximum holding force of the trap to the frictional force observed on beads moving at a velocity v. Stokes' law can be used to calculate the frictional force on spherical objects with a small Reynolds number in a viscous fluid. The frictional force, or drag force F_d, is given by:

$$F_d = 6\pi\eta_{eff}Rv \tag{B.6}$$

where η_{eff} is the effective dynamic viscosity of the fluid, R is the radius of the bead, and v is the flow velocity relatively to the object. Although one can measure R and v directly, the effective viscosity of the water and bead suspension must be measured

experimentally from the mean squared displacement of particles in solution. The mean squared displacement (MSD) can be related to the diffusion constant D:

$$MSD(t) = 2dDt \tag{B.7}$$

where d is a dimensionality constant (e.g. d=2 for two-dimensional range of motion), and t is time. Using the Stokes-Einstein equation, the diffusion constant of a particle with radius R can be related to the effective viscosity, η_{eff}, by:

$$D = \frac{k_B T}{6\pi\eta_{eff} R} \tag{B.8}$$

where k_B is the Boltzmann constant, and T is the temperature.

The MSD can be calculated from using the FIJI plugin TrackMate and computing:

$$MSD(t_i) = (x(t_i) - x(0))^2 + (y(t_i) - y(0))^2 \tag{B.9}$$

If we plot the MSD over time for our silica beads, the slope of this line (which we will call m) is given by:

$$m = 2dD = \frac{2k_B T}{3\pi\eta_{eff} R} \tag{B.10}$$

B.3.1 Example of maximum trap holding force

To find the effective viscosity η_{eff}, 40 to 60-second duration videos were taken at 100x magnification of silica beads subjected to the Brownian motion of the surrounding water molecules. Tracking of particle displacements over time were analyzed with the Trackmate plugin of FIJI and exported into Matlab. Examples of MSD(t) curves

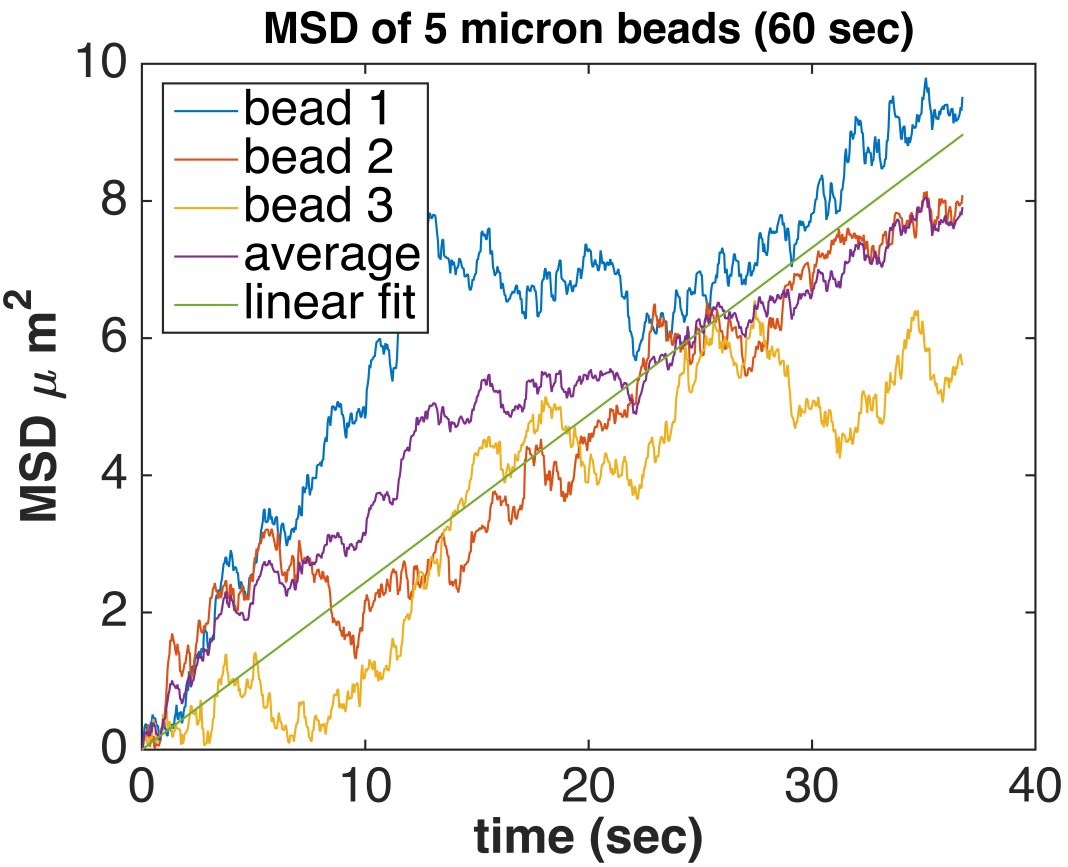

Figure B.5: mean squared displacements for 5 micron diameter silica beads plotted alongside a linear fit for the averaged displacements.

for a set of 5 micron silica beads suspended in filtered deionized water is shown in Figure B.5.

Note that although the average displacement due to Brownian motion should be zero, the mean-squared displacement is not zero, and increases as a function of time. In the case of the 5 um beads, the effective viscosity, which is found from equation B.10, is found as $\eta_{eff} = \frac{2k_BT}{3\pi Rm} = .0014$ Ns/m^2. In comparison, the dynamic viscosity of water is typically .0009 Ns/m^2.

Now that we have obtained the effective viscosity, we can now compute the drag

force for different applied velocities. To achieve this, a single bead is trapped at a fixed laser power, and then the fluid velocity is increased until the bead is dragged out of the trap. The velocity of the surrounding particles is also measured using the Trackmate plugin of FIJI.

For 5 micron beads at 200 mW power at the back aperture, the velocity at which the bead is dragged out of the trap was demonstrated to be 335 microns/sec. Plugging this into our equation for drag force, $Fd = 6\pi\eta Rv = 6\pi 0.0014\text{Ns}/(m^2)(2.5 \times 10^{-6}m)(335 \times 10^{-6}m/s) = 22.1\text{pN}$. The maximum holding distance is the distance that the bead can be pulled away from the bead center (i.e., the distance when the maximum force is applied). In most cases, increasing the power of the optical trap will increase the stiffness of the trap, but at the cost of reducing the maximum trap holding distance.

Appendix C

For each indentation experiment, a separate folder (named by a unique experiment identification number) is saved on the Hopkins Extreme Materials Institute (HEMI) Craedl website which contains:

- Voltage history raw data sets in the form of an Excel sheet (ExperimentID.xlsx). The columns are indicated by "SGX" (stage translation in the x-direction),"SGY" (stage translation in the y-direction), "QPDX" (bead deflection in x-direction measured by QPD detector), "QPDY" (bead deflection in y-direction measured by QPD detector), and "SUM" (bead deflection in z-direction measured by QPD detector).

- An image (or video) of the cell that was probed during the experiment. The images were used to obtain the cell diameter values and determine the direction of loading.

APPENDIX C.

- A custom-built Matlab code (v3fdExperimentID.m) that 1.) converts the voltage histories to forces and indentation depths and 2.) calculates the hyperelastic material properties from the force-displacement curves of the two strain rate regimes. The code also outputs several images, including the experimental force-displacement curves, along with the fitted force-displacement curves with the hyperelastic formulation.

Bibliography

[1] Y.-B. Lu, K. Franze, G. Seifert, C. Steinhäuser, F. Kirchhoff, H. Wolburg, J. Guck, P. Janmey, E.-Q. Wei, J. Käs *et al.*, "Viscoelastic properties of individual glial cells and neurons in the cns," *Proceedings of the National Academy of Sciences*, vol. 103, no. 47, pp. 17 759–17 764, 2006.

[2] Y. A. Ayala, B. Pontes, D. S. Ether, L. B. Pires, G. R. Araujo, S. Frases, L. F. Romão, M. Farina, V. Moura-Neto, N. B. Viana *et al.*, "Rheological properties of cells measured by optical tweezers," *BMC biophysics*, vol. 9, no. 1, p. 5, 2016.

[3] M. Iwashita, N. Kataoka, K. Toida, and Y. Kosodo, "Systematic profiling of spatiotemporal tissue and cellular stiffness in the developing brain," *Development*, vol. 141, no. 19, pp. 3793–3798, 2014.

[4] K. B. Bernick, T. P. Prevost, S. Suresh, and S. Socrate, "Biomechanics of single cortical neurons," *Acta biomaterialia*, vol. 7, no. 3, pp. 1210–1219, 2011.

[5] B. S. Elkin, E. U. Azeloglu, K. D. Costa, and B. Morrison Iii, "Mechanical

heterogeneity of the rat hippocampus measured by atomic force microscope indentation," *Journal of neurotrauma*, vol. 24, no. 5, pp. 812–822, 2007.

[6] E. Spedden and C. Staii, "Neuron biomechanics probed by atomic force microscopy," *International journal of molecular sciences*, vol. 14, no. 8, pp. 16 124–16 140, 2013.

[7] R. Bernal, P. A. Pullarkat, and F. Melo, "Mechanical properties of axons," *Physical review letters*, vol. 99, no. 1, p. 018301, 2007.

[8] W. J. Miller, I. Leventhal, D. Scarsella, P. G. Haydon, P. Janmey, and D. F. Meaney, "Mechanically induced reactive gliosis causes atp-mediated alterations in astrocyte stiffness," *Journal of neurotrauma*, vol. 26, no. 5, pp. 789–797, 2009.

[9] M. Mustata, K. Ritchie, and H. A. McNally, "Neuronal elasticity as measured by atomic force microscopy," *Journal of neuroscience methods*, vol. 186, no. 1, pp. 35–41, 2010.

[10] S.-M. Lee, T.-H. Nguyen, K. Na, I.-J. Cho, D. H. Woo, J.-E. Oh, C. J. Lee, and E.-S. Yoon, "Nanomechanical measurement of astrocyte stiffness correlated with cytoskeletal maturation," *Journal of Biomedical Materials Research Part A*, vol. 103, no. 1, pp. 365–370, 2015.

[11] J.-P. Michalski and R. Kothary, "Oligodendrocytes in a nutshell," *Frontiers in cellular neuroscience*, vol. 9, p. 340, 2015.

[12] J. Haseleu, E. Anlauf, S. Blaess, E. Endl, and A. Derouiche, "Studying subcellular detail in fixed astrocytes: dissociation of morphologically intact glial cells (dimigs)," *Frontiers in cellular neuroscience*, vol. 7, p. 54, 2013.

[13] L. Kirkpatrick and S. Brady, "Molecular components of the neuronal cytoskeleton," *Available from: in: GJ Siegel, BW Agranoff, RW Albers, et al.,(Eds.), Basic Neurochemistry: Molecular, Cellular and Medical Aspects, 6th editionLippincott-Raven, Philadelphia*, 1999.

[14] E. M. Darling and D. Di Carlo, "High-throughput assessment of cellular mechanical properties," *Annual review of biomedical engineering*, vol. 17, pp. 35–62, 2015.

[15] T. B. Puschmann, C. Zandén, I. Lebkuechner, C. Philippot, Y. de Pablo, J. Liu, and M. Pekny, "Hb-egf affects astrocyte morphology, proliferation, differentiation, and the expression of intermediate filament proteins," *Journal of neurochemistry*, vol. 128, no. 6, pp. 878–889, 2014.

[16] L. E. Goldstein, A. M. Fisher, C. A. Tagge, X.-L. Zhang, L. Velisek, J. A. Sullivan, C. Upreti, J. M. Kracht, M. Ericsson, M. W. Wojnarowicz *et al.*, "Chronic traumatic encephalopathy in blast-exposed military veterans and a

blast neurotrauma mouse model," *Science translational medicine*, vol. 4, no. 134, pp. 134ra60–134ra60, 2012.

[17] J. Ryu, I. Horkayne-Szakaly, L. Xu, O. Pletnikova, F. Leri, C. Eberhart, J. C. Troncoso, and V. E. Koliatsos, "The problem of axonal injury in the brains of veterans with histories of blast exposure," *Acta neuropathologica communications*, vol. 2, no. 1, p. 153, 2014.

[18] D. L. Adams, V. Piserchia, J. R. Economides, and J. C. Horton, "Vascular supply of the cerebral cortex is specialized for cell layers but not columns," *Cerebral Cortex*, vol. 25, no. 10, pp. 3673–3681, 2014.

[19] G. L. Baumbach, P. B. Dobrin, M. N. Hart, and D. D. Heistad, "Mechanics of cerebral arterioles in hypertensive rats." *Circulation research*, vol. 62, no. 1, pp. 56–64, 1988.

[20] S. Budday, G. Sommer, C. Birkl, C. Langkammer, J. Haybaeck, J. Kohnert, M. Bauer, F. Paulsen, P. Steinmann, E. Kuhl *et al.*, "Mechanical characterization of human brain tissue," *Acta biomaterialia*, vol. 48, pp. 319–340, 2017.

[21] M. C. Dewan, A. Rattani, S. Gupta, R. E. Baticulon, Y.-C. Hung, M. Punchak, A. Agrawal, A. O. Adeleye, M. G. Shrime, A. M. Rubiano *et al.*, "Estimating the global incidence of traumatic brain injury," *Journal of neurosurgery*, pp. 1–18, 2018.

BIBLIOGRAPHY

[22] A. C. McKee and D. H. Daneshvar, "The neuropathology of traumatic brain injury," in *Handbook of clinical neurology*. Elsevier, 2015, vol. 127, pp. 45–66.

[23] L. Cuthbert, "Leaving your brain to science: don't let myths dissuade you," *National Geographic*, 2018.

[24] E. Pilkington, "The nfl star and the brain injuries that destroyed him," *The Guardian*, 2011.

[25] K. Miller, *Biomechanics of the Brain*. Springer Science & Business Media, 2011.

[26] A. C. Bain and D. F. Meaney, "Tissue-level thresholds for axonal damage in an experimental model of central nervous system white matter injury," *Journal of biomechanical engineering*, vol. 122, no. 6, pp. 615–622, 2000.

[27] B. Morrison III, H. L. Cater, C. D. Benham, and L. E. Sundstrom, "An in vitro model of traumatic brain injury utilising two-dimensional stretch of organotypic hippocampal slice cultures," *Journal of neuroscience methods*, vol. 150, no. 2, pp. 192–201, 2006.

[28] D. K. Cullen, C. M. Simon, and M. C. LaPlaca, "Strain rate-dependent induction of reactive astrogliosis and cell death in three-dimensional neuronal–astrocytic co-cultures," *Brain research*, vol. 1158, pp. 103–115, 2007.

[29] V. Di Pietro, D. Amin, S. Pernagallo, G. Lazzarino, B. Tavazzi, R. Vagnozzi,

A. Pringle, and A. Belli, "Transcriptomics of traumatic brain injury: gene expression and molecular pathways of different grades of insult in a rat organotypic hippocampal culture model," *Journal of neurotrauma*, vol. 27, no. 2, pp. 349–359, 2010.

[30] A. J. Fournier, L. Rajbhandari, S. Shrestha, A. Venkatesan, and K. Ramesh, "In vitro and in situ visualization of cytoskeletal deformation under load: traumatic axonal injury," *The FASEB Journal*, vol. 28, no. 12, pp. 5277–5287, 2014.

[31] M. D. Tang-Schomer, A. R. Patel, P. W. Baas, and D. H. Smith, "Mechanical breaking of microtubules in axons during dynamic stretch injury underlies delayed elasticity, microtubule disassembly, and axon degeneration," *The FASEB Journal*, vol. 24, no. 5, pp. 1401–1410, 2010.

[32] H. Ahmadzadeh, D. H. Smith, and V. B. Shenoy, "Mechanical effects of dynamic binding between tau proteins on microtubules during axonal injury," *Biophysical journal*, vol. 109, no. 11, pp. 2328–2337, 2015.

[33] K. B. Walhovd, H. Johansen-Berg, and R. T. Karadottir, "Unraveling the secrets of white matter–bridging the gap between cellular, animal and human imaging studies," *Neuroscience*, vol. 276, pp. 2–13, 2014.

[34] C. R. Ethier and C. A. Simmons, *Introductory biomechanics: from cells to organisms*. Cambridge University Press, 2007.

[35] Y. Yamaguchi, "Lecticans: organizers of the brain extracellular matrix," *Cellular and Molecular Life Sciences CMLS*, vol. 57, no. 2, pp. 276–289, 2000.

[36] E. Syková and C. Nicholson, "Diffusion in brain extracellular space," *Physiological reviews*, vol. 88, no. 4, pp. 1277–1340, 2008.

[37] R. G. Thorne and C. Nicholson, "In vivo diffusion analysis with quantum dots and dextrans predicts the width of brain extracellular space," *Proceedings of the National Academy of Sciences*, vol. 103, no. 14, pp. 5567–5572, 2006.

[38] P. Kamali-Zare and C. Nicholson, "Brain extracellular space: geometry, matrix and physiological importance," *Basic and clinical neuroscience*, vol. 4, no. 4, p. 282, 2013.

[39] U. Novak and A. H. Kaye, "Extracellular matrix and the brain: components and function," *Journal of clinical neuroscience*, vol. 7, no. 4, pp. 280–290, 2000.

[40] C. S. Barros, S. J. Franco, and U. Müller, "Extracellular matrix: functions in the nervous system," *Cold Spring Harbor perspectives in biology*, vol. 3, no. 1, p. a005108, 2011.

[41] N. Kasthuri, K. J. Hayworth, D. R. Berger, R. L. Schalek, J. A. Conchello, S. Knowles-Barley, D. Lee, A. Vázquez-Reina, V. Kaynig, T. R. Jones *et al.*, "Saturated reconstruction of a volume of neocortex," *Cell*, vol. 162, no. 3, pp. 648–661, 2015.

[42] F. A. Azevedo, L. R. Carvalho, L. T. Grinberg, J. M. Farfel, R. E. Ferretti, R. E. Leite, W. J. Filho, R. Lent, and S. Herculano-Houzel, "Equal numbers of neuronal and nonneuronal cells make the human brain an isometrically scaled-up primate brain," *Journal of Comparative Neurology*, vol. 513, no. 5, pp. 532–541, 2009.

[43] S. Herculano-Houzel, "The remarkable, yet not extraordinary, human brain as a scaled-up primate brain and its associated cost," *Proceedings of the National Academy of Sciences*, vol. 109, no. Supplement 1, pp. 10 661–10 668, 2012.

[44] P.-H. Wu, D. R.-B. Aroush, A. Asnacios, W.-C. Chen, M. E. Dokukin, B. L. Doss, P. Durand-Smet, A. Ekpenyong, J. Guck, N. V. Guz *et al.*, "A comparison of methods to assess cell mechanical properties," *Nature methods*, p. 1, 2018.

[45] J. Domke and M. Radmacher, "Measuring the elastic properties of thin polymer films with the atomic force microscope," *Langmuir*, vol. 14, no. 12, pp. 3320–3325, 1998.

[46] R. Vargas-Pinto, H. Gong, A. Vahabikashi, and M. Johnson, "The effect of the endothelial cell cortex on atomic force microscopy measurements," *Biophysical journal*, vol. 105, no. 2, pp. 300–309, 2013.

[47] S. R. Heidemann and D. Wirtz, "Towards a regional approach to cell mechanics," *Trends in cell biology*, vol. 14, no. 4, pp. 160–166, 2004.

[48] T. Grevesse, B. E. Dabiri, K. K. Parker, and S. Gabriele, "Opposite rheological properties of neuronal microcompartments predict axonal vulnerability in brain injury," *Scientific reports*, vol. 5, p. 9475, 2015.

[49] H. Miyazaki and K. Hayashi, "Atomic force microscopic measurement of the mechanical properties of intact endothelial cells in fresh arteries," *Medical & biological engineering & computing*, vol. 37, no. 4, pp. 530–536, 1999.

[50] N. Caille, O. Thoumine, Y. Tardy, and J.-J. Meister, "Contribution of the nucleus to the mechanical properties of endothelial cells," *Journal of biomechanics*, vol. 35, no. 2, pp. 177–187, 2002.

[51] F. Guilak, J. R. Tedrow, and R. Burgkart, "Viscoelastic properties of the cell nucleus," *Biochemical and biophysical research communications*, vol. 269, no. 3, pp. 781–786, 2000.

[52] E. U. Azeloglu, J. Bhattacharya, and K. D. Costa, "Atomic force microscope elastography reveals phenotypic differences in alveolar cell stiffness," *Journal of Applied Physiology*, vol. 105, no. 2, pp. 652–661, 2008.

[53] S. Yang and T. Saif, "Micromachined force sensors for the study of cell mechanics," *Review of scientific instruments*, vol. 76, no. 4, p. 044301, 2005.

[54] J. L. Alonso and W. H. Goldmann, "Feeling the forces: atomic force microscopy in cell biology," *Life sciences*, vol. 72, no. 23, pp. 2553–2560, 2003.

[55] C. T. McKee, J. A. Last, P. Russell, and C. J. Murphy, "Indentation versus tensile measurements of young's modulus for soft biological tissues," *Tissue Engineering Part B: Reviews*, vol. 17, no. 3, pp. 155–164, 2011.

[56] D. C. Lin, D. I. Shreiber, E. K. Dimitriadis, and F. Horkay, "Spherical indentation of soft matter beyond the hertzian regime: numerical and experimental validation of hyperelastic models," *Biomechanics and modeling in mechanobiology*, vol. 8, no. 5, p. 345, 2009.

[57] I. Sokolov, M. E. Dokukin, and N. V. Guz, "Method for quantitative measurements of the elastic modulus of biological cells in afm indentation experiments," *Methods*, vol. 60, no. 2, pp. 202–213, 2013.

[58] S. Sen, S. Subramanian, and D. E. Discher, "Indentation and adhesive probing of a cell membrane with afm: theoretical model and experiments," *Biophysical journal*, vol. 89, no. 5, pp. 3203–3213, 2005.

[59] K. C. Neuman and A. Nagy, "Single-molecule force spectroscopy: optical tweezers, magnetic tweezers and atomic force microscopy," *Nature methods*, vol. 5, no. 6, p. 491, 2008.

[60] N. Wang, J. P. Butler, and D. E. Ingber, "Mechanotransduction across the cell surface and through the cytoskeleton," *Science*, vol. 260, no. 5111, pp. 1124–1127, 1993.

[61] N. Wang and D. E. Ingber, "Probing transmembrane mechanical coupling and cytomechanics using magnetic twisting cytometry," *Biochemistry and Cell Biology*, vol. 73, no. 7-8, pp. 327–335, 1995.

[62] M. Dao, C. T. Lim, and S. Suresh, "Mechanics of the human red blood cell deformed by optical tweezers," *Journal of the Mechanics and Physics of Solids*, vol. 51, no. 11-12, pp. 2259–2280, 2003.

[63] C. Lim, M. Dao, S. Suresh, C. Sow, and K. Chew, "Large deformation of living cells using laser traps," *Acta Materialia*, vol. 52, no. 7, pp. 1837–1845, 2004.

[64] E. Planus, R. Fodil, M. Balland, D. Isabey *et al.*, "Assessment of mechanical properties of adherent living cells by bead micromanipulation: comparison of magnetic twisting cytometry vs optical tweezers," *Journal of biomechanical engineering*, vol. 124, no. 4, pp. 408–421, 2002.

[65] E. Evans and R. Hochmuth, "Membrane viscoelasticity," *Biophysical Journal*, vol. 16, no. 1, pp. 1–11, 1976.

[66] L. M. Lee and A. P. Liu, "The application of micropipette aspiration in molecular mechanics of single cells," *Journal of nanotechnology in engineering and medicine*, vol. 5, no. 4, p. 040902, 2014.

[67] R. M. Hochmuth, "Micropipette aspiration of living cells," *Journal of biomechanics*, vol. 33, no. 1, pp. 15–22, 2000.

[68] N. Nishimura, C. B. Schaffer, B. Friedman, P. D. Lyden, and D. Kleinfeld, "Penetrating arterioles are a bottleneck in the perfusion of neocortex," *Proceedings of the National Academy of Sciences*, vol. 104, no. 1, pp. 365–370, 2007.

[69] M. J. Cipolla, J. Sweet, S.-L. Chan, M. J. Tavares, N. Gokina, and J. E. Brayden, "Increased pressure-induced tone in rat parenchymal arterioles vs. middle cerebral arteries: role of ion channels and calcium sensitivity," *Journal of applied physiology*, vol. 117, no. 1, pp. 53–59, 2014.

[70] M. J. Cipolla, "The cerebral circulation," *Integrated systems physiology: From molecule to function*, vol. 1, no. 1, pp. 1–59, 2009.

[71] B. R. L. M. Koeppen and A. Stanton, "Physiology fifth edition. copyright elsevier," 2004.

[72] E. A. Winkler, A. P. Sagare, and B. V. Zlokovic, "The pericyte: A forgotten cell type with important implications for a lzheimer's disease?" *Brain pathology*, vol. 24, no. 4, pp. 371–386, 2014.

[73] E. P. Wei, W. D. Dietrich, J. T. Povlishock, R. M. Navari, and H. A. Kontos, "Functional, morphological, and metabolic abnormalities of the cerebral microcirculation after concussive brain injury in cats." *Circulation research*, vol. 46, no. 1, pp. 37–47, 1980.

[74] P. Barzó, A. Marmarou, P. Fatouros, F. Corwin, and J. Dunbar, "Magnetic

resonance imaging?monitored acute blood-brain barrier changes in experimental traumatic brain injury," *Journal of neurosurgery*, vol. 85, no. 6, pp. 1113–1121, 1996.

[75] C. D. Hue, F. S. Cho, S. Cao, R. E. Nicholls, E. W. Vogel III, C. Sibindi, O. Arancio, C. R. ?Dale? Bass, D. F. Meaney, and B. Morrison III, "Time course and size of blood–brain barrier opening in a mouse model of blast-induced traumatic brain injury," *Journal of neurotrauma*, vol. 33, no. 13, pp. 1202–1211, 2016.

[76] W. J. S. Marshall, J. L. F. Jackson, and T. W. Langfitt, "Brain swelling caused by trauma and arterial hypertension: hemodynamic aspects," *Archives of neurology*, vol. 21, no. 5, pp. 545–553, 1969.

[77] N. Szarka, K. Amrein, P. Horvath, I. Ivic, E. Czeiter, A. Buki, A. Koller, and P. Toth, "Hypertension-induced enhanced myogenic constriction of cerebral arteries is preserved after traumatic brain injury," *Journal of neurotrauma*, vol. 34, no. 14, pp. 2315–2319, 2017.

[78] A. Rodríguez-Baeza, F. Reina-de la Torre, A. Poca, M. Martí, and A. Garnacho, "Morphological features in human cortical brain microvessels after head injury: a three-dimensional and immunocytochemical study," *The Anatomical Record Part A: Discoveries in Molecular, Cellular, and Evolutionary Biology:*

An Official Publication of the American Association of Anatomists, vol. 273, no. 1, pp. 583–593, 2003.

[79] K. Kenney, F. Amyot, M. Haber, A. Pronger, T. Bogoslovsky, C. Moore, and R. Diaz-Arrastia, "Cerebral vascular injury in traumatic brain injury," *Experimental neurology*, vol. 275, pp. 353–366, 2016.

[80] A. C. McKee, R. C. Cantu, C. J. Nowinski, E. T. Hedley-Whyte, B. E. Gavett, A. E. Budson, V. E. Santini, H.-S. Lee, C. A. Kubilus, and R. A. Stern, "Chronic traumatic encephalopathy in athletes: progressive tauopathy after repetitive head injury," *Journal of Neuropathology & Experimental Neurology*, vol. 68, no. 7, pp. 709–735, 2009.

[81] A. C. McKee, T. D. Stein, C. J. Nowinski, R. A. Stern, D. H. Daneshvar, V. E. Alvarez, H.-S. Lee, G. Hall, S. M. Wojtowicz, C. M. Baugh *et al.*, "The spectrum of disease in chronic traumatic encephalopathy," *Brain*, vol. 136, no. 1, pp. 43–64, 2013.

[82] S. B. Shively, S. L. Edgerton, D. Iacono, D. P. Purohit, B.-X. Qu, V. Haroutunian, K. L. Davis, R. Diaz-Arrastia, and D. P. Perl, "Localized cortical chronic traumatic encephalopathy pathology after single, severe axonal injury in human brain," *Acta neuropathologica*, vol. 133, no. 3, pp. 353–366, 2017.

[83] V. E. Johnson, M. T. Weber, R. Xiao, D. K. Cullen, D. F. Meaney, W. Stewart,

and D. H. Smith, "Mechanical disruption of the blood–brain barrier following experimental concussion," *Acta neuropathologica*, pp. 1–16, 2018.

[84] M. LaPlaca, C. Simon, G. Prado, and D. Cullen, "Cns injury biomechanics and experimental models," *Progress in brain research*, vol. 161, pp. 13–26, 2007.

[85] D. K. Cullen, V. N. Vernekar, and M. C. LaPlaca, "Trauma-induced plasmalemma disruptions in three-dimensional neural cultures are dependent on strain modality and rate," *Journal of neurotrauma*, vol. 28, no. 11, pp. 2219–2233, 2011.

[86] V. Di Pietro, A. M. Amorini, B. Tavazzi, D. A. Hovda, S. Signoretti, C. C. Giza, G. Lazzarino, R. Vagnozzi, G. Lazzarino, and A. Belli, "Potentially neuroprotective gene modulation in an in vitro model of mild traumatic brain injury," *Molecular and cellular biochemistry*, vol. 375, no. 1-2, pp. 185–198, 2013.

[87] Q. Miao, T. Paloneva, S. Tuominen, M. Pöyhönen, S. Tuisku, M. Viitanen, and H. Kalimo, "Fibrosis and stenosis of the long penetrating cerebral arteries: the cause of the white matter pathology in cerebral autosomal dominant arteriopathy with subcortical infarcts and leukoencephalopathy," *Brain pathology*, vol. 14, no. 4, pp. 358–364, 2004.

[88] G. Baumbach, J. Walmsley, and M. Hart, "Composition and mechanics of cerebral arterioles in hypertensive rats." *The American journal of pathology*, vol. 133, no. 3, p. 464, 1988.

BIBLIOGRAPHY

[89] G. L. Baumbach and D. D. Heistad, "Cerebral circulation in chronic arterial hypertension." *Hypertension*, vol. 12, no. 2, pp. 89–95, 1988.

[90] G. A. Lammie, F. Brannan, J. Slattery, and C. Warlow, "Nonhypertensive cerebral small-vessel disease: an autopsy study," *Stroke*, vol. 28, no. 11, pp. 2222–2229, 1997.

[91] K. L. Monson, W. Goldsmith, N. M. Barbaro, and G. T. Manley, "Significance of source and size in the mechanical response of human cerebral blood vessels," *Journal of biomechanics*, vol. 38, no. 4, pp. 737–744, 2005.

[92] R. W. Ogden, "Large deformation isotropic elasticity–on the correlation of theory and experiment for incompressible rubberlike solids," *Proc. R. Soc. Lond. A*, vol. 326, no. 1567, pp. 565–584, 1972.

[93] J. D. Finan, S. N. Sundaresh, B. S. Elkin, G. M. McKhann II, and B. Morrison III, "Regional mechanical properties of human brain tissue for computational models of traumatic brain injury," *Acta biomaterialia*, vol. 55, pp. 333–339, 2017.

[94] S. Lee, M. King, J. Sun, H. Xie, G. Subhash, and M. Sarntinoranont, "Measurement of viscoelastic properties in multiple anatomical regions of acute rat brain tissue slices," *Journal of the mechanical behavior of biomedical materials*, vol. 29, pp. 213–224, 2014.

[95] F. Velardi, F. Fraternali, and M. Angelillo, "Anisotropic constitutive equations and experimental tensile behavior of brain tissue," *Biomechanics and modeling in mechanobiology*, vol. 5, no. 1, pp. 53–61, 2006.

[96] R. W. Carlsen and N. P. Daphalapurkar, "The importance of structural anisotropy in computational models of traumatic brain injury," *Frontiers in neurology*, vol. 6, p. 28, 2015.

[97] R. J. Cloots, J. Van Dommelen, S. Kleiven, and M. Geers, "Multi-scale mechanics of traumatic brain injury: predicting axonal strains from head loads," *Biomechanics and modeling in mechanobiology*, vol. 12, no. 1, pp. 137–150, 2013.

[98] N. C. Colgan, M. D. Gilchrist, and K. M. Curran, "Applying dti white matter orientations to finite element head models to examine diffuse tbi under high rotational accelerations," *Progress in biophysics and molecular biology*, vol. 103, no. 2-3, pp. 304–309, 2010.

[99] R. H. Kraft, P. J. Mckee, A. M. Dagro, and S. T. Grafton, "Combining the finite element method with structural connectome-based analysis for modeling neurotrauma: connectome neurotrauma mechanics," *PLoS computational biology*, vol. 8, no. 8, p. e1002619, 2012.

[100] H. T. Garimella and R. H. Kraft, "Modeling the mechanics of axonal fiber

tracts using the embedded finite element method," *International journal for numerical methods in biomedical engineering*, vol. 33, no. 5, p. e2823, 2017.

[101] G. A. Holzapfel, T. C. Gasser, and R. W. Ogden, "A new constitutive framework for arterial wall mechanics and a comparative study of material models," *Journal of elasticity and the physical science of solids*, vol. 61, no. 1-3, pp. 1–48, 2000.

[102] T. C. Gasser, R. W. Ogden, and G. A. Holzapfel, "Hyperelastic modelling of arterial layers with distributed collagen fibre orientations," *Journal of the royal society interface*, vol. 3, no. 6, pp. 15–35, 2006.

[103] R. M. Wright and K. Ramesh, "An axonal strain injury criterion for traumatic brain injury," *Biomechanics and modeling in mechanobiology*, vol. 11, no. 1-2, pp. 245–260, 2012.

[104] R. M. Wright, A. Post, B. Hoshizaki, and K. T. Ramesh, "A multiscale computational approach to estimating axonal damage under inertial loading of the head," *Journal of neurotrauma*, vol. 30, no. 2, pp. 102–118, 2013.

[105] S. Ganpule, N. P. Daphalapurkar, K. T. Ramesh, A. K. Knutsen, D. L. Pham, P. V. Bayly, and J. L. Prince, "A three-dimensional computational human head model that captures live human brain dynamics," *Journal of neurotrauma*, vol. 34, no. 13, pp. 2154–2166, 2017.

[106] S. H. Haddad and Y. M. Arabi, "Critical care management of severe traumatic brain injury in adults," *Scandinavian journal of trauma, resuscitation and emergency medicine*, vol. 20, no. 1, p. 12, 2012.

[107] P. J. Blanco, L. O. Müller, and J. D. Spence, "Blood pressure gradients in cerebral arteries: a clue to pathogenesis of cerebral small vessel disease," *Stroke and vascular neurology*, pp. svn–2017, 2017.

[108] R. G. Budynas, J. K. Nisbett *et al.*, *Shigley's mechanical engineering design*. McGraw-Hill New York, 2008, vol. 8.

[109] C. Horgan and A. Chan, "The pressurized hollow cylinder or disk problem for functionally graded isotropic linearly elastic materials," *Journal of Elasticity*, vol. 55, no. 1, pp. 43–59, 1999.

[110] D. Moody, M. Bell, and V. Challa, "The corpus callosum, a unique white-matter tract: anatomic features that may explain sparing in binswanger disease and resistance to flow of fluid masses." *American journal of neuroradiology*, vol. 9, no. 6, pp. 1051–1059, 1988.

[111] M. Urrecha, I. Romero, J. DeFelipe, and A. Merchán-Pérez, "Influence of cerebral blood vessel movements on the position of perivascular synapses," *PloS one*, vol. 12, no. 2, p. e0172368, 2017.

[112] C. A. Tagge, A. M. Fisher, O. V. Minaeva, A. Gaudreau-Balderrama, J. A.

Moncaster, X.-L. Zhang, M. W. Wojnarowicz, N. Casey, H. Lu, O. N. Kokiko-Cochran *et al.*, "Concussion, microvascular injury, and early tauopathy in young athletes after impact head injury and an impact concussion mouse model," *Brain*, vol. 141, no. 2, pp. 422–458, 2018.

[113] H. van den Bedem and E. Kuhl, "Molecular mechanisms of chronic traumatic encephalopathy," *Current Opinion in Biomedical Engineering*, vol. 1, pp. 23–30, 2017.

[114] H. Ahmadzadeh, D. H. Smith, and V. B. Shenoy, "Viscoelasticity of tau proteins leads to strain rate-dependent breaking of microtubules during axonal stretch injury: predictions from a mathematical model," *Biophysical journal*, vol. 106, no. 5, pp. 1123–1133, 2014.

[115] R. M. Lee, "Morphology of cerebral arteries," *Pharmacology & therapeutics*, vol. 66, no. 1, pp. 149–173, 1995.

[116] D. G. Welsh and S. S. Segal, "Endothelial and smooth muscle cell conduction in arterioles controlling blood flow," *American Journal of Physiology-Heart and Circulatory Physiology*, vol. 274, no. 1, pp. H178–H186, 1998.

[117] A. R. Bausch, F. Ziemann, A. A. Boulbitch, K. Jacobson, and E. Sackmann, "Local measurements of viscoelastic parameters of adherent cell surfaces by magnetic bead microrheometry," *Biophysical journal*, vol. 75, no. 4, pp. 2038–2049, 1998.

[118] Y. Zhang, F. Wei, Y.-C. Poh, Q. Jia, J. Chen, J. Chen, J. Luo, W. Yao, W. Zhou, W. Huang *et al.*, "Interfacing 3d magnetic twisting cytometry with confocal fluorescence microscopy to image force responses in living cells," *Nature protocols*, vol. 12, no. 7, p. 1437, 2017.

[119] D. Weihs, T. G. Mason, and M. A. Teitell, "Bio-microrheology: a frontier in microrheology," *Biophysical journal*, vol. 91, no. 11, pp. 4296–4305, 2006.

[120] P. Panorchan, J. S. Lee, T. P. Kole, Y. Tseng, and D. Wirtz, "Microrheology and rock signaling of human endothelial cells embedded in a 3d matrix," *Biophysical journal*, vol. 91, no. 9, pp. 3499–3507, 2006.

[121] C. T. Laurencin and L. S. Nair, *Nanotechnology and regenerative engineering: the scaffold*. CRC Press, 2014.

[122] J. F. Mano, *Biomimetic approaches for biomaterials development*. John Wiley & Sons, 2013.

[123] S.-Y. Tee, J. Fu, C. S. Chen, and P. A. Janmey, "Cell shape and substrate rigidity both regulate cell stiffness," *Biophysical journal*, vol. 100, no. 5, pp. L25–L27, 2011.

[124] E. Cukierman, R. Pankov, D. R. Stevens, and K. M. Yamada, "Taking cell-matrix adhesions to the third dimension," *Science*, vol. 294, no. 5547, pp. 1708–1712, 2001.

[125] F. Pampaloni, E. G. Reynaud, and E. H. Stelzer, "The third dimension bridges the gap between cell culture and live tissue," *Nature reviews Molecular cell biology*, vol. 8, no. 10, p. 839, 2007.

[126] P. D. Benya and J. D. Shaffer, "Dedifferentiated chondrocytes reexpress the differentiated collagen phenotype when cultured in agarose gels," *Cell*, vol. 30, no. 1, pp. 215–224, 1982.

[127] H. Baharvand, S. M. Hashemi, S. K. Ashtiani, and A. Farrokhi, "Differentiation of human embryonic stem cells into hepatocytes in 2d and 3d culture systems in vitro," *International Journal of Developmental Biology*, vol. 50, no. 7, pp. 645–652, 2004.

[128] D. Mooney, L. Hansen, J. Vacanti, R. Langer, S. Farmer, and D. Ingber, "Switching from differentiation to growth in hepatocytes: control by extracellular matrix," *Journal of cellular physiology*, vol. 151, no. 3, pp. 497–505, 1992.

[129] L. E. O'Brien, M. M. Zegers, and K. E. Mostov, "Building epithelial architecture: insights from three-dimensional culture models," *Nature Reviews Molecular Cell Biology*, vol. 3, no. 7, p. 531, 2002.

[130] A. L. Placone, P. M. McGuiggan, D. E. Bergles, H. Guerrero-Cazares, A. Quiñones-Hinojosa, and P. C. Searson, "Human astrocytes develop phys-

iological morphology and remain quiescent in a novel 3d matrix," *Biomaterials*, vol. 42, pp. 134–143, 2015.

[131] C. L. Lau, M. Kovacevic, T. S. Tingleff, J. S. Forsythe, H. S. Cate, D. Merlo, C. Cederfur, F. L. Maclean, C. L. Parish, M. K. Horne *et al.*, "3d electrospun scaffolds promote a cytotrophic phenotype of cultured primary astrocytes," *Journal of neurochemistry*, vol. 130, no. 2, pp. 215–226, 2014.

[132] J. R. Staunton, B. L. Doss, S. Lindsay, and R. Ros, "Correlating confocal microscopy and atomic force indentation reveals metastatic cancer cells stiffen during invasion into collagen i matrices," *Scientific reports*, vol. 6, p. 19686, 2016.

[133] K. Costa and F. Yin, "Analysis of indentation: implications for measuring mechanical properties with atomic force microscopy," *Journal of biomechanical engineering*, vol. 121, no. 5, pp. 462–471, 1999.

[134] Y. Tseng, T. P. Kole, and D. Wirtz, "Micromechanical mapping of live cells by multiple-particle-tracking microrheology," *Biophysical journal*, vol. 83, no. 6, pp. 3162–3176, 2002.

[135] T. P. Kole, Y. Tseng, and D. Wirtz, "Intracellular microrheology as a tool for the measurement of the local mechanical properties of live cells," in *Methods in cell biology*. Elsevier, 2004, vol. 78, pp. 45–64.

[136] M. Mak, R. D. Kamm, and M. H. Zaman, "Impact of dimensionality and network disruption on microrheology of cancer cells in 3d environments," *PLoS computational biology*, vol. 10, no. 11, p. e1003959, 2014.

[137] M. S. Yousafzai, F. Ndoye, G. Coceano, J. Niemela, S. Bonin, G. Scoles, and D. Cojoc, "Substrate-dependent cell elasticity measured by optical tweezers indentation," *Optics and Lasers in Engineering*, vol. 76, pp. 27–33, 2016.

[138] A. Kamgoué, J. Ohayon, and P. Tracqui, "Estimation of cell young?s modulus of adherent cells probed by optical and magnetic tweezers: influence of cell thickness and bead immersion," *Journal of biomechanical engineering*, vol. 129, no. 4, pp. 523–530, 2007.

[139] S. Nawaz, P. Sánchez, K. Bodensiek, S. Li, M. Simons, and I. A. Schaap, "Cell visco-elasticity measured with afm and optical trapping at sub-micrometer deformations," *PloS one*, vol. 7, no. 9, p. e45297, 2012.

[140] A. Ashkin, J. M. Dziedzic, J. Bjorkholm, and S. Chu, "Observation of a single-beam gradient force optical trap for dielectric particles," *Optics letters*, vol. 11, no. 5, pp. 288–290, 1986.

[141] Y. Harada and T. Asakura, "Radiation forces on a dielectric sphere in the rayleigh scattering regime," *Optics communications*, vol. 124, no. 5-6, pp. 529–541, 1996.

[142] H. Zhang and K.-K. Liu, "Optical tweezers for single cells," *Journal of the Royal Society interface*, vol. 5, no. 24, pp. 671–690, 2008.

[143] S. Ayano, Y. Wakamoto, S. Yamashita, and K. Yasuda, "Quantitative measurement of damage caused by 1064-nm wavelength optical trapping of escherichia coli cells using on-chip single cell cultivation system," *Biochemical and biophysical research communications*, vol. 350, no. 3, pp. 678–684, 2006.

[144] K. C. Neuman, E. H. Chadd, G. F. Liou, K. Bergman, and S. M. Block, "Characterization of photodamage to escherichia coli in optical traps," *Biophysical journal*, vol. 77, no. 5, pp. 2856–2863, 1999.

[145] E. K. Dimitriadis, F. Horkay, J. Maresca, B. Kachar, and R. S. Chadwick, "Determination of elastic moduli of thin layers of soft material using the atomic force microscope," *Biophysical journal*, vol. 82, no. 5, pp. 2798–2810, 2002.

[146] N. Guz, M. Dokukin, V. Kalaparthi, and I. Sokolov, "If cell mechanics can be described by elastic modulus: study of different models and probes used in indentation experiments," *Biophysical journal*, vol. 107, no. 3, pp. 564–575, 2014.

[147] I. M. Tolić-Nørrelykke, K. Berg-Sørensen, and H. Flyvbjerg, "Matlab program for precision calibration of optical tweezers," *Computer physics communications*, vol. 159, no. 3, pp. 225–240, 2004.

[148] D. Sengupta, A. Kottapalli, S. Chen, J. Miao, C. Kwok, M. Triantafyllou, M. Warkiani, and M. Asadnia, "Characterization of single polyvinylidene fluoride (pvdf) nanofiber for flow sensing applications," *AIP Advances*, vol. 7, no. 10, p. 105205, 2017.

[149] J. D. Humphrey, "Continuum biomechanics of soft biological tissues," in *Proceedings of the Royal Society of London A: Mathematical, Physical and Engineering Sciences*, vol. 459, no. 2029. The Royal Society, 2003, pp. 3–46.

[150] V. C. Mow, F. Guilak, R. Tran-Son-Tay, and R. M. Hochmuth, *Cell mechanics and cellular engineering*. Springer Science & Business Media, 2012.

[151] X. Dai, K. Kathiria, and Y.-C. Huang, "Electrospun fiber scaffolds of poly (glycerol-dodecanedioate) and its gelatin blended polymers for soft tissue engineering," *Biofabrication*, vol. 6, no. 3, p. 035005, 2014.

[152] H. Kawai, "The piezoelectricity of poly (vinylidene fluoride)," *Japanese Journal of Applied Physics*, vol. 8, no. 7, p. 975, 1969.

[153] C. López-Fagundo, E. Bar-Kochba, L. L. Livi, D. Hoffman-Kim, and C. Franck, "Three-dimensional traction forces of schwann cells on compliant substrates," *Journal of The Royal Society Interface*, vol. 11, no. 97, p. 20140247, 2014.

[154] S. A. Maskarinec, C. Franck, D. A. Tirrell, and G. Ravichandran, "Quantify-

ing cellular traction forces in three dimensions," *Proceedings of the National Academy of Sciences*, vol. 106, no. 52, pp. 22 108–22 113, 2009.

[155] S. Hosmane, M. A. Tegenge, L. Rajbhandari, P. Uapinyoying, N. G. Kumar, N. Thakor, and A. Venkatesan, "Toll/interleukin-1 receptor domain-containing adapter inducing interferon-β mediates microglial phagocytosis of degenerating axons," *Journal of Neuroscience*, vol. 32, no. 22, pp. 7745–7757, 2012.

[156] Y.-S. Lee and T. Livingston Arinzeh, "Electrospun nanofibrous materials for neural tissue engineering," *Polymers*, vol. 3, no. 1, pp. 413–426, 2011.

[157] M. P. Lutolf, P. M. Gilbert, and H. M. Blau, "Designing materials to direct stem-cell fate," *Nature*, vol. 462, no. 7272, p. 433, 2009.

[158] S. Suresh, J. Spatz, J. Mills, A. Micoulet, M. Dao, C. Lim, M. Beil, and T. Seufferlein, "Connections between single-cell biomechanics and human disease states: gastrointestinal cancer and malaria," *Acta biomaterialia*, vol. 1, no. 1, pp. 15–30, 2005.

[159] E. Moeendarbary, I. P. Weber, G. K. Sheridan, D. E. Koser, S. Soleman, B. Haenzi, E. J. Bradbury, J. Fawcett, and K. Franze, "The soft mechanical signature of glial scars in the central nervous system," *Nature Communications*, vol. 8, p. 14787, 2017.

[160] S. Suresh, "Biomechanics and biophysics of cancer cells," *Acta Materialia*, vol. 55, no. 12, pp. 3989–4014, 2007.

[161] C. Lim, E. Zhou, and S. Quek, "Mechanical models for living cells?a review," *Journal of biomechanics*, vol. 39, no. 2, pp. 195–216, 2006.

[162] S. Digiuni, A. Berne-Dedieu, C. Martinez-Torres, J. Szecsi, M. Bendahmane, A. Arneodo, and F. Argoul, "Single cell wall nonlinear mechanics revealed by a multiscale analysis of afm force-indentation curves," *Biophysical journal*, vol. 108, no. 9, pp. 2235–2248, 2015.

[163] I. Levental, P. C. Georges, and P. A. Janmey, "Soft biological materials and their impact on cell function," *Soft Matter*, vol. 3, no. 3, pp. 299–306, 2007.

[164] H. Hertz, "On the contact of solid elastic bodies and on hardness," *Journal of math*, vol. 92, pp. 156–171, 1881.

[165] K. L. Johnson, *Contact mechanics*. Cambridge university press, 1987.

[166] J. A. Williams and R. S. Dwyer-Joyce, "Contact between solid surfaces," *Modern tribology handbook*, vol. 1, pp. 121–162, 2001.

[167] D. Liu, Z. Zhang, and L. Sun, "Nonlinear elastic load–displacement relation for spherical indentation on rubberlike materials," *Journal of Materials Research*, vol. 25, no. 11, pp. 2197–2202, 2010.

[168] A. Giannakopoulos and A. Triantafyllou, "Spherical indentation of incompressible rubber-like materials," *Journal of the Mechanics and Physics of Solids*, vol. 55, no. 6, pp. 1196–1211, 2007.

[169] M.-G. Zhang, Y.-P. Cao, G.-Y. Li, and X.-Q. Feng, "Spherical indentation method for determining the constitutive parameters of hyperelastic soft materials," *Biomechanics and modeling in mechanobiology*, vol. 13, no. 1, pp. 1–11, 2014.

[170] Y. Ding, G.-K. Xu, and G.-F. Wang, "On the determination of elastic moduli of cells by afm based indentation," *Scientific Reports*, vol. 7, p. 45575, 2017.

[171] I. Kang, D. Panneerselvam, V. P. Panoskaltsis, S. J. Eppell, R. E. Marchant, and C. M. Doerschuk, "Changes in the hyperelastic properties of endothelial cells induced by tumor necrosis factor-α," *Biophysical Journal*, vol. 94, no. 8, pp. 3273–3285, 2008.

[172] R. Mahaffy, C. Shih, F. MacKintosh, and J. Käs, "Scanning probe-based frequency-dependent microrheology of polymer gels and biological cells," *Physical review letters*, vol. 85, no. 4, p. 880, 2000.

[173] I. Sokolov, S. Iyer, and C. D. Woodworth, "Recovery of elasticity of aged human epithelial cells in vitro," *Nanomedicine: Nanotechnology, Biology and Medicine*, vol. 2, no. 1, pp. 31–36, 2006.

[174] B. Codan, G. Del Favero, V. Martinelli, C. Long, L. Mestroni, and O. Sbaizero, "Exploring the elasticity and adhesion behavior of cardiac fibroblasts by atomic force microscopy indentation," *Materials Science and Engineering: C*, vol. 40, pp. 427–434, 2014.

[175] T. K. Berdyyeva, C. D. Woodworth, and I. Sokolov, "Human epithelial cells increase their rigidity with ageing in vitro: direct measurements," *Physics in Medicine & Biology*, vol. 50, no. 1, p. 81, 2004.

[176] S. Park, D. Koch, R. Cardenas, J. Käs, and C.-K. Shih, "Cell motility and local viscoelasticity of fibroblasts," *Biophysical journal*, vol. 89, no. 6, pp. 4330–4342, 2005.

[177] M. H. Magdesian, F. S. Sanchez, M. Lopez, P. Thostrup, N. Durisic, W. Belkaid, D. Liazoghli, P. Grütter, and D. R. Colman, "Atomic force microscopy reveals important differences in axonal resistance to injury," *Biophysical journal*, vol. 103, no. 3, pp. 405–414, 2012.

[178] G. T. Charras and M. A. Horton, "Single cell mechanotransduction and its modulation analyzed by atomic force microscope indentation," *Biophysical journal*, vol. 82, no. 6, pp. 2970–2981, 2002.

[179] D. E. Brewe and B. J. Hamrock, "Simplified solution for elliptical-contact deformation between two elastic solids," *Journal of Lubrication Technology*, vol. 99, no. 4, pp. 485–487, 1977.

[180] B. J. Hamrock and D. Brewe, "Simplified solution for stresses and deformations," *Journal of lubrication technology*, vol. 105, no. 2, pp. 171–177, 1983.

[181] M. Puttock and E. Thwaite, *Elastic compression of spheres and cylinders at point and line contact*. Commonwealth Scientific and Industrial Research Organization Melbourne, Australia, 1969.

[182] C. O. Horgan and M. G. Smayda, "The importance of the second strain invariant in the constitutive modeling of elastomers and soft biomaterials," *Mechanics of Materials*, vol. 51, pp. 43–52, 2012.

[183] R. Mahaffy, S. Park, E. Gerde, J. Käs, and C. Shih, "Quantitative analysis of the viscoelastic properties of thin regions of fibroblasts using atomic force microscopy," *Biophysical journal*, vol. 86, no. 3, pp. 1777–1793, 2004.

[184] R. S. Chadwick, "Axisymmetric indentation of a thin incompressible elastic layer," *SIAM Journal on Applied Mathematics*, vol. 62, no. 5, pp. 1520–1530, 2002.

[185] C. M. Pereira, A. L. Ramalho, and J. A. Ambrósio, "A critical overview of internal and external cylinder contact force models," *Nonlinear Dynamics*, vol. 63, no. 4, pp. 681–697, 2011.

[186] Y. Pan, Y. Zhan, H. Ji, X. Niu, and Z. Zhong, "Can hyperelastic material

parameters be uniquely determined from indentation experiments?" *RSC Advances*, vol. 6, no. 85, pp. 81 958–81 964, 2016.

[187] A. Cartagena and A. Raman, "Local viscoelastic properties of live cells investigated using dynamic and quasi-static atomic force microscopy methods," *Biophysical journal*, vol. 106, no. 5, pp. 1033–1043, 2014.

[188] P. Sudharshan Phani and W. C. Oliver, "Ultra high strain rate nanoindentation testing," *Materials*, vol. 10, no. 6, p. 663, 2017.

[189] P. Chugh and E. K. Paluch, "The actin cortex at a glance," *J Cell Sci*, vol. 131, no. 14, p. jcs186254, 2018.

[190] K. Haase and A. E. Pelling, "The role of the actin cortex in maintaining cell shape," *Communicative & integrative biology*, vol. 6, no. 6, p. e26714, 2013.

[191] ——, "Resiliency of the plasma membrane and actin cortex to large-scale deformation," *Cytoskeleton*, vol. 70, no. 9, pp. 494–514, 2013.

[192] A. G. Clark, K. Dierkes, and E. K. Paluch, "Monitoring actin cortex thickness in live cells," *Biophysical journal*, vol. 105, no. 3, pp. 570–580, 2013.

[193] G. Ofek, D. C. Wiltz, and K. A. Athanasiou, "Contribution of the cytoskeleton to the compressive properties and recovery behavior of single cells," *Biophysical journal*, vol. 97, no. 7, pp. 1873–1882, 2009.

[194] S. Ilschner and R. Brandt, "The transition of microglia to a ramified phenotype is associated with the formation of stable acetylated and detyrosinated microtubules," *Glia*, vol. 18, no. 2, pp. 129–140, 1996.

[195] M. Sato, W. H. Schwarz, and T. D. Pollard, "Dependence of the mechanical properties of actin/α-actinin gels on deformation rate," *Nature*, vol. 325, no. 6107, p. 828, 1987.

[196] D. H. Wachsstock, W. Schwarz, and T. Pollard, "Cross-linker dynamics determine the mechanical properties of actin gels," *Biophysical journal*, vol. 66, no. 3, pp. 801–809, 1994.

[197] A. R. Harris and G. Charras, "Experimental validation of atomic force microscopy-based cell elasticity measurements," *Nanotechnology*, vol. 22, no. 34, p. 345102, 2011.

[198] Y.-S. Lee, G. Collins, and T. L. Arinzeh, "Neurite extension of primary neurons on electrospun piezoelectric scaffolds," *Acta biomaterialia*, vol. 7, no. 11, pp. 3877–3886, 2011.

[199] A. S. Motamedi, H. Mirzadeh, F. Hajiesmaeilbaigi, S. Bagheri-Khoulenjani, and M. Shokrgozar, "Effect of electrospinning parameters on morphological properties of pvdf nanofibrous scaffolds," *Progress in biomaterials*, vol. 6, no. 3, pp. 113–123, 2017.

[200] M. Cavaglia, S. M. Dombrowski, J. Drazba, A. Vasanji, P. M. Bokesch, and D. Janigro, "Regional variation in brain capillary density and vascular response to ischemia," *Brain research*, vol. 910, no. 1-2, pp. 81–93, 2001.

[201] A. Shahbazi, J. Kinnison, R. Vescovi, M. Du, R. Hill, M. Joesch, M. Takeno, H. Zeng, N. M. da Costa, J. Grutzendler *et al.*, "Flexible learning-free segmentation and reconstruction of neural volumes," *Scientific reports*, vol. 8, no. 1, p. 14247, 2018.

[202] J. W. Lichtman, H. Pfister, and N. Shavit, "The big data challenges of connectomics," *Nature neuroscience*, vol. 17, no. 11, p. 1448, 2014.

[203] R. Schalek, N. Kasthuri, K. Hayworth, D. Berger, J. Tapia, J. Morgan, S. Turaga, E. Fagerholm, H. Seung, and J. Lichtman, "Development of high-throughput, high-resolution 3d reconstruction of large-volume biological tissue using automated tape collection ultramicrotomy and scanning electron microscopy," *Microscopy and Microanalysis*, vol. 17, no. S2, pp. 966–967, 2011.

[204] Y.-B. Lu, I. Iandiev, M. Hollborn, N. Körber, E. Ulbricht, P. G. Hirrlinger, T. Pannicke, E.-Q. Wei, A. Bringmann, H. Wolburg *et al.*, "Reactive glial cells: increased stiffness correlates with increased intermediate filament expression," *The FASEB Journal*, vol. 25, no. 2, pp. 624–631, 2011.

[205] K. C. Neuman and S. M. Block, "Optical trapping," *Review of scientific instruments*, vol. 75, no. 9, pp. 2787–2809, 2004.

[206] K. Berg-Sørensen and H. Flyvbjerg, "Power spectrum analysis for optical tweezers," *Review of Scientific Instruments*, vol. 75, no. 3, pp. 594–612, 2004.

Vita

Amy M. Dagro received her B.S. degree in Biomedical Engineering at the Johns Hopkins University in 2009, followed by a M.S. degree in Mechanical Engineering from Columbia University in 2010. Shortly after receiving her Master's degree, she began working at the U.S. Army Research Laboratory (ARL) at the Aberdeen Proving Ground, MD where she worked on computational models of traumatic brain injury under the guidance of Dr. Reuben Kraft. She returned to JHU in Fall 2013 to begin her Ph.D. studies with Prof. K.T. Ramesh and in 2014 she was awarded a DoD SMART (Science, Mathematics, and Research for Transformation) Scholarship.